Title
Wafer Scale Synthesis of Thin Film Black Arsenic Phosphorus

Author
Young, Eric

Publication Date
2018

Peer reviewed|Thesis/dissertation

UNIVERSITY OF CALIFORNIA

Los Angeles

WAFER-SCALE SYNTHESIS OF THIN-FILM BLACK ARSENIC-PHOSPHORUS

A dissertation submitted in partial satisfaction of the

requirements for the degree Doctor of Philosophy

in Materials Science and Engineering

by

Eric Patrick Young

2018

ABSTRACT OF THE DISSERTATION

WAFER-SCALE SYNTHESIS OF THIN-FILM

BLACK ARSENIC-PHOSPHORUS

by

Eric Patrick Young

Doctor of Philosophy in Materials Science and Engineering

University of California, Los Angeles, 2018

Professor Dwight Christopher Streit, Chair

Herein we report the wafer-scale synthesis of few-layered black arsenic phosphorus (b-AsP) alloys via two-step solid-source molecular beam deposition (MBD) and subsequent hermetic thermal annealing. We characterized our thin films with a variety of compositional and structural metrology techniques. X-ray photoelectron spectroscopy and energy dispersive spectroscopy determine compositions of $As_{0.78}P_{0.22}$ for our thin films, while x-ray reflectivity measurements indicate film thicknesses of 6-9 nm. High resolution transmission electron spectroscopy images reveal a nanocrystalline morphology with orthorhombic b-AsP grains on the order of ~ 5 nm. Raman scattering spectroscopy is employed to characterize the vibrational structure of our thin films, and results obtained from experiments are in excellent agreement with the b-AsP bulk crystal spectra. Evidence of conformal wafer-scale is substantiated by Raman mapping. We simulate crystal structure, bandgaps, and Raman spectra from first-principle DFT-based computations and find good agreement with our experimental results. This work is the first

demonstration of on-wafer synthesis of b-AsP. Our wafer-scale growth technique enables the development of next-generation b-AsP devices for optoelectronic, digital and RF applications.

The dissertation of Eric Patrick Young is approved.

Mark S. Goorsky

Bruce S. Dunn

Subramanian Srikantes Iyer

Dwight Christopher Streit, Committee Chair

University of California, Los Angeles

2018

Table of Contents

List of Figures

Acknowledgements

This work would not have been possible without the encouragement, direction, and support from my doctoral advisor, Professor Dwight C. Streit. I will always appreciate all the wisdom, insight, and advice I received from Professor Streit, as well as all the conversations we had about cars, relationships, life experiences and a variety of other topics. I really couldn't have asked for a better advisor, and our relationship undoubtedly has left a positive, lasting impact on my personal and professional life. Thanks Professor Streit!

Additionally, I owe much gratitude to my mentor at Northrop Grumman Aerospace Systems, Dr. Vincent Gambin for the hands-on scientific training and for developing me into the researcher I am today. I appreciate all the effort and time you poured into me and I am grateful for the standard of excellence you held me to. Thanks for pushing me and encouraging me to be thorough in my experimental results and to validate them with mathematical models when possible. I appreciate you very much Vincent!

I'd also like to thank my PhD doctoral committee, Professor Mark S. Goorsky, Professor Bruce S. Dunn, and Professor Subramanian S. Iyer for all their support and guidance in this process.

Much of this work would not be possible without the help of my UCLA research collaborators. First and foremost, I'd like to thank Junsoo Park for his invaluable contributions to this thesis. All of the theoretical density functional theory calculations were performed by Junsoo, and many hours of helpful discussion were shared with him. In addition, I'd like to thank Tingyu Bai for all her cross section FIB and electron microscopy contributions. We spent many hours repeating experiments, but in the end it was all worth it. Thanks guys!

Dr. Mike Lange of Northrop Grumman Corporation was instrumental to the many deposition runs we accomplished on the Varian Gen II E, and for that I am very thankful. Additionally, Dr. Sumiko Poust was incredibly patient and helpful with ALD depositions. Finally, Dr. Claire Pettiette-Hall was gracious, accommodating, and insightful, and trained me on a variety of characterization tools at Space Park. Thanks Mike, Sumiko, and Claire!

I owe many thanks to my fellow Streit group members: Dr. Jinhee Park, Dr. Shenglin Ye, Teresa Ha, Sudheer Korlam, Clincy Cheung, and Max Kuciej. I couldn't have done it without your friendships! Also, I'd like to thank my Northrop Grumman Aerospace Systems collaborators: Tom Young, Rachel Koltun, Michael Barako, Jesse Tice, David Hong, Logan Johnson, and YC Chen.

Finally, I'd like to thank my friends and family for their support during these five years of my life. Thanks Dad, Mom, and Amy! Most of all, I owe the utmost gratitude to my God, Rock and Redeemer, Jesus Christ, my Lord.

VITA

2013	B.S. Chemical Engineering, University of California, Berkeley, CA, USA
2009-2013	Undergraduate Research Assistant, Department of Chemistry, University of California, Berkeley, CA, USA
2013-2018	Graduate Student Researcher, Department of Materials Science and Engineering, University of California, Los Angeles, CA, USA
2016-2018	Graduate Teaching Assistant, Department of Chemistry, University of California, Los Angeles, CA USA
2016-2018	Electronics and Payloads Technical Internship, Northrop Grumman Aerospace Systems, Redondo Beach, CA, USA

Publications

1. **Young, E.P.**; Park, J.; Bai, T.; DeBlock, R.H.; Lange, M.; Poust, S.; Tice, J.; Cheung, C.; Choi, C.; Dunn, B.S.; Goorsky, M.; Ozolins, V.s.; Streit, D.C.; Gambin, V.; "Wafer-Scale Deposition and Recrystallization of Black-Arsenic-Phosphorus Thin Films," *Submitted*, **2018**.

2. Chang, W.H.; Meng, L.; Dou, L.; You, J.; Chen, C.; Yang, Y.; **Young, E.P.**; Li, G.; Yang, Y.; "A Selenophene Containing Benzodithiophene-alt-thienothiophene Polymer for Additive-Free High Performance Solar Cell," *Macromolecules.* **2015**, *48*, 563-568.

3. Liu, Y.S.; Hong, Z.; Chen, Q.; Chang, W.; Zhou, H.; Song, T.; **Young, E.P.**; Yang, Y.; You, J.; Li, G.; Yang, Y. "Integrated Perovskite/Bulk-Heterojunction toward Efficient Solar Cells," *Nano Lett.* **2015**, *15*, 662-668.

4. Douglas, J. D.; Niskala, J. R.; Lee, O. P.; Yiu, A. T.; **Young, E. P.**; Chen, M. S.; Fréchet, J. M. J. "Solution-Processed, Molecular Photovoltaics that Exploit Hole Transfer from Non-Fullerene, n-Type Materials," *Adv. Mater.* **2014**, *25*, 4313-4319.

5. Douglas, J. D.; Griffini, G.; Holcombe, T. W.; **Young, E. P.**; Lee, O. P.; Chen, M. S.; Fréchet, J. M. J. "Functionalized isothianaphthene monomers that promote quinoidal character in donor-acceptor copolymers for organic photovoltaics," *Macromolecules* **2012**, *45*, 4069-4074.

Highlighted as one of the top ten most read articles in *Macromolecules* between April and June 2012

6. Piliego, C.; Holcombe, T. W.; Douglas, J. D.; Woo, C. H.; Beaujuge, P. M.; Fréchet, J. M. J. "Synthetic control of structural order in *N*-alkylthieno[3,4-*c*]pyrrole-4,6-dione based polymers for efficient solar cells," *J. Am. Chem. Soc.* **2010**, *132*, 7595-7597.

Acknowledged for performing Cyclic Voltammetry measurements

Chapter 1 Introduction

1.1 Current 2D Material Landscape: Electronics and Optoelectronics

1.1.1 Graphene

It was previously believed that two-dimensional (2D) crystals were thermodynamically unstable and thus could not exist in a free-standing state.[1-2] However, the successful micromechanical exfoliation of monolayer graphene from bulk graphite has since provided the basis for intense multidisciplinary research regarding both graphene and 2D materials within the physics, chemistry, and engineering communities. A myriad of interesting physics and applications have been studied, including massless Dirac-Fermion carrier behavior, quantum hall effect, single molecule sensing, nanoscale electronic devices and supercapacitors. [3-5]

Graphene exhibits extraordinary electronic properties resulting from its physical structure. In particular, graphene displays ambipolar transport as a result of its semi-metal band structure.[6] Upon electric field manipulation, graphene's Fermi level can be tuned to reside either in the conduction or valence band resulting in respective electron or hole transport. In addition to ambipolar transport, graphene exhibits extraordinarily high carrier mobility. As graphene's carrier mobility has been shown to be weakly dependent on temperature, phonon-electron interactions do not dominate graphene's carrier scattering processes. Impurity scattering, then, is the primary charge carrier scattering mechanism and is a direct consequence of lattice defects. Consequentially, graphene's high degree of crystallinity and nearly pristine structure minimizes lattice scattering resulting in measured carrier mobilities as high as 200,000 $cm^2/V*s$.[7] Carrier

transport is ballistic on the micrometer scale, which is highly desirable for high-speed device applications.

As silicon technology reaches maturation, the search for next-generation materials for logic circuits has intensified. The high carrier mobility of graphene makes it a promising material for application in high-speed radio frequency devices. However, device performance is limited by low on/off ratios of graphene based field-effect transistors.[8] Unlike traditional semiconductors, graphene's zero bandgap enables the generation of thermal carriers at ambient temperatures, resulting in significant off-state conduction in field-effect devices.[9-11] This non-zero off state conduction leads to unwanted power dissipation thus decreasing overall device efficiency. Various efforts have been made toward tuning graphene's zero bandgap with limited success.[12-13] Typically, successful manipulation of graphene's electronic bandgap results in drops in carrier mobility due to alteration of the pristine lattice. Thus despite the remarkable electronic transport properties of graphene, the material's electronic bandgap continues to limit the performance of graphene based nano-electronic devices.

1.1.2 Transition Metal Dichalcogenides and Hexagonal Boron-Nitride

The isolation of monolayer graphene from bulk graphite catalyzed intense research regarding the discovery, characterization and application of novel 2D materials. The transition metal dichalcogenides (TMDCs) emerged as promising candidates for application to nanoscale transistors due to their finite bandgaps as compared to pristine graphene's zero-bandgap.[14] TMDCs also feature a Van der Waal layered structure, in which the in-plane bonding is intramolecular while the out-of-plane bonding is intermolecular. Because of their weak layer-to-layer interactions, TMDCs can also be micromechanically exfoliated from the bulk to yield both few-layer and monolayer sheets. Like graphene, TMDC properties have been shown to evolve

with layer thickness revealing unique physics and chemistry at the monolayer limit. TMDC research is ongoing and potential applications include electronic and optoelectronic FET devices, spintronics, sensors, and 2D heterojunction devices.

One TMDC that has garnered interest is MoS2. Monolayer MoS2 is a direct-gap p-type semiconductor that shifts to an indirect gap semiconductor with increasing layer number. The electronic band-gap has been measured to be approximately 1.8 eV.[15] MoS2's direct-gap makes it a promising material for both optoelectronics and electronics. It is believed that a replacement for silicon CMOS devices needs to possess device on/off ratios exceeding $1*10^4$ and a corresponding electronic bandgap of 0.4 eV. Field effect transistor devices have demonstrated electron mobilities exceeding 200 cm2/V*s with appropriate device architecture and dielectric screening.[16] This is compared with crystalline silicon's electron mobility of 1400 $cm^2/V*s$. Unlike graphene, MoS2 suffers from many inherent defects, impurities, and dangling bonds which adversely affect carrier transport. As a result, improvements are still necessary before few-layer MoS2 can be legitimately considered as a potential silicon CMOS replacement.

Hexagonal boron nitride (h-BN) is another layered material which has been recently isolated as a free-standing single layer via micromechanical exfoliation. Like graphene and the TMDCs, h-BN has strong in-plane covalent bonding whereas the out of plane bonding is characterized by weak van der Waals forces. The in-plane hybridization, like graphene, is a honeycomb matrix of sp^2 hybridized covalent bonds. Unlike graphene and MoS2, h-BN is an insulator with band gap of approximately 6 eV. The hexagonal geometry is the most stable phase and exhibits strong thermal, chemical, and mechanical stability. Because of its remarkable physical properties, few layer h-BN has found use in various nano-electronic and nano-photonic applications, particularly as dielectrics or for encapsulation.[17]

1.2 Black Phosphorus

Recent 2D material research has been focused on expanding the current library of 2D compounds. Graphene, MoS2 and h-BN partially span the electromagnetic spectrum with their varied electronic bandgaps. Graphene is a zero bandgap material, and thus has applications in the radiowave and microwave frequencies. Monolayer MoS2 has an electronic bandgap of 1.9 eV which translates to optical absorption in the visible light frequencies. Finally, h-BN is a wide-gap semiconductor with bandgap 6 eV, and thus absorbs in the UV range. It is apparent that an infrared absorbing 2D material is needed for application in mid-IR based devices.

Black phosphorus (BP) has recently been rediscovered as a Van der Waal material. Figure 1.1 displays the optical absorption, structure, and electronic structure of black phosphorus alongside its other 2D material analogues.[18-20] BP is a direct-gap semiconductor, which varies with layer thickness. In the bulk, black phosphorus exhibits an electronic bandgap of 0.3 eV which corresponds to absorption in the mid-IR regime, making it an attractive material for many thermal infrared and military applications. Quantum confinement effects widen black phosphorus' bandgap as the material decreases in layer thickness. At the monolayer limit, BP exhibits electronic bandgap of 2 eV, effectively making the bandgap tunable with layer thickness. This makes BP a promising material for a variety of applications both in the visible and mid-IR regimes. The reemergence of BP provides full spectral coverage of the electromagnetic spectrum with 2D materials.

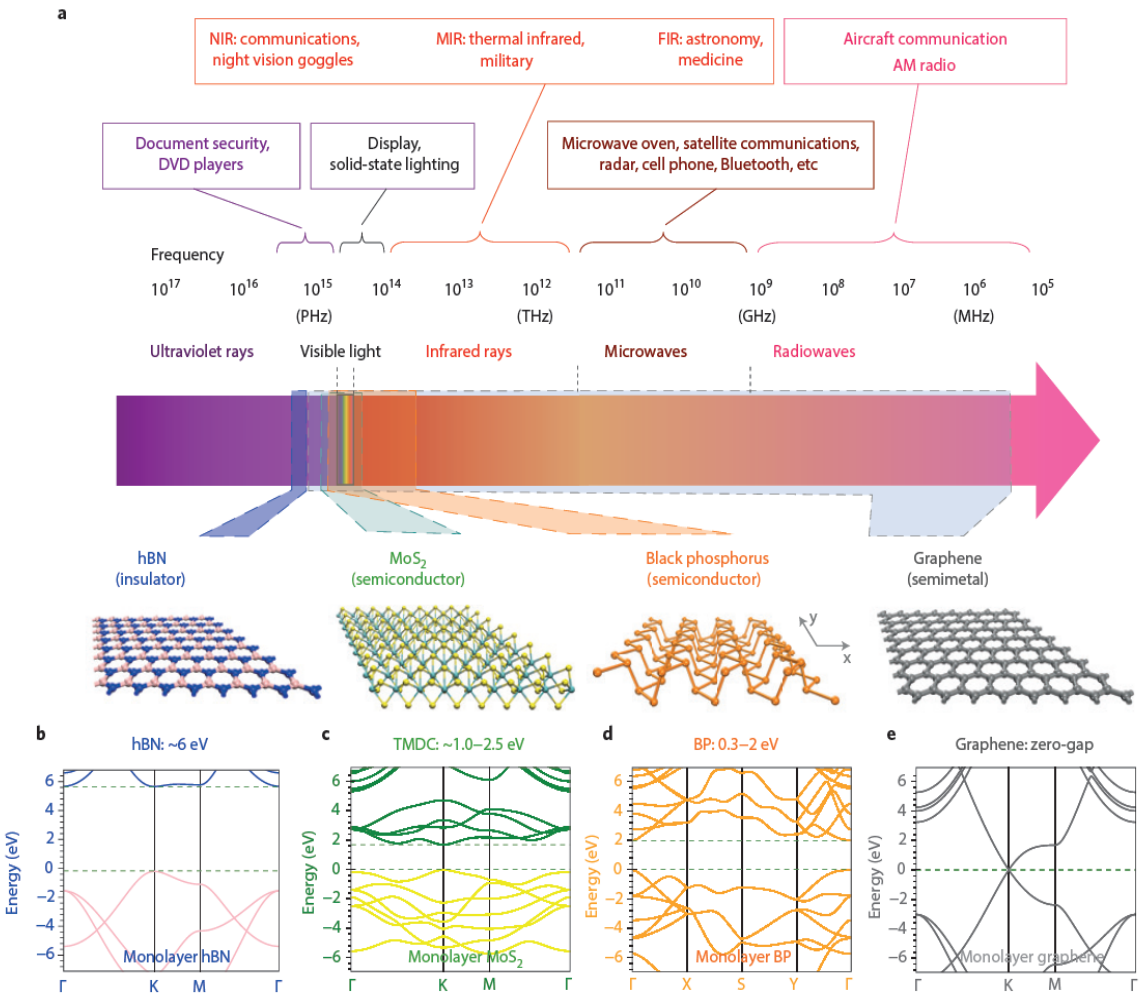

Figure 1.1: Current 2D materials displayed alongside their respective optical absorption along with potential absorption. The in-plane structures are also pictured alongside their electronic band structures. Black phosphorus absorbs in the mid-IR region, making it a promising material for thermal infrared and military applications.

Figure 1.2 also displays the optical absorption of BP with respect to the entire EM spectrum. Because of its tunability, BP has applications in the near-IR, mid-IR, and even visible regimes. This is compared with the TMDCs, which display absorption in the visible and UV regimes and zero-gap graphene which absorbs in the far-IR.

Figure 1.2: Absorption frequencies for the TMDCs, BP, and graphene. Also depicted is operation region of the electromagnetic spectrum for each of the layered materials.

Like graphene and the TMDCs, BP is a Van der Waal structure with strong in plane covalent bonding and weak out of plane london dispersion force attractions. This results in its ability to be micromechanically exfoliated and isolated in the monolayer state. However, unlike graphene, BP exhibits in-plane structrual anisotropy as depicted in Figure 1.3. While graphene belongs to the D_{6h} space group, BP belongs to the D_{2h} space group. Graphene exhibits 6 fold rotational symmetry in the x-y plane, whereas BP loses this symmetry due to the unequal phosphorus-phosphorus bond lengths and angles between bonds. This results in two different in-plane orientations; armchair along the x-direction, and zigzag along the y direction. The structural anisotropy results in anisotropic physical properties.

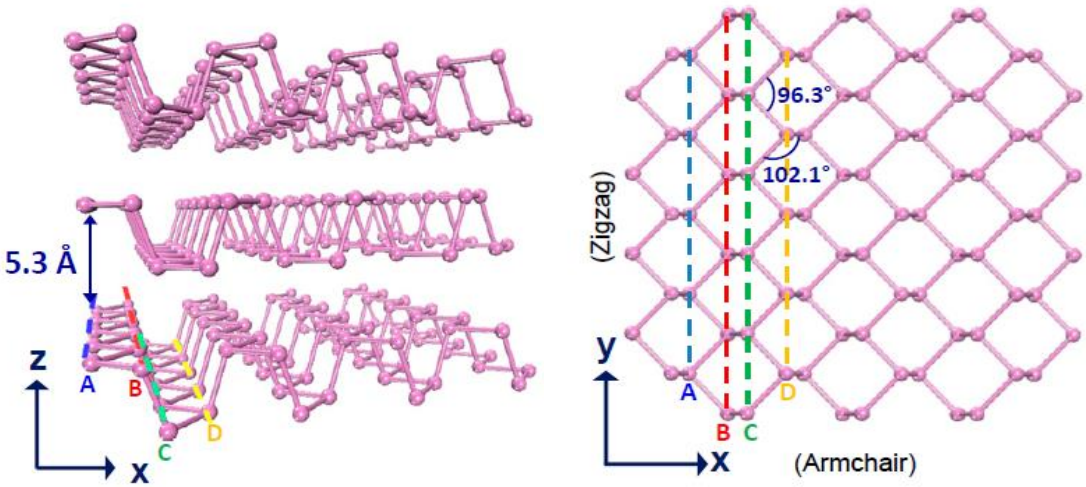

Figure 1.3: Structural depiction of layered BP. The left image illustrates the layered nature of BP with interplanar distance of 5.3 A along the z direction. Additionally, BP shows a corrugated structure along the planar direction. The right image illustrates the in-plane structure of BP with both zigzag and armchair orientations.

Early experiments on isolated BP focused on the electronic band gap characterization of the material and in particular, how it evolves with layer thickness. Density Functional Theory (DFT) calculations on band-gap provided first-principle calculations and predictions for BP's electronic structure. This has since been corroborated by experimental groups focused on fingerprinting BP layer thickness via bandgap. Figure 1.4 illustrates preliminary bandgap data using both experimental and DFT techniques. The bulk BP electronic bandgap was measured via ARPRES and was found to be direct-gap residing at the Z point. With decreasing layer thickness, the electronic bandgap remains direct gap but shifts to the gamma point as a result quantum confinement. DFT calculations revealed that the bandgap increases with decreasing layer thickness, reaching a maximum value of approximately 2.0 eV at the monolayer limit.

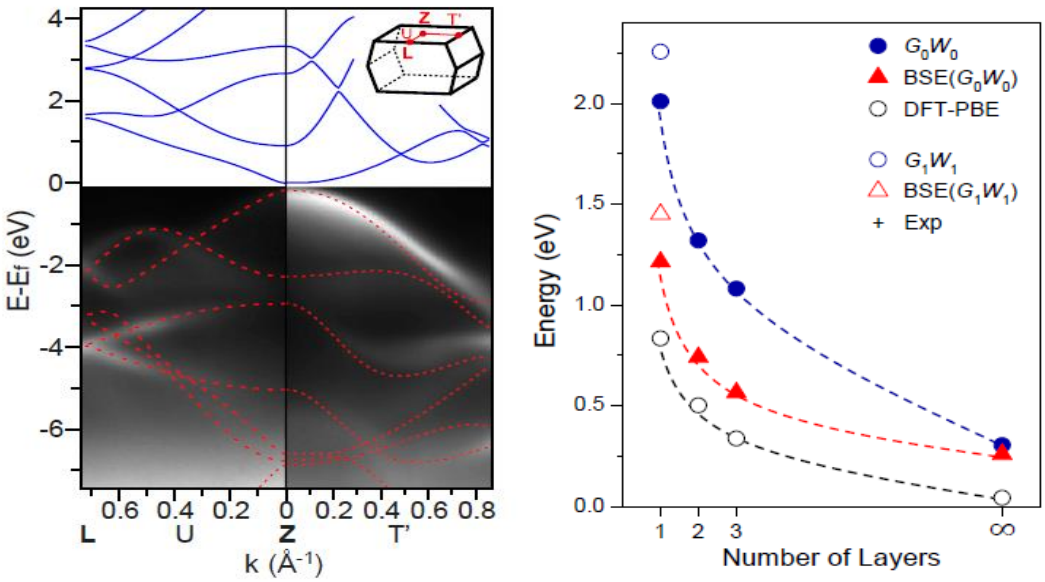

Figure 1.4: Bandgap of Black Phosphorus. (a) Experimental bandgap as determined by angle resolved photoelectron spectroscopy (ARPES). The bandgap was determined to be 0.3 eV in the bulk. (b) Theoretical first principle predictions for black phosphorus bandgap versus number of layers. Bandgap is seen to decrease from 2.0 eV in the monolayer to 0.3 eV in the bulk.

The structural anisotropy of BP results in corresponding anisotropic physical properties and as a result, BP is often deemed a "low-symmetry" material. Xia et al demonstrated that BP's absorption is a function of the incident photon polarization angle. This anisotropic absorption is a result of the structural anisotropy of the BP and in particular, the non-symmetric band structure. Figure 1.5 depicts the optical absorption spectra of BP with respect to incident light polarization.

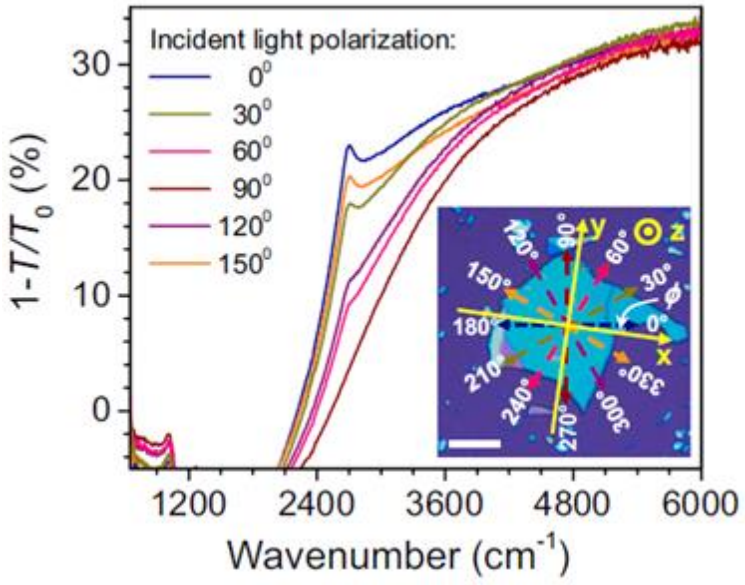

Figure 1.5: Optical absorption spectra for BP as a function of incident light polarization. FTIR transmission was collected and corresponding absorption was plotted. The inset depicts the optical image of BP with overlaid polarization axes.

Another result of the asymmetric band structure of BP is the corresponding anisotropic electronic transport properties. Theoretical and experimental groups have determined that the

electron and hole effective masses of BP differ based on transport direction.[21-23] The band structure for BP is depicted in Figure 1.6, along with a potential plasmonics application. The concavity of the valence band is seen to depend severely on direction, with the x-direction valence band having much sharper curvature versus the more concave y-direction valence band. The dispersion curve anisotropy can be exploited for plasmonic devices, particularly those requiring direction-dependent absorption.

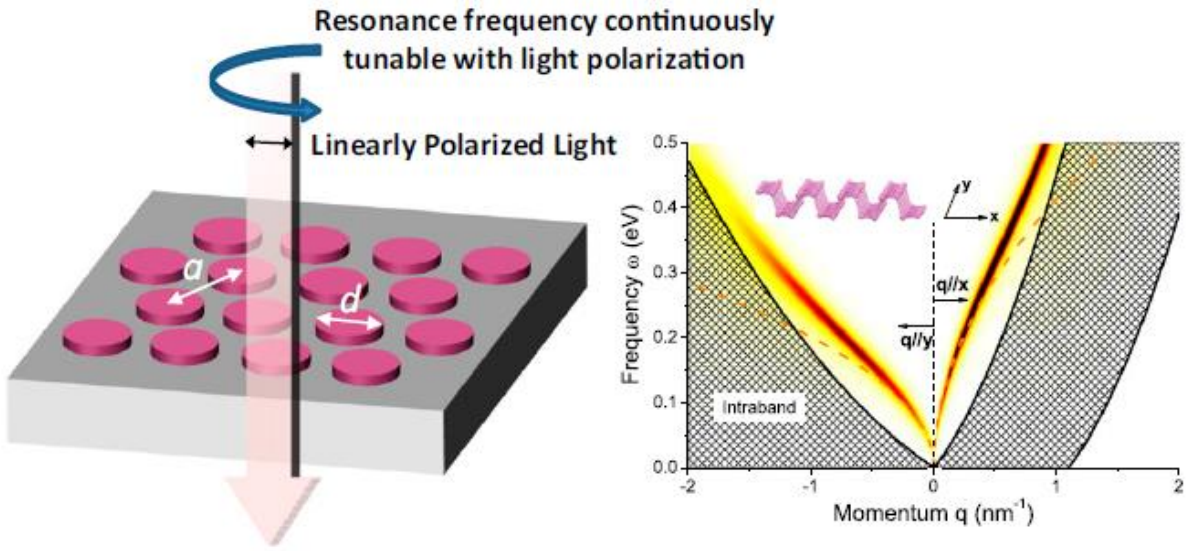

Figure 1.6: (Left) Plasmonic application of low-symmetry BP due to its anisotropic absorption properties. (Right) Dispersion curves for BP from first principle calculations.

The thermal transport properties of BP have also been investigated, particularly by Wang et al who performed DFT calculations on the material. Their results found that the "fast" phonon transport direction is orthogonal to the electron and hole transport direction. Thus heat transport is faster in the zigzag direction and slower in the armchair direction. The thermal transport anisotropy is also a result of the structural asymmetry of BP, and makes BP a promising candidate for thermoelectric applications. Figure 1.8 illustrates the orthogonal heat and electron transport direction.

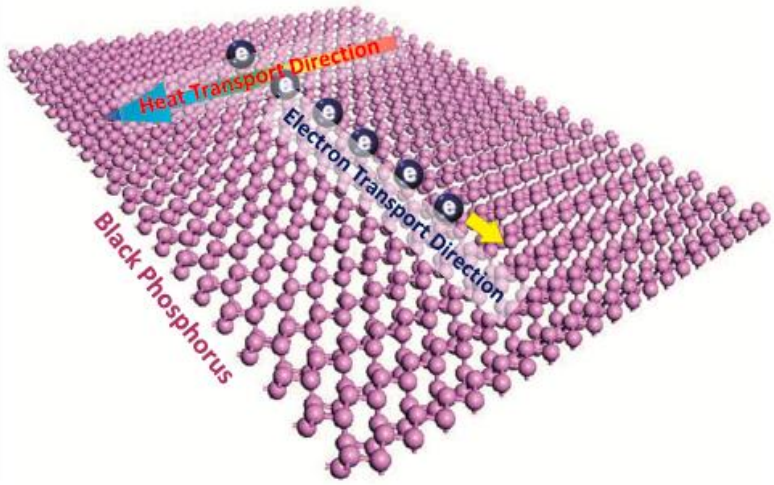

Figure 1.7: Schematic of orthogonal heat and electron transport in b-P. Heat transport is faster along the zig-zag (ZZ) direction, while the electrical transport is faster along the armchair (AC) direction.

The asymmetric effective mass of BP was further identified through field effect transfer measurements. Li et al. fabricated the first monolayer and few-layer BP field effect devices using a global Si back gate and SiO_2 dielectric. Anisotropic hole mobility was measured with x-direction mobility nearly doubling that along the y-direction. Thus in-plane hole transport down the zigzag direction is faster than transport along the armchair direction. Best field effect transistor devices exhibited hole mobilities close to 1000 cm^2/Vs. With increasing temperature, the mobilities decayed with a rate of $-T^{1/2}$, which is consistent with lattice-scattering observed in traditional semiconductors. Layer thickness can also be seen to drastically affect mobility as confirmed by Xia, et al, who saw a nearly two fold increase in hole mobility when increasing channel layer thickness from 8 nm to 15 nm. Additionally sheet conductivity was also seen to depend on layer thickness, with thicker samples displaying large increases in conductivity upon sufficient gate bias as displayed in Figure 1.10. On/off ratios were also measured and determined to exceed 10^5.

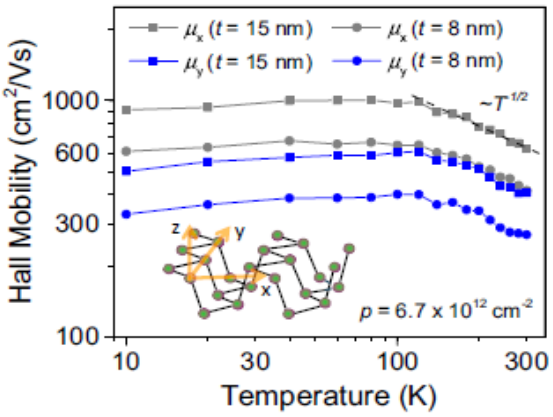

Figure 1.8: Hall mobility as a function of temperature of different sample thicknesses. The squares represent 15 nm thick samples whereas the circles represent 8 nm thick samples. The gray lines are x-direction mobilities while the blue lines represent y-direction mobilities. The inset is a schematic of the in-plane structure of BP with x, y, z axes overlaid.

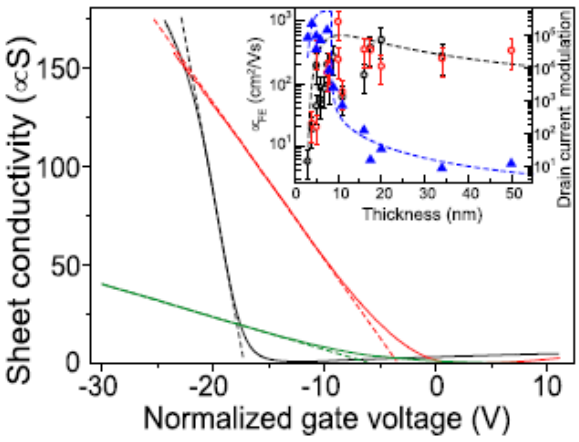

Figure 1.9: Sheet conductivity vs. normalized gate voltage for BP films. Increasing layer thickness is plotted with green, red, and black curves displaying thicker films.

Device operation in the gigahertz frequency has also been demonstrated for BP. Wang et. al fabricated FET devices with structure seen in Figure 1.11. The cutoff frequency was found

to be 12 GHz while the max frequency was 20 GHz. Results demonstrated that BP's finite bandgap made it a superior material for GHz frequency operation as compared to graphene-based devices.

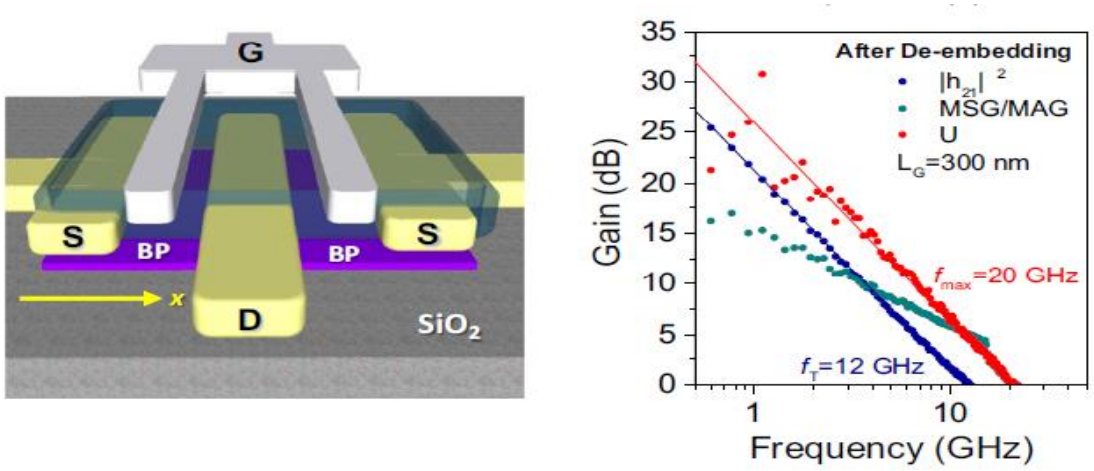

Figure 1.10: Schematic of GHz frequency BP-based devices. Device data showed a maximum cutoff frequency of 12 GHz and a max frequency of 20 GHz.

BP-based FET devices show promising preliminary results despite being in the infancy of its development.[24-28] Most significantly BP offers a reasonable compromise between the properties of graphene and MoS2 with its high hole mobility and finite gap. The high carrier mobility allows for fast device switching while the finite gap yields decent device on/off ratio. A mobility versus on/off ratio plot is shown in Figure 1.12. As demarcated by the figure, BP's application space resides in high-speed flexible electronics. With favorable semiconductor

properties, BP's future implementation in state-of-the-art devices may be on the horizon.

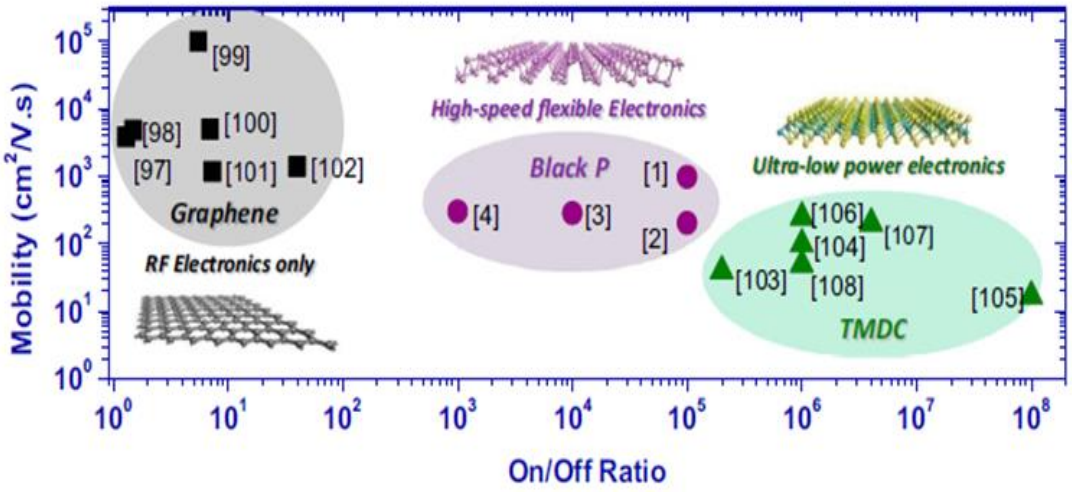

Figure 1.11: Mobility vs On/Off Ratio and the application space of various layered materials. BP boasts both high carrier mobility and a reasonable on/off ratio for FET device operation.

BP readily oxidizes in air, which is detrimental to device performance. The stability of BP has been reasonably well studied despite the novelty of the layered material. It has been demonstrated that layer thickness is directly correlated to reactivity of BP. With increasing layer thickness, the material proves to be more robust, especially with regards to oxidation potential. However, as BP approaches the monolayer limit, the material becomes highly reactive. Hersam et al comprehensively studied BP's reactivity in air via AFM studies.[29] They found that passivation via aluminum oxide Al2O3 prevented oxidation-related degradation and preserved device performance for extended periods of time. A cross-section schematic of their device is shown below in Figure 1.13. Future BP-based devices undoubtedly will require encapsulation for

effective and durable operation.

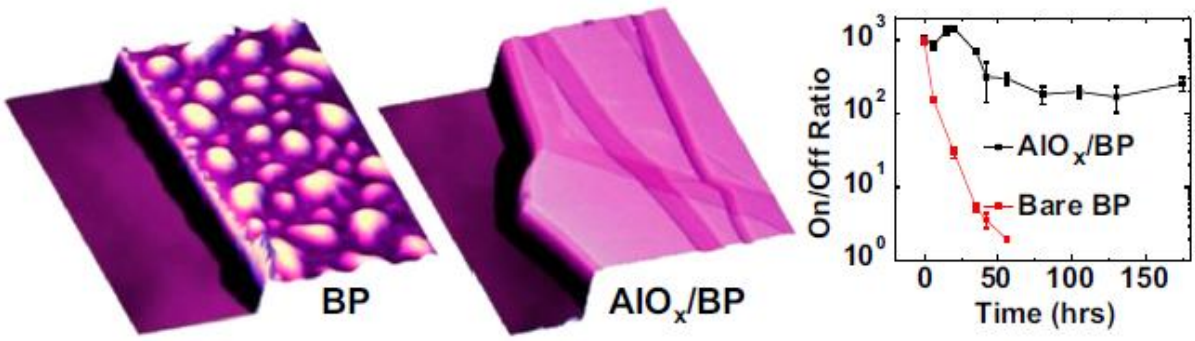

Figure 1.12: Schematic of BP and encapsulated BP along with corresponding FET on/off ratio as a function of time. Encapsulated devices preserve on/off ratio for upwards of 150 hours versus the rapid degradation of on/off ratio for un-encapsulated devices.

1.3 Black Arsenic-Phosphorus

Recently, Liu et al have demonstrated that BP can be alloyed with same group arsenic to yield black arsenic phosphorus (b-AsP). This material maintains the structural identity of b-P by maintaining both the layered anisotropic structure as well as the overall orthorhombic crystal structure. A schematic of b-AsP is shown in Figure 1.14. Again, the in-plane structure is a puckered honeycomb, and exhibits strong covalent bonding. Interlayer attractions are Van der Waal, characteristic of all 2D materials. Notably, alloying BP with As results in an electronic bandgap change as seen in Figure 1.15. With increasing As stoichiometry, the material's bandgap shrinks, reaching a minimum of 0.15 eV. Alloying BP thus effectively allows b-AsP to be used for the long-IR regime, which includes LIDAR (light radar) applications.

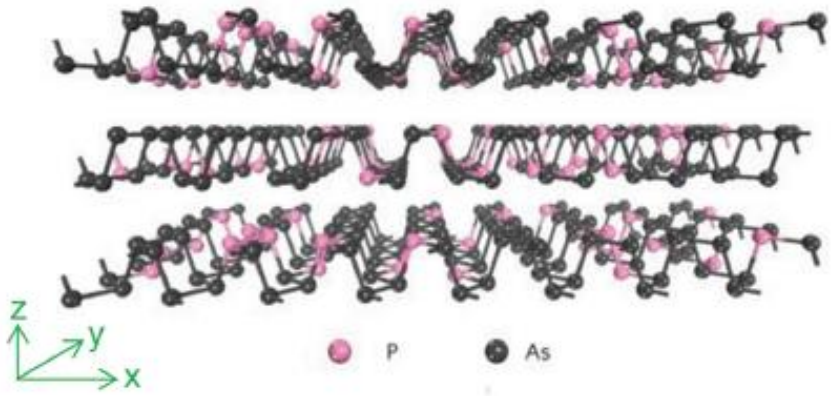

Figure 1.13: Depiction of b-AsP alloy. b-AsP has similar corrugated structure as BP with strong in-plane bonding and weak out of plane layered interactions.

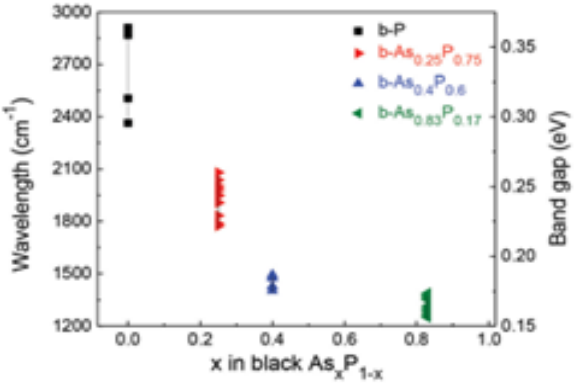

Figure 1.14: Evolving bandgap with increasing As stoichiometry. Samples were measured using FTIR reflection mode. With increasing As content, the bandgap shrinks to a minimum of 0.15 eV.

b-AsP, like the pure elemental phosphorus analogue, also shows anisotropic properties arising from its low in-plane symmetry. Liu et al collected both polarization dependent Raman and FTIR reflection data. The absorption is direction dependent, as depicted in Figure 1.16 where the absorption onset varies as a function of incident light polarization. Optical bandgaps were extracted from the FTIR data Raman signatures were also found to be polarization

dependent in b-AsP. Raman scattering has been studied extensively for the BP analogue, where the three distinct phosphorus vibration modes observed vary in intensity with polarization angle. The in-plane structural anisotropy is the cause of the polarization dependent Raman signatures. Figure 1.17 shows the varying intensities of b-AsP Raman peaks with different polarization angles. At 0° polarization, both the A_g^1 and A_g^2peaks are dampened, whereas the B2g peak is pronounced. However, at 90° polarization, the B_g^2 peak decreases in intensity, while the A_g^1 and A_g^2 peaks are more intense. Further discussion on why the Raman signatures are polarized will be discussed in the experimental section.

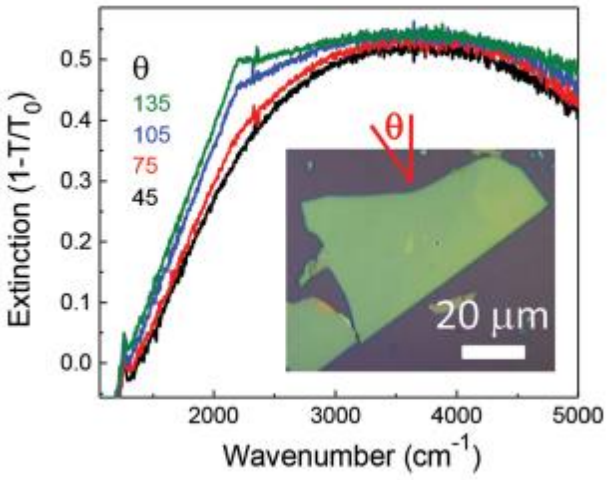

Figure 1.15: Polarization-dependent FTIR spectroscopy. The data was collected in reflection mode and absorption was plotted versus wavenumber. The polarization angle slightly shifts the absorption onset, thus demonstrating polarization-dependent absorption.

Liu et al fabricated b-AsP FET devices to measure the transfer characteristics of the alloy. Similar to graphene, b-AsP was found to exhibit ambipolar transport dependent on gate bias. This is undoubtedly a result of the small yet finite bandgap of the material (0.15 eV). Fermi level tuning via external electric field can result in either hole or electron free carriers. Best

devices exhibited hole mobilities of 110 $cm^2/V*s$ with layer thickness severely affecting transport properties. Current-voltage transfer curves are depicted in Figure 18. Additionally, the on/off ratio of fabricated FET was found to be $1.9 *10^3$. This first generation proof-of-concept device demonstrates the validity of b-AsP as a semiconducting material. The reasonably high mobility and on/off ratio makes b-AsP a promising material for future optimization and incorporation in a variety of micro and nanoscale devices.

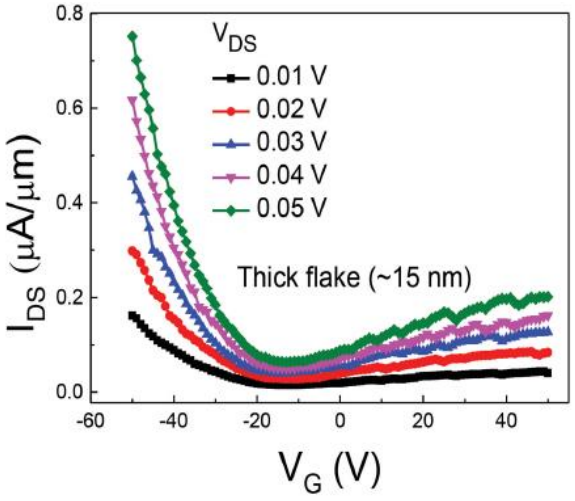

Figure 1.16: Transfer characteristics of b-AsP with varying gate voltage. This device had a channel layer thickness of approximately 15 nm.

1.4 b-P and b-AsP Physics, Devices and Applications

Other than simple transistor architectures, b-P has now been integrated into a variety of different optoelectronic devices. Additionally, novel physics and chemistry has been explored for the b-P material system. This section will serve as a very brief survey of the current status of b-P devices and fundamental physics. This review is by no means comprehensive, and additional resources on b-P can be found in the literature.

1.4.1 Quantum Hall Effect in Black Phosphorus

The quantum Hall (QH) effect is a phenomenom in which a 2D electron system demonstrates quantized Hall conductance. The classical Hall effect is the phenomena in which a voltage is observed orthogonal to the direction of electrical current in a conductor/semiconductor in the presence of an orthogonal magnetic field. In semiconductor physics, the Hall effect is the perhaps the most widely employed method for determining free carrier concentration. Discussions on the classical Hall effect can be found throughout semiconductor physics textbooks as well as in the literature. The quantum Hall effect has ubiquitous applications in electrical engineering and related fields, since exact quantization of Hall resistance in 2-D electron systems (2DES) materials can serve as resistance standards.

Recently, the quantum Hall effect has been observed in black phosphorus-based 2-dimensional hole gas (2DHG).[30] By creating a dual interface with b-P between two hBN layers on top of a graphite back-gate, quantized Hall resistance was observed in b-P. Additionally, the Hall resistance measured was 6000 $cm^2 V^{-1} s^{-1}$, an optimized value due to the effective screening of charged impurities in the 2DHG. The electron sea present in graphite reduced the effective electric field of charged impurities in the 2DHG, thus reducing the magnitude of interactions between free carriers and charged impurities. Figure 1.17 depicts the fabricated device along with the measured Hall resistance. The Hall resistance measurements show behavior ubiquitous for semiconductors. At low temperatures, impurity scattering dominates which decreases the observed mobility. With the effective screening architecture, the impurity effects can be seen to be minimized. At high temperatures, phonon scattering dominates, which is corroborated by the drop in Hall mobility above 50 K seen in Figure 1.18.

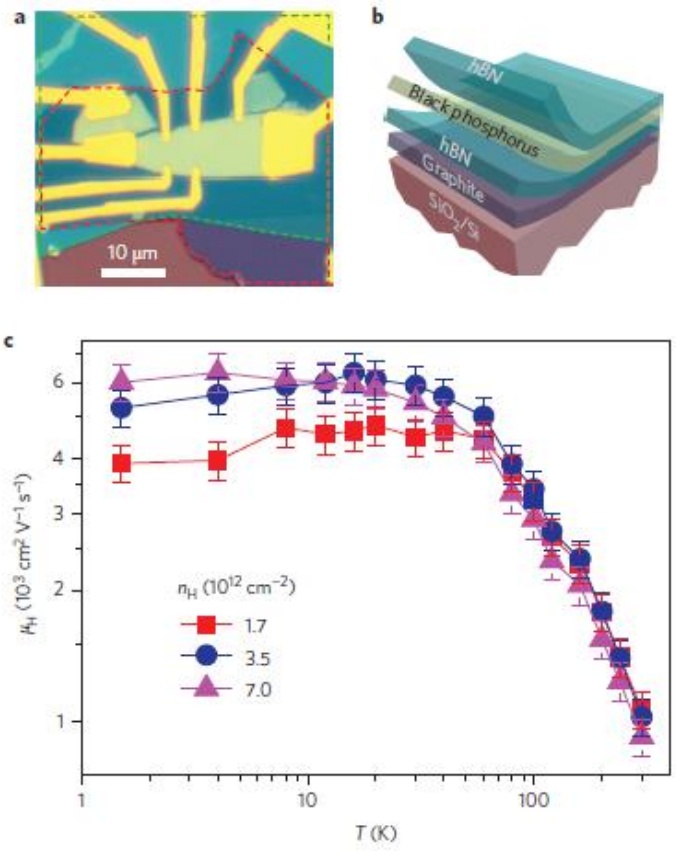

Figure 1.17: Fabricated 2DHG and corresponding Hall mobility measurement. (a) Optical image of heterostructure device. (b) Schematic of device layers. (c) Hall mobility with respect to temperature.

The QH effect is observed in the presence of high magnetic fields in this b-P based device. Typical of integer QH effect materials, the Hall resistance is seen to be quantized at varying magnetic field magnitude according to the relationship $(ve^2/h)^{-1}$ where v is an integer value which represents the filling factor. Figure 1.19 depicts measurements which show the QH effect for b-P in these heterostructures. The QH effect was observed for various hole-doping carrier concentrations, where carriers were gate-induced. In summary, the QH effect is one of many exotic physical phenomena that have been observed in b-P. As a result, ongoing

condensed matter and materials science research in b-P can undoubtedly contribute significantly to the understanding of rapidly growing 2D materials research.

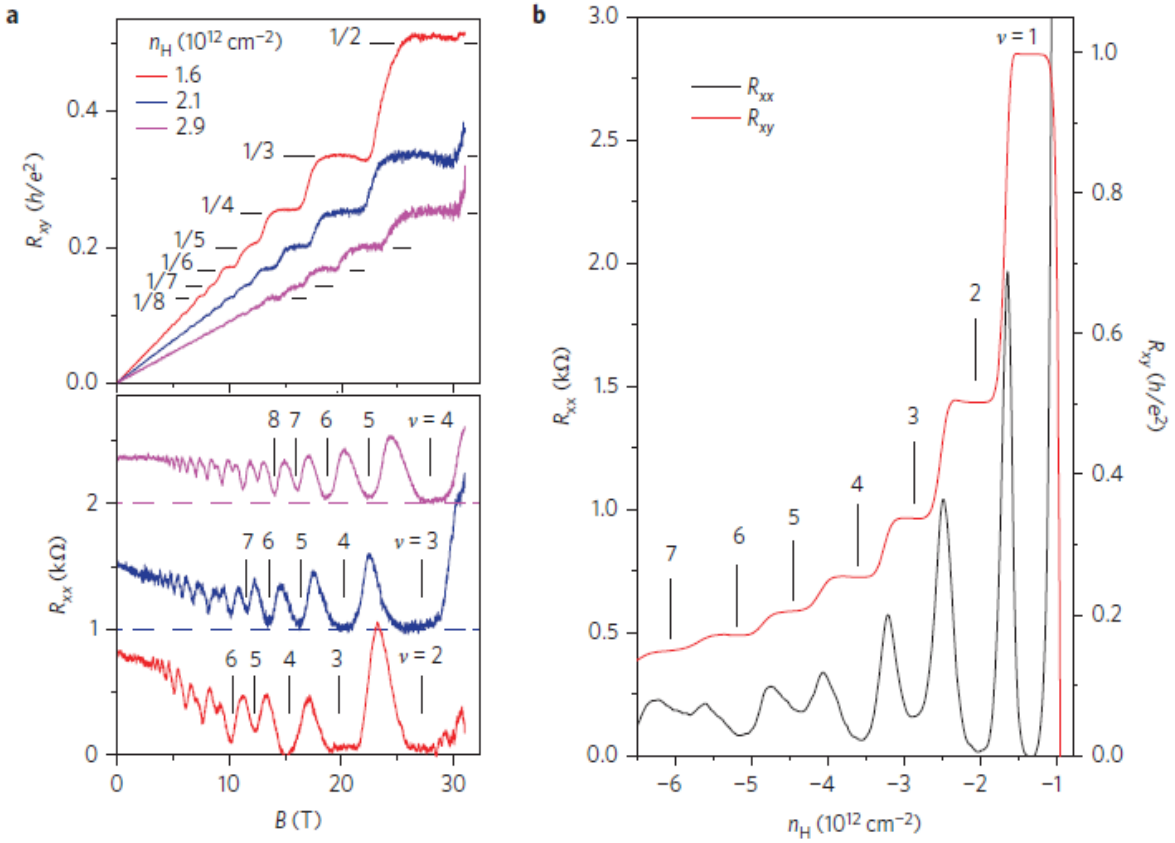

Figure 1.18: Observation of QH effect in b-P/hBN 2DHS. (a) Hall resistance versus magnetic field (upper) and magnetoresistance versus magnetic field for b-P based 2DHS. The different color curves indicate different hole doping conditions induced by the back gate. (b) Hall resistance and magnetoresistance versus carrier concentration.

1.4.2 Amorphous Black Phosphorus Transistor

While most fabricated devices have originated from the micromechanical exfoliation and subsequent placement of b-P onto substrates, some work has been done on fabricating amorphous b-P transistors synthesized via pulsed laser deposition (PLD).[31] The reported method

is performed by ablating a b-P target with a 248 nm KrF pulsed laser while under ultra-high vacuum. The substrate is placed at a distance away from the target such that re-deposition occurs. Unfortunately, a major drawback of this method is the amorphous nature of the deposited film. The metrology results can be seen in Figure 15 below.

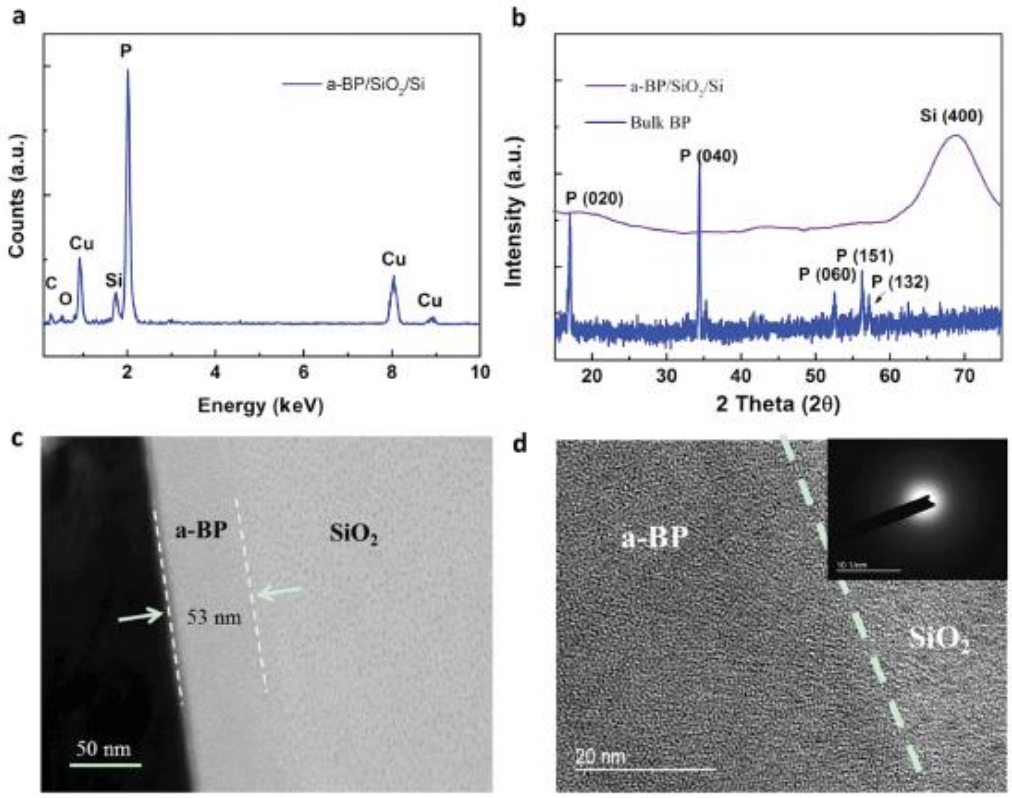

Figure 1.19: Characterization of amorphous b-P film deposited by PLD. (a) EDX spectrum. (b) XRD scan for film stack. (c) Cross sectional TEM of film stack. (d) High resolution TEM cross sectional image. The lack of a well-defined lattice confirms the amorphous nature of the b-P.

The lack of crystalline structure severely limits the device performance, and particularly the field-effect mobility of amorphous b-P FETs. This is the amorphous crystalline structure has no predictable lattice, leading to a variety of defects, thus leading to trap states which severely limit field effect mobility. Additionally, amorphous materials, like ionic conduction, tend to follow different transport mechanisms. As compared to the free-carrier conduction afforded by a

well-defined crystal lattice, amorphous materials, due to electron localization, exhibit electron-hopping mechanisms. Like ionic conduction in solid electrolytes, transport via-hopping is significantly slower than free-electron conduction. As such, the measured field effect mobility was only 14 $cm^2/V*s$ as compared to the 1000 $cm^2/V*s$ mobility obtained from single crystal exfoliated b-P. A schematic of the device as well as the FET transfer curve is depicted in Figure 16.

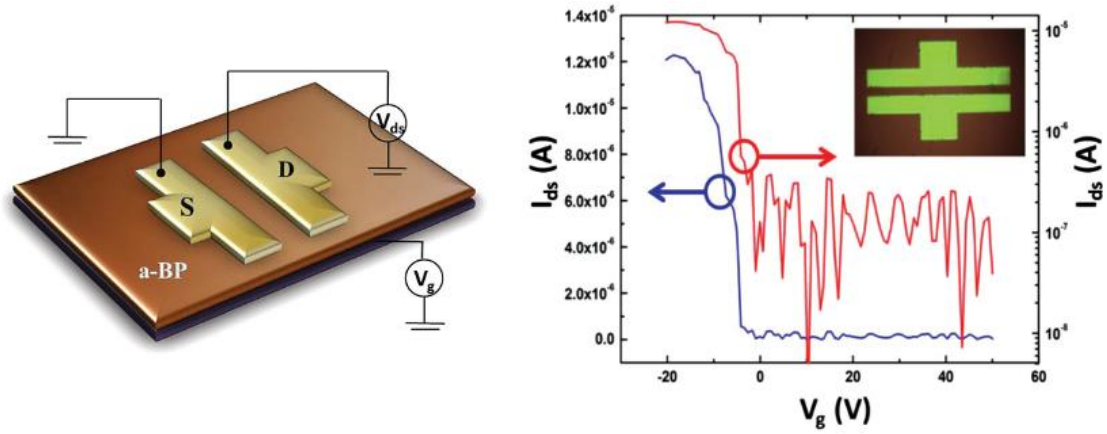

Figure 1.20: (a) Device schematic of back-gated a-BP/SiO2/Si FET. (b) Transfer curve of amorphous b-P transistor. The linear region is extrapolated to give dI/dV which is then used to calculate field effect mobility.

1.4.3 b-AsP Photodetector

b-AsP has recently been demonstrated as a material for mid-infrared (MIR) absorbers. The MIR spans from 3- 50 microns, and has particularly useful application in thermal imaging and sensing. Traditionally, the benchmark MIR detector material is HgCdTe, though the material suffers from several distinct disadvantages including the requirement of cryogenic temperatures for device operation. b-AsP boasts a stoichiometry-dependent, tunable band gap which ranges from 0.3 eV to 0.15 eV in the bulk. As a result, b-AsP can absorb MIR light up to 8.3 μm, extending into the 8-14 μm long-wavelength infrared (LWIR).

Recently, Long et al. have demonstrated the legitimacy of b-AsP as a MIR absorber by fabricating a b-AsP photodetector.[32] The device was comprised of exfoliated b-AsP with stoichiometry $As_{0.83}P_{0.17}$ synthesized from a mineralization assisted vapor condensation. As a result, the bandgap was shown to be 0.15 eV, or 8.5 μm. Devices were encapsulated with PMMA to prevent degradation. Figure 17 below depicts the characterization of the fabricated b-AsP photodetector. The band-edge was at 1250 cm^{-1}, or 0.155 eV and 8 μm while the absorption peak was centered on 2760 cm^{-1} or 3.62 μm. The photodetector was also characterized by measuring photoresponse under MIR 8.05 μm illumination for various source-drain V_{ds} and gate voltages V_g. Two mechanisms dominate photocurrent response, the photovoltaic effect (PVE) and the photothermoelectric effect (PTE), and most of the photocurrent generation occurs at the b-AsP/metal Schottky junction.

The device was also characterized across the entire MIR (2.4 to 8.05 μm) to determine photoresponse at zero bias. All measurements were performed at room temperature, and overall the device boasted a responsivity of 15 to 30 mA W^{-1}. The external quantum efficiency (EQE), or the ratio of photoexcited charge carriers to incident photons was found to be 6.1%. The speed of the photodetector, denoted by the rise/fall time or 10/90% (rise) and 90/10% (fall) was also determined by optical pumping with a 4.034 μm laser and was found to be τ_{rise} = 0.54 ms and τ_{fall} = 0.52 ms. The results can be found in Figure 18.

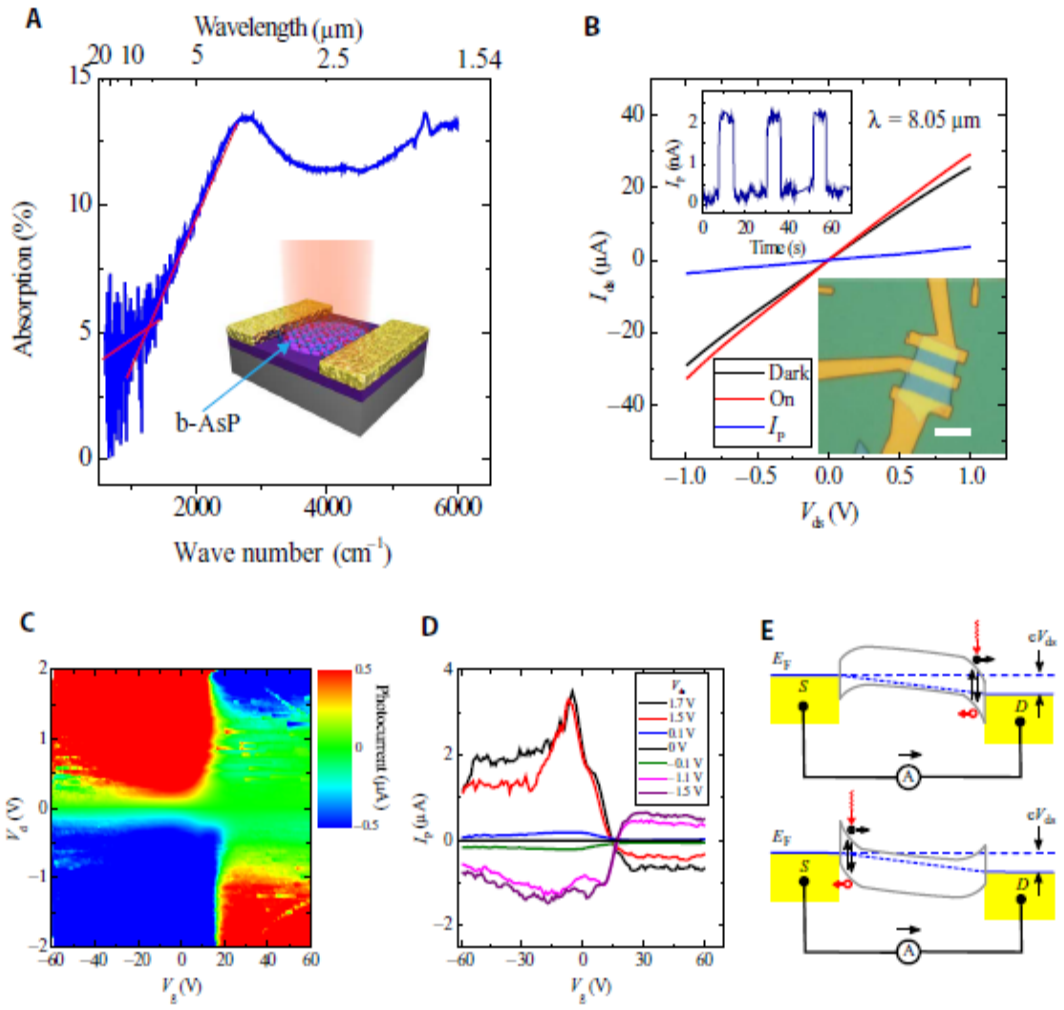

Figure 1.21: (a) Schematic of b-AsP device along with IR spectra showing absorption peak and absorption edge. (b) I_{ds}-V_{ds} response curves for both dark and illuminated scenarios. I_p vs V_{ds} is also plotted, and the inset depicts an optical image of device. (c) V_d versus V_g contour plot. (d) I_p vs V_g for different V_{ds} conditions. (e) Photocurrent generation mechanism for p-type biasing (top) and n-type biasing (bottom).

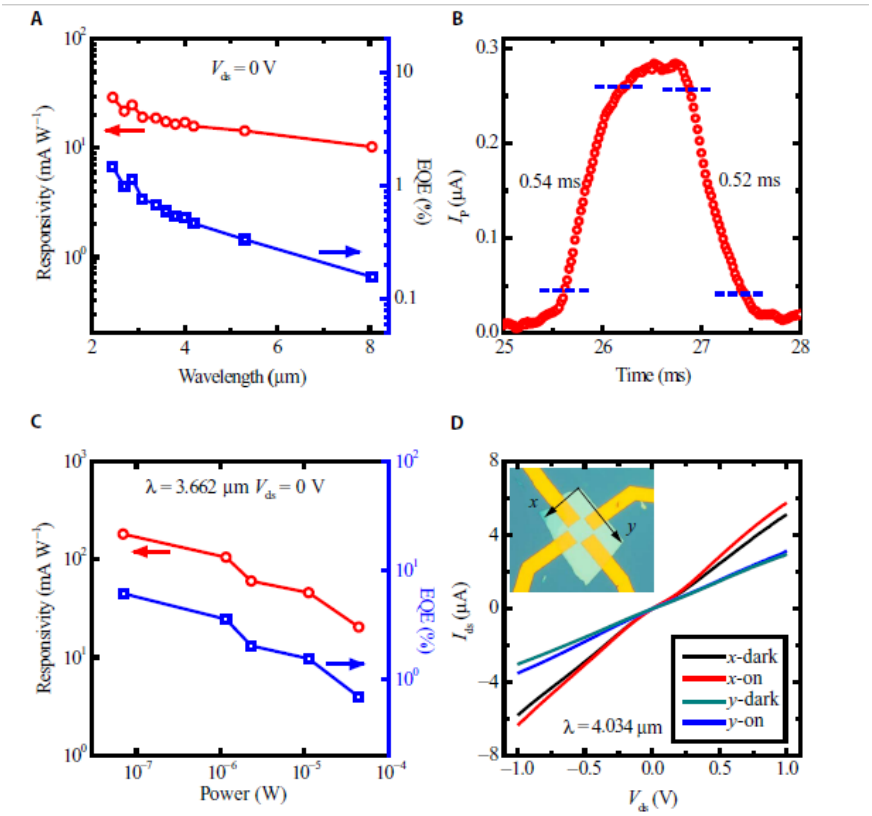

Figure 1.22**:** b-AsP photodetector device characterization. (A) Responsivity and EQE versus wavelength. (B) Photoresponse versus time with rise/fall regions marked with blue lines. (C) Responsivity and EQE versus power. (D) Direction-dependent IV curves for illuminated and non-illuminated devices.

It's important to note why the photoresponse of the b-AsP was slower than theoretical calculations. The authors suggest that the transport of the b-AsP is slower under low-carrier densities because the mechanism differs from high-carrier densities. For low carrier densities, a hopping mechanism similar to ionic conduction is expected, whereas high carrier densities results in band-like transport.

Finally, a b-AsP/MoS_2 heterojunction photodetector was fabricated and was shown to significantly reduce dark current noise. This is because the built in energy barrier that results from creating the heterojunction blocks the ability for electron and hole transport across the

barrier. In addition, the b-AsP/MoS_2 heterojunction was also found to reduce 1/*f* noise which results from defect-driven electronic state fluctuations. The results of the b-AsP/MoS2 photodetector can be seen in Figure 19.

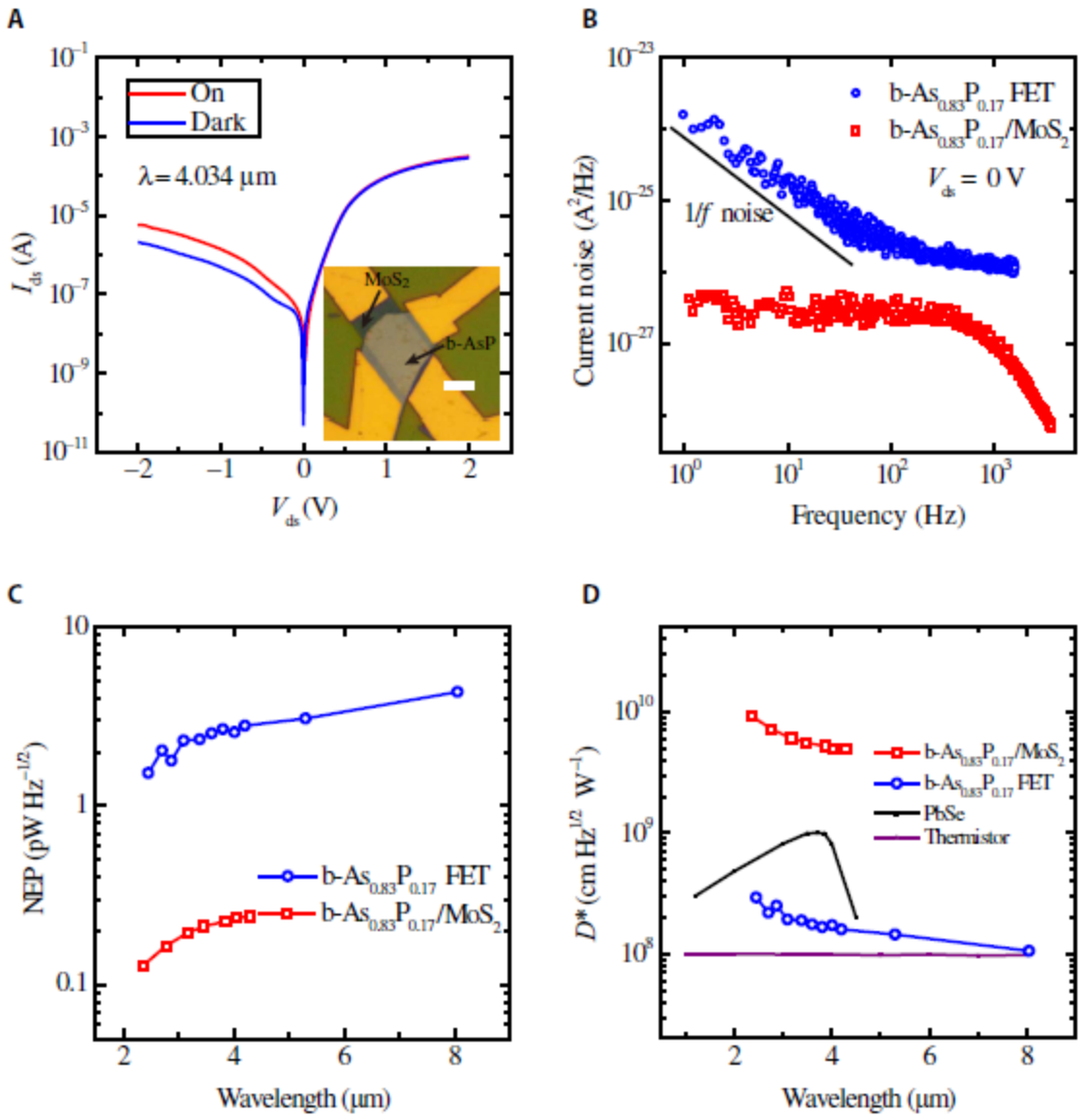

Figure 1.23: b-AsP/MoS_2 heterojunction photodetector. (A) I_{ds}-V_{ds} curves for b-AsP/MoS_2 heterojunction devices under illumination and without illumination. (B) Current noise vs.

frequency for b-AsP vs b-AsP/MoS_2 devices at V_{ds} = 0. (C) Noise equivalent power (NEP) versus wavelength. (D) Specific detectivity versus wavelength for b-AsP/MoS_2 devices.

1.1 Black Phosphorus and b-AsP Synthesis Challenges

1.1.1 b-P and b-AsP Bulk Synthesis

Although both BP and b-AsP exhibit promising properties with a variety of potential applications, the synthesis of both remains challenging. Orthorhombic BP is the most thermodynamically stable allotrope of phosphorus. However, BP is a high-pressure phase which is difficult to synthesize using traditional growth methods. Typically, pressures in the GPas are required to convert the amorphous red phosphorus (RP) into BP. The phase diagram of phosphorus is depicted in Figure 1.25. Of importance is the red/black phosphorus equilibrium. With higher pressures, lower temperatures are required to convert RP to BP. However, it does seem feasible to convert RP to BP with sufficiently high temperatures. Figure 1.26 is an image of bulk black phosphorus as converted by a high pressure approach.

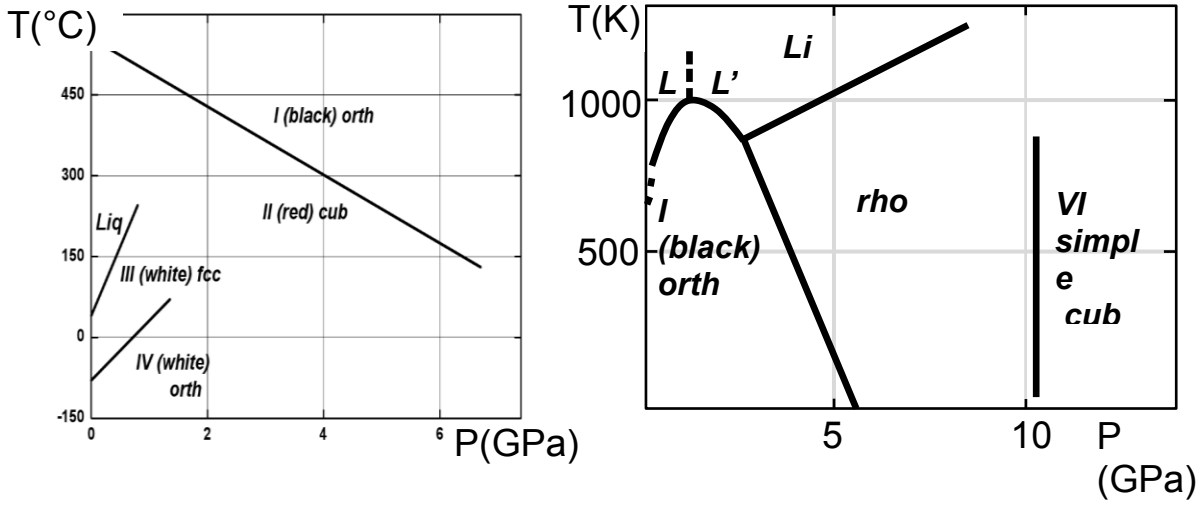

Figure 1.24: Phosphorus Temperature-Pressure phase diagram. Black phosphorus is a high pressure phase with orthorhombic cubic structure. Red is amorphous and white phase is both FCC and orthorhombic.

Figure 1.25: Optical image of bulk BP crystal. Traditional synthesis routes are via high-pressure phase change. Typically elevated temperatures upwards of (200 C) and pressures exceeding 5 GPa are needed to transform from RP to BP.

The b-AsP alloy phase equilibria unquestionably will vary from the pure elemental BP phase diagram depicted above. Alloys often introduce many new phases and solubility restrictions as a result of the inhomogeneous mixing thermodynamics introduced. In contrast, pure elemental materials may be readily described by homogeneous solution thermodynamics. The black As phase has only recently been studied and preliminary DFT calculations have focused on the thermodynamic stability of such a phase. Unlike other alloys, b-AsP contains elements within the same group. Thus the valence of As and P are identical, resulting in similar in-plane bonding. Synthesized b-AsP alloys have been determined to belong to the same crystal structure as BP. In addition, the synthetic conditions for the alloy have been determined to be identical to those for BP. Thus although a reliable phase diagram for the b-AsP system has yet to be constructed, using the phosphorus phase diagram as a synthetic road-map can is useful.

Low pressure, facile synthesis routes for BP as they are cost-effective and simpler as compared with high-pressure routes. In the early 2000s, a patent was filed for the conversion of RP to BP under low-pressure systems via thermal cycling. The reaction times reported is exceedingly long, with ten heating cycles of 16 hours each. Additionally, the three-chambered growth vessel utilized was both complicated and costly. Because BP has only recently been a material of interest, few have attempted to reproduce the low-synthesis method reported by this patent. The discovery of facile synthesis for the laboratory research scale is therefore a necessity for ongoing BP research.

Recently, Nilges et al have reported a low-pressure route towards the synthesis of BP.[33] These reactions exploited the use of metal mineralizers, usually Au or Sn containing, to catalyze the conversion from RP to BP. It has since been proposed that this is a vapor phase reaction where RP converts to P2 vapor before condensing as BP on the catalyst site. Reactions were conducted under moderate vacuum (1*106) and at high temperatures. Early studies using Au catalyst report reaction temperatures exceeding 700 C with reaction times upwards of 24 h. The temperature was ramped to 873K and held there for 23 hours before being cooled to 773K and held for an indefinite time. The reaction was believed to proceed in 5 solid-state reaction steps and reaction enthalpies were calculated. The exact reaction mechanism has yet to be determined, though the efforts of Nigles et al have contributed tremendously to the BP field. More efficient reaction times can be achieved via substitution of Au catalyst with Sn containing catalyst. Figure 21 illustrates the synthetic setup of the low-pressure synthesis approach utilizing a standard solid-state chemistry evacuated quartz tube setup.

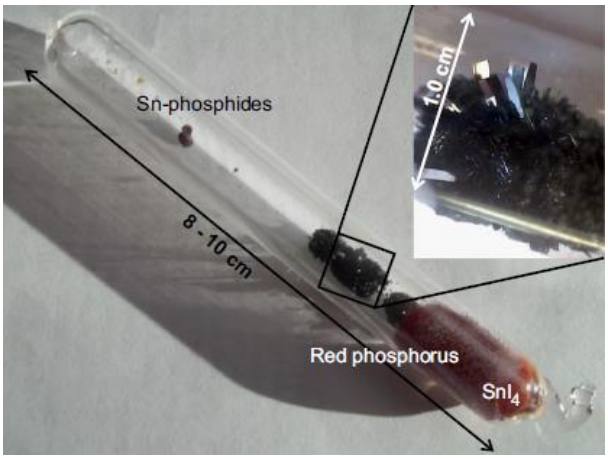

Figure 1.26: Quartz tube setup for the low-pressure mineralization route to BP. RP, and Sn-based mineralizer are loaded into a quartz tube which is subsequently evacuated and sealed. BP crystals are synthesized upstream from the RP with needle-like structure.

The same mineralization route used to synthesize BP was applied to b-AsP.[34] Successful synthesis of b-AsP was achieved, with growth tenability of As content. Because the physical properties of b-AsP are composition dependent, synthetic control of b-AsP results in tunable properties. Figure 22 plots unit cell volume as a function of As composition. Both DFT computational data and experimental results are plotted with a consistent trend of increasing cell volume with As content. This is in line with physical intuition, since although the in-plane bonding is covalent for both the pure elemental form and the alloy, As is a bigger element resulting in longer bond length and thus unit cell volume. The inset is an image of b-AsP crystals, which like their BP analogues, take on a needle-like shape.

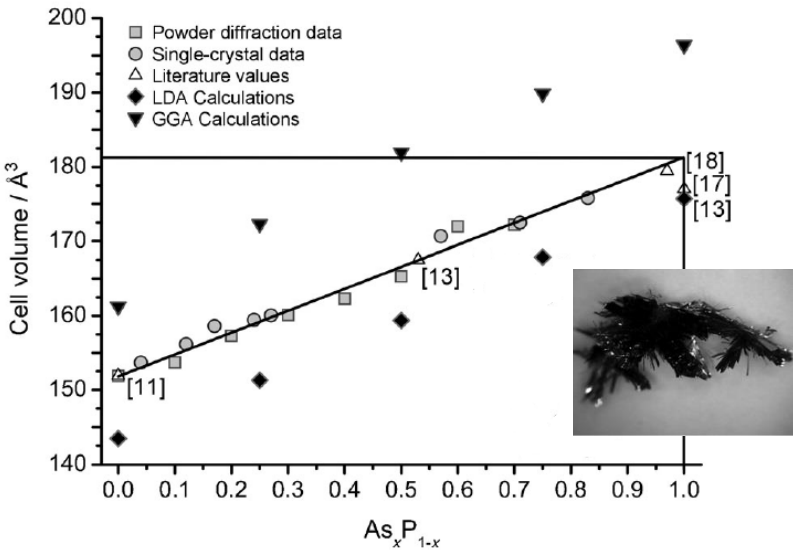

Figure 1.27: Unit cell volume vs As content for b-AsP crystals. Plotted are DFT data, literature values, and bulk single crystal and powder data. The inset is an image showing the b-AsP.

1.5.2 On-Substrate Synthesis of b-P and b-AsP

The future of both BP and b-AsP integration into electronic devices is currently restricted by the limited synthesis methods. While a low-pressure synthesis method has been discovered, there has been no on-wafer synthesis methods reported. Micromechanical exfoliation is nontrivial, unreliable, and irreproducible. Despite being able to isolate few-layer and even monolayer films from bulk single crystal, exfoliation techniques are for not scalable for large scale production. Xia et al have presented a large area synthesis method for BP on a flexible substrate.[27] The synthetic method is presented in **Figure 23**. RP is deposited onto flexible PET substrate via vapor phase deposition. The RP film is then converted to BP under high pressures and some heating using a diamond anvil type setup. Successful conversion was validated by Raman spectroscopy, energy dispersive spectroscopy (EDS), and transmission electron microscopy. Grain sizes on the order of ~10 nm were observed, which resulted in poor field effect mobility. Though this approach does offer an on-wafer approach, the area of converted BP is limited by

the size of the stamp used to apply the pressure. To attain pressures in the GPa regime, low area stamps are utilized with high loads. Furthermore, the method requires extensively long times under load, which limits scalability. For these reasons as well as the overall cost of the tool, the need to devise a simpler yet effective wafer-scale technique is vital.

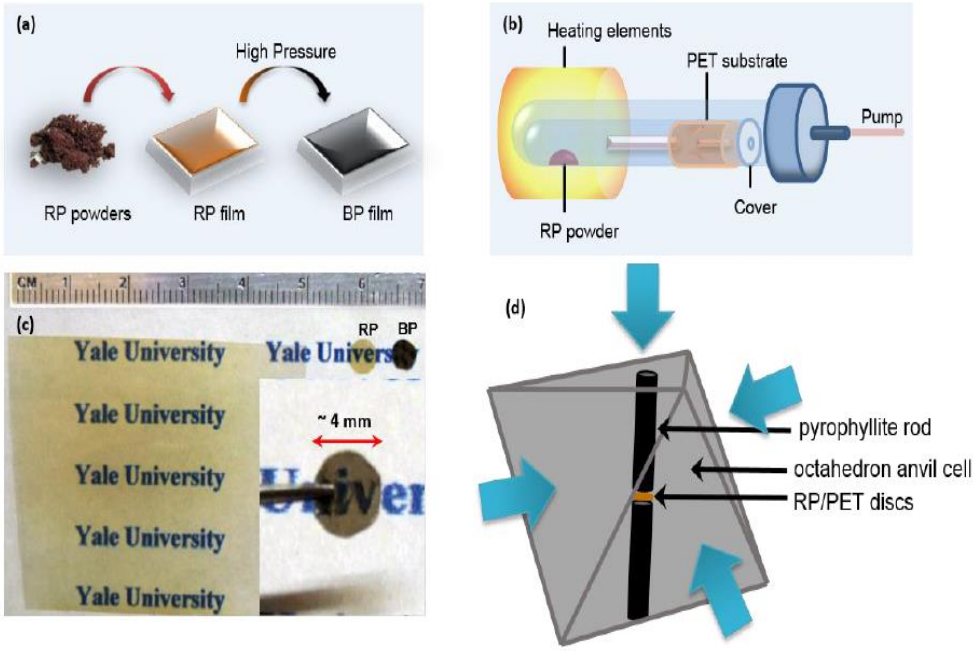

Figure 1.28: Schematic of RP conversion to BP on a flexible substrate. RP powder is deposited onto PET substrate by heating both in a tube furnace. Subsequent conversion to BP is achieved via high-pressure tool.

Very recently, Xia and coworkers have improved their process by synthesizing poly-crystalline black phosphorus on a sapphire substrate. The core method is relatively unchanged, regarding a two-step red phosphorus chemical vapor deposition process followed by a high pressure conversion process. Some key differences from their previous method include depositions on sapphire substrate versus flexible PDMS, as well as the incorporation of an exfoliated h-BN passivation layer to protect the film during conversion. Additionally, the conversion tool used was an end loaded Boyd-England piston cylinder, as compared to a

diamond anvil process. The process conditions were also 1.5 GPa and 700 °C versus 10 GPa room temperature conversion utilized in their previous study. The significant reduction in process pressure affords a larger variety of substrates to be used for future experiments. Most significantly, grain sizes on the order of 70 to 90 μm were reported as compared to the 5 nm nanocrystalline grain sizes yielded in their previous work. As a result of the improved film morphology, field-effect mobilities of 160 $cm^2V^{-1}s^{-1}$ and 200 $cm^2V^{-1}s^{-1}$were achieved at room temperature and 90 K respectively. Figure 24 includes a schematic of their improved process.

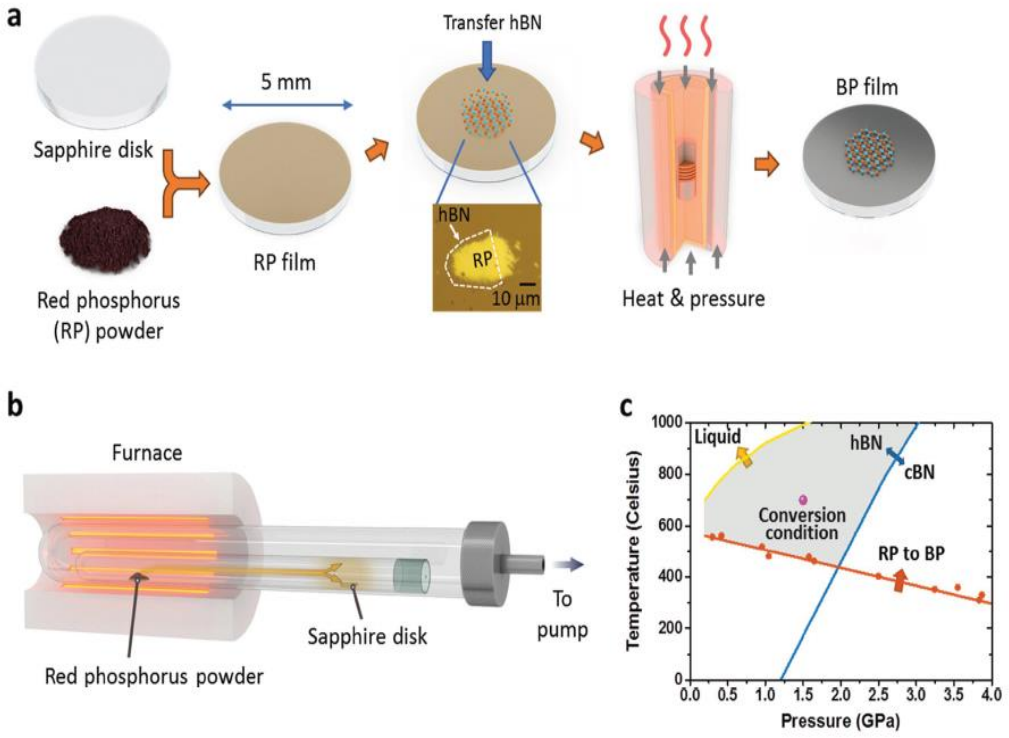

Figure 1.29: Schematic of improved b-P deposition process by Xia et al. (a) Total depiction of process including: deposition of red phosphorus onto sapphire disk, exfoliation of hBN and subsequent transfer, and final conversion process using high-pressure heating tool.

b-P crystallinity was confirmed via high-resolution transmission electron microscopy (HRTEM) as shown in Figure 25. Interestingly, HRTEM images confirmed preferential transformation with respect to the substrate. Specifically, the VdW direction is perpendicular to

the sapphire substrate c-plane, meaning that the in-plane layers lie perfectly flat on the substrate. Additionally, an atomically abrupt, flat transition can be seen between the b-P and hBN layers. This is of importance because this is not an epitaxial process in which the lattice of the substrate promotes the orientation-dependent growth of the film. Rather, upon home-grown vapor deposition, RP is seen to be amorphous on the substrate surface. Thus, the preferential ordering of b-P on sapphire must be a result of the phase transformation process. A possible explanation for the observed results could be that the ordered structure gives rise to the most thermodynamically stable form of b-P on sapphire. Although no real mechanism was proposed as to why the film has a preferential direction, future work exploring this phenomena will be critical to further understanding large-area b-P growth.

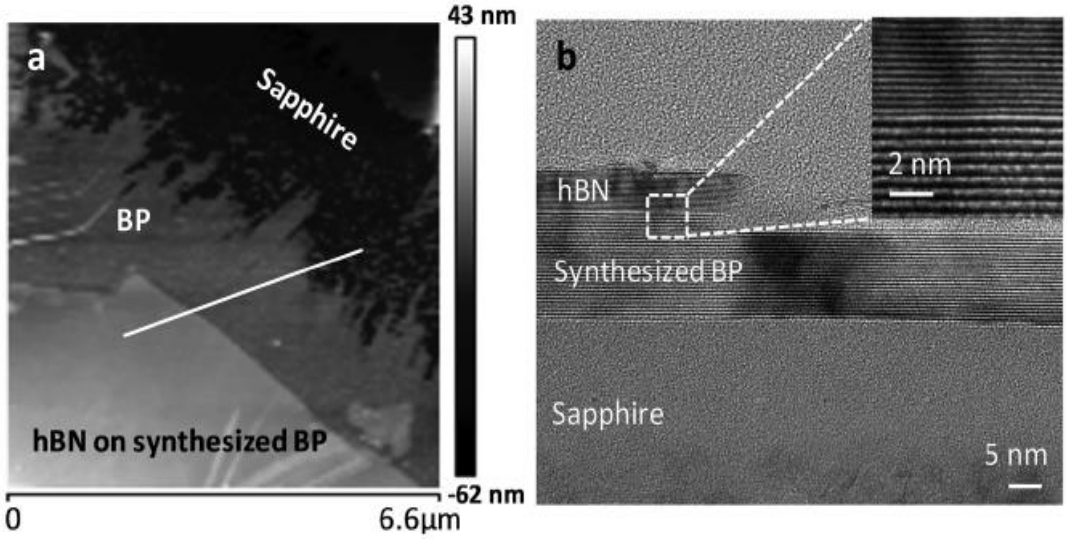

Figure 1.30: AFM and TEM characterization of b-P grown on sapphire (a) AFM image of bP and sapphire pre-conversion. (b) TEM cross-section image of film stack. b-P is preferentially oriented to the sapphire substrate, with c-plane direction parallel to b-P VdW direction. Additionally, an atomically abrupt interface can be seen between b-P and hBN.

A Cambridge group has also recently reported a large-area demonstration of b-P on substrate using inkjet printing.[35] They developed a binder-free ink which allows b-P to be dissolved into low boiling point solvents. As a result, the b-P ink quickly dries, thereby reducing the propensity for oxidation during the process. The method involved the isolation of layered-b-P from the bulk using ultrasound-assisted liquid phase exfoliation (UALPE). Characterization of the UALPE b-P can be seen in Figure 26.

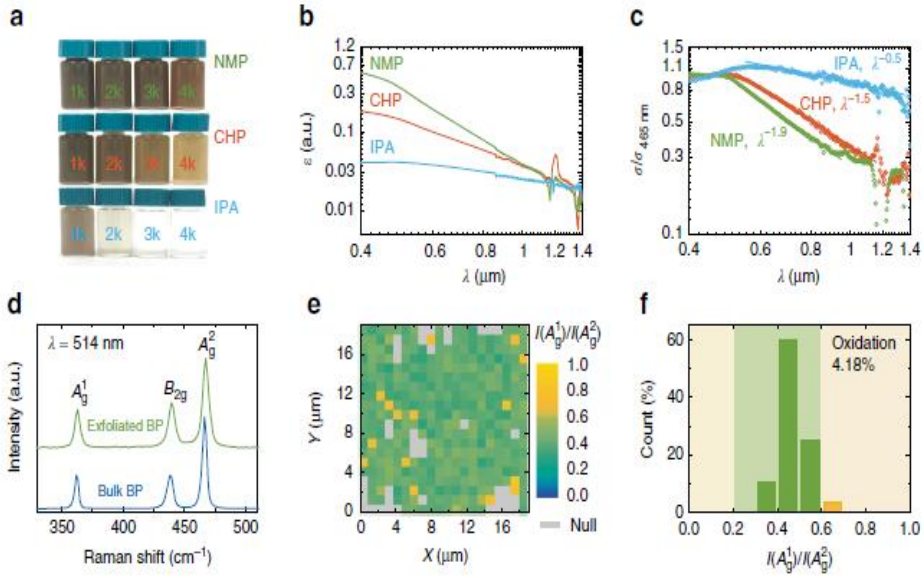

Figure 1.31: Characterization of UALPE b-P. (a) Images of UALPE b-P in various solvents. (b) Optical extinction of the b-P dispersions in various solvents. (c) Optical scattering of the dispersions. (d) Raman scattering spectroscopy spectrum for bulk b-P versus exfoliated b-P. All three solid-solid P modes can be identified. (e) Raman map of exfoliated b-P flake with colorscale displaying A1g/A2g ratio. (f) Counts of A1g/A2g ratio plotted. Ratios below 0.6 have been correlated to denote minimum oxidation (<4.18%).

Printed films boasted excellent uniformity and consistency. Optical extinction and Raman spectroscopy characterization can be found in Figure 27. Electronic devices were fabricated for proof-of-concept demonstrations, though no field effect transistors were made using their thin

films. Instead, a broadband photodetector for visible and near-IR light is reported as well as a saturable absorber. Despite these efforts, b-P deposited via inkjet printing still suffers from the same shortcomings as other printed materials. The most glaring difficulty of inkjet printing is morphology control. Amorphous/polycrystalline b-P has been demonstrated to possess a much lower field-effect mobility as compared to single crystal b-P. This is because grain-boundary scattering significantly decreases the mobility of free carriers in any material. Additionally, the lack of a well-ordered crystal structure further retards free carrier propagation through a solid. Other issues with inkjet printing of b-P as well as other materials include lack of precise synthetic control, as well as batch-to-batch repeatability problems.

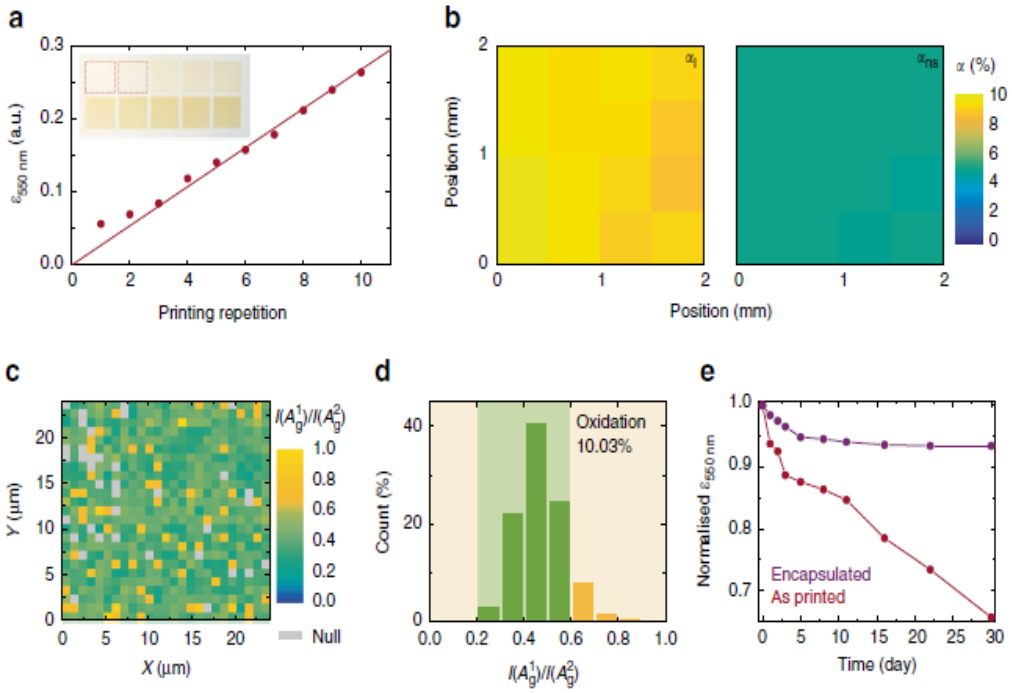

Figure 1.32: Optical extinction and Raman spectroscopy characterization of printed b-P films. (a) 550 nm optical extinction versus printing cycles. (b) Spatial optical absorption characterization plotting spatial linear (α_l) and nonsaturable (α_{ns}) optical absorption coefficient. (c) Spatial raman map plotting A^1_g versus A^2_g intensity ratios. (d) Histogram displaying counts of various

intensities of A^1_g versus A^2_g ratios. (e) Optical extinction coefficient versus time for encapsulated versus non-encapsulated films.

Previous attempts to grow b-P via traditional III-V growth techniques such as molecular beam epitaxy (MBE) have also been reported with limited success. By using Au (111) scaffold along with a b-P seed crystal, Zhang et al. successfully grew a single layer of blue phosphorus.[36] Blue phosphorus was previously predicted to exist by first principles calculations, and like b-P, was expected to behave as a layer-dependent 2D semiconductor. The structure of blue phosphorus as compared to the well-studied b-P system is shown in Figure 28.

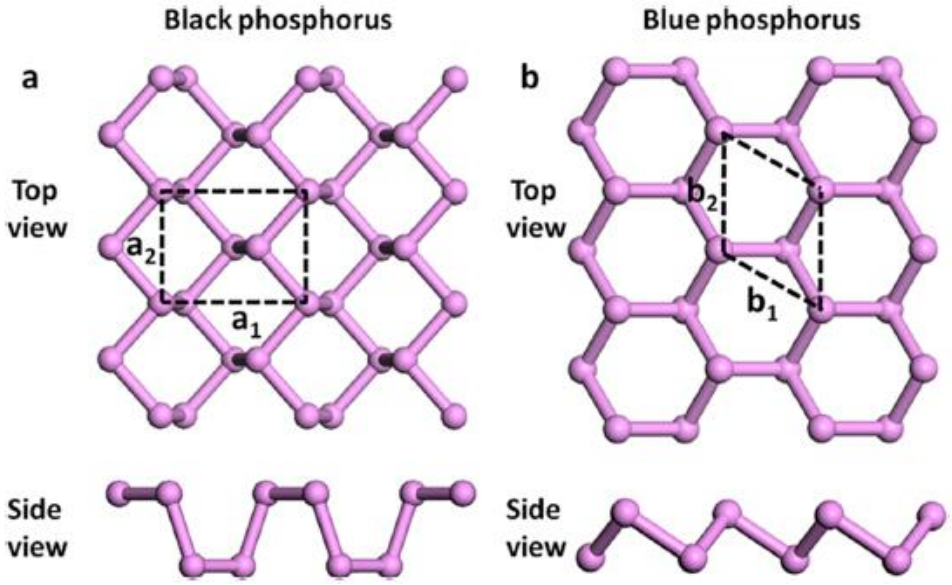

Figure 1.33: Structures of b-P versus blue phosphorus. (a) Black phosphorus in plane and side view. The crystal structure of b-P is orthorhombic, and the side-view structure shows a corrugated sheet. (b) Blue phosphorus crystal structure as shown from top view and side view. The unit cell is shown in the dashed region. Blue phosphorus exhibits a hexagonal crystal structure as compared to the orthorhombic crystal structure of black phosphorus.

It's important to note the structural differences between b-P as compared to blue phosphorus. While both are layered and contain armchair (AC) and zigzag (ZZ) configurations,

the angles and bond lengths are not identical. As a result, b-P and blue phosphorus exhibit different crystal structures. b-P belongs to the orthorhombic family, while blue phosphorus exhibits hexagonal structure. Owing to the difference in physical structure, the transport characteristics of each are likely to differ.

The process involved traditional MBE using an Au (111) substrate that was pre-treated using ion bombardment and subsequent annealing at 500 C. The solid source used in Zhang et al's report is b-P. This is unique as typical phosphorus sources such as those used during InP deposition are charged with solid red-phosphorus. The source cell was heated to 260 C to allow for the slow vaporization of b-P and the substrate was kept at room temperature. Films were annealed at 250 C for 24 h post-deposition. The temperature of the source cell is of significance since it is unusually low. Typically, phosphorus effusion cells are held at upwards of 350 C, and are used in conjunction with a high temperature phosphorus cracker. The cracker serves to convert P4 to dimerized P2 or monatomic P1. The rationale used by the Zhang et al was that black phosphorus is more likely to be formed from P4. However, recent evidence has shown that in contrast, reaction mechanisms for vapor-phase b-P growth involve P2 and P1 precursors. Although no consensus has been reached regarding the exact vapor-phase growth mechanism of b-P, I believe that Zhang et al failed to synthesize b-P because they predicted the incorrect reaction mechanism. STM characterization of their films can be found in Figure 29.

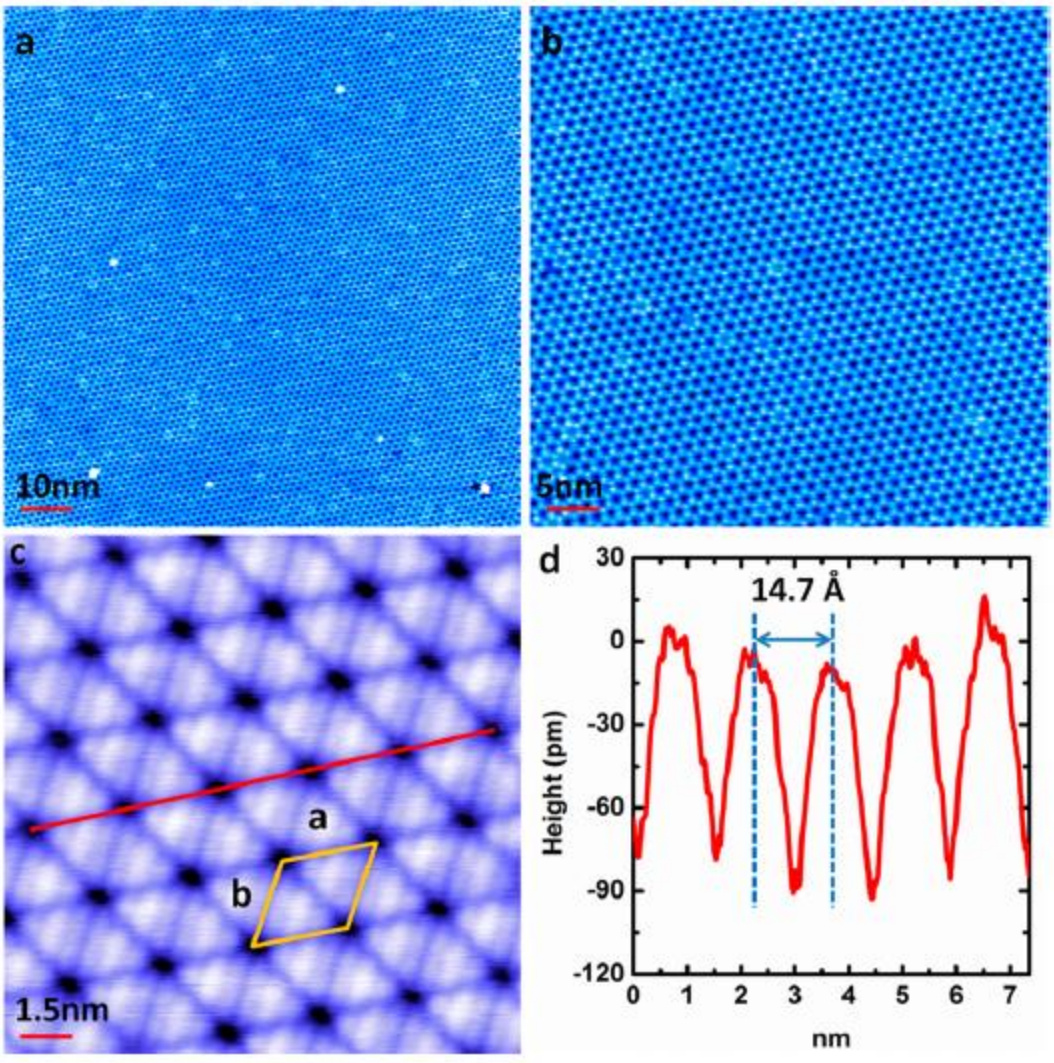

Figure 1.34: Scanning Tunneling Microscopy (STM) characterization of blue phosphorus films. (a) Zoom-out STM image of blue phosphorus. Defects can be visualized. (b) Zoom-in depiction where honeycomb in-plane lattice can be clearly identified. (c) High-resolution STM image with in-plane unit cell depicted. (d) Line-profile scan along corrugated structure. A periodic alternating height can be determined from STM.

Undoubtedly, realization of MBE deposition of b-P and b-AsP has yet to be demonstrated. Because of the highly-controllable, consistent, and clean process of MBE, it is still highly desirable to grow 2D materials via the ultra-high vacuum approach. Although CVD has

been widely and traditionally utilized as the premier growth method for 2D materials, a transition to the more controllable MBE will undoubtedly catalyze and transform 2D materials research. The plethora of novel devices that can be fabricated with monolayer control via MBE will result in applications that have been yet to be realized by traditional bulk materials. In light of the need for more controllable on-wafer growth methods for 2D materials, the subject of this thesis focuses on the molecular beam deposition growth of b-AsP. Synthetic challenges have often been the limiting factor for new material device applications. This work looks to explore a specific such challenge, specifically focusing on the 2D material system of b-P and b-AsP. The hope is that through this work, applications to other layered 2D materials can be realized, thus rapidly

Here, we report a novel synthetic route to synthesizing b-AsP on-wafer. Our two-step approach involves the deposition of thin film b-AsP on 3 ” wafers via molecular beam sources, followed by a post-growth hermetic annealing process. We subsequently characterized both structural and optical properties of our thin films. Chemical compositions of our b-AsP alloys are determined by X-ray photoelectron spectroscopy (XPS) and energy dispersive spectroscopy (EDS). Transmission electron microscopy (TEM) reveals an amorphous film with sparse nanocrystalline grains sized at ~5 nm. Raman spectroscopy measurements confirm signatures consistent with bulk b-AsP, and suggest improved film crystallinity as a result of annealing. Additionally, evidence of conformal, large-area growth is substantiated by Raman mapping. To validate our experimental results, we perform first-principle density functional theory calculations and simulate the Raman spectra for varying composition b-AsP alloys. Our calculations are in good agreement with our experimental results. Using our model, we also predict theoretical bandgap values. Our results are found to match well with previous work. Our

novel growth method is a low-pressure, scalable, and facile on-wafer approach which will promote the rapid integration of b-AsP into a variety of electronic and optoelectronic on-chip devices.

1.6 References

(1) Landau, L. D. Zur Th eorie der phasenumwandlungen II. Phys. Z. Sowjetunion 1937, 11, 26–35.

(2) Landau, L. D. & Lifshitz, E. M. Statistical Physics, 1980, Part I (Pergamon, Oxford).

(3) Peierls, R. E. Quelques proprietes typiques des corpses solides. 1935, Ann. I. H. Poincare 5, 177–222.

(4) Castro Neto, A. H., Guinea, F., Peres, N. M. R., Novoselov, K. S. & Geim, A. K.The electronic properties of graphene. Available at http://arxiv.org/abs/0709.1163, 2007.

(5) Allen, M.J., Tung, V.C., Kaner, R.B. Honeycomb Carbon: A Review of Graphene. Chem. Rev. 2010, 110, 132-145.

(6) Bunch, J. S. et al. Electromechanical resonators from graphene sheets. Science. 2007, 315, 490–493.

(7) Novoselov, K. S. et al. Two-dimensional atomic crystals. Proc. Natl Acad. Sci. USA. 2005, 102, 10451–10453.

(8) Novoselov, K.S. et al. Electric Field Effect in Atomically Thin Carbon Films. Science. 2004, 306, 666-669.

(9) Geim, A.K., Novoselov, K.S., The rise of graphene. Nat. Mat. 2007, 6, 183-101.

(10) Staley, N. et al. Lithography-free fabrication of graphene devices. Appl. Phys. Lett. 2007, 90, 143518.

(11) Zhang, Y., Tan, J. W., Stormer, H. L. & Kim, P. Experimental observation of the quantum Hall effect and Berry's phase in graphene. Nature. 2005, 438, 201–204.

(12) Brey, L. & Fertig, H. A. Electronic states of graphene nanoribbons. Phys. Rev. B. 2006, 73, 235411.

(13) Son, Y.W, Cohen, M. L. & Louie, S. G. Energy gaps in graphene nanoribbons. Phys. Rev. Lett. 2006, 97, 216803.

(14) Zhang, Q., Ganatra, R., Few-Layer MoS_2: A Promising Layered Semiconductor. ACS Nano 8, 2014, 4074-4099.

(15) Mak, K.F. et al. Atomically Thin MoS2: A New Direct-Gap Semiconductor. Phys. Rev. Lett. 2006, 105 136805.

(16) Radisavljevic, B. et al. Single-layer MoS_2 transistors. Nat. Nanotechnol. 2011, 6, 147-150.

(17) Song, L. et al. Large Scale Growth and Characterization of Atomic Hexagonal Boron Nitride Layers. Nano Lett. 2010, 10, 3209-3215.

(18) Li L, et al. Black phosphorus field-effect transistors. Nat. Nanotechnol. 2014, 9(5):372–377.

(19) Xia F, Wang H, Jia Y., Rediscovering black phosphorus as an anisotropic layered material for optoelectronics and electronics. Nat. Commun. 2014, 5:4458.

(20) Liu H, et al. Phosphorene: An unexplored 2D semiconductor with a high hole mobility. ACS Nano. 2014, 8(4):4033–4041.

(21) Koenig SP, Doganov RA, Schmidt H, Neto AHC, Özyilmaz B. Electric field effect in ultrathin black phosphorus. Appl. Phys. Lett. 2014, 104(10):103106.

(22) Rodin AS, Carvalho A, Castro Neto AH., Strain-induced gap modification in black phosphorus. Phys. Rev. Lett. 2014, 112(17):176801.

(23) Qiao J, Kong X, Hu Z-X, Yang F, Ji W High-mobility transport anisotropy and linear dichroism in few-layer black phosphorus. Nat. Commun. 2014, 5:4475.

(24) Churchill HOH, Jarillo-Herrero P., Two-dimensional crystals: Phosphorus joins the family. Nat. Nanotechnol. 2014, 9(5):330–331.

(25) Liu H, Du Y, Deng Y, Ye PD. Semiconducting blackphosphorus: Synthesis, transport properties and electronic applications. Chem. Soc. Rev. 2015, 10.1039/C4CS00257A.

(26) Guo, Q. et al. Black Phosphorus Mid-Infrared Photodetectors with High Gain. Nano Lett. 2016, 16, 4648–4655.

(27) Li, X. et al. Synthesis of Thin-Film Black Phosphorus on a Flexible Substrate. 2D Mat. 2015, 2, 031002.

(28) Liu, B. et al. Black Arsenic-Phosphorus: Layered Anisotropic Infrared Semiconductors with Highly Tunable Compositions and Properties. Adv. Mater. 2015, 27, 4423–4429.

(29) Ling, X., Wang, H., Huang, S., Xia, F. & Dresselhaus, M. S. The renaissance of black phosphorus. Proceedings of the National Academy of Sciences. 2015, 112, 4523–4530.

(30) Li, L. et al. Quantum Hall effect in black phosphorus two-dimensional electron system. Nat. Nanotech. 2016, 11, 593-597.

(31) Yang, Z.; Hao, J.; Yuan, S.; Lin, S.; Yau, H. M.; Dai, J.; Lau, S. P. Field-Effect Transistors Based on Amorphous Black Phosphorous Ultrathin Films by Pulsed Laser Deposition. Adv. Mater. 2015, 27, 3748–3754.

(32) Long, M. et al. Room Temperature high-detectivity mid-infrared photodetectors based on black arsenic phosphorus. Science Advances. 2017, 3: e1700589.

(33) Nilges, T. et al. A fast low-pressure transport route to large black phosphorus single crystals. J. Solid State Chem. 2008, 181, 1707-1711.

(34) Osters, O. et al. Synthesis and Identification of Metastable Compounds: Black Arsenic – Science or fiction? Angew. Chem. Int. Ed. 2015, 51, 2994-2997.

(35) Hu, G. et al. Black phosphorus ink formulation for inkjet printing of optoelectronics and photonics. Nat. Commun. 2017, 8.

(36) Zhang, J.L. et al. Epitaxial Growth of Single Layer Blue Phosphorus: A New Phase of Two-Dimensional Phosphorus. Nano Lett. 2016, DOI: 10.1021/acs.nanolett.6b01459.

Chapter 2: Molecular Beam Deposition of b-AsP

2.1 MBE Fundamentals

Although silicon complimentary metal-oxide semiconductor (CMOS) technology has dominated the semiconductor industry, compound semiconductors such as III-V and II-VI have distinct advantages over Si in many different electronic and photonic device architectures.[1] Light emitting diodes (LEDs), high power and high frequency metal semiconductor field effect transistors (MESFETs), high electron mobility transistors (HEMTs), semiconductor lasers, quantum cascade lasers (QCLs), photodetectors, and photovoltaics all require high-quality crystalline III-V semiconductor materials for device operation.[2] III-V compound semiconductors have significant synthetic challenges as compared to the well-developed, economic, and relatively facile synthesis of Si crystal. Epitaxial methods are employed toward depositing III-V materials on wafer. Epitaxy is a growth process in which the substrate serves as a seed crystal for the deposited thin film.[3] The substrate is lattice matched to the thin film, thereby minimizing strain free-energy contributions which allows for thermodynamically favorable growth.

Molecular beam epitaxy (MBE) is a suitable technique for the effective fabrication of III-V semiconductors and heterojunctions as it enables the synthesis of ultra-clean, single crystal, epitaxial films with precise chemical, dopant, and thickness control. [4-7]

Classically, molecular beam epitaxy (MBE) has been utilized to grow III-V semiconductors with monolayer control. MBE is a growth process conducted in ultra-high-vacuum (UHV) conditions. Source material can either be solid or liquid, and effusion rates can be controlled by the modifying the temperature of the source cells. Because growth is conducted under UHV, the mean free path of the effusing species is longer than the source to substrate

distance, resulting in unmixed and unperturbed beams. Additionally, the effusion flux rates are slow enough to afford monolayer control during growth, and film evolution can be monitored using reflection high-energy electron diffraction (RHEED). Traditional MBE employs epitaxial growth, where the deposited film is lattice matched to the substrate. This minimizes substrate-film strain, and makes growth more both more thermodynamically favorable and stable. Typically, the substrate is heated during growth which improves film quality by providing necessary driving force for film diffusion. A variety of solid-sources can be used, which provides the basis for various thin-film stacks and architectures. Thus because MBE growth is highly controllable and produces high-quality crystalline fields, the technique continues to be the method of choice for III-V material fabrication.

2.2 MBE for b-AsP Growth

Here, MBE is used to deposit AsP alloys. A schematic of the MBE deposition is shown below in **Figure 24**. The sources used are solid source As and P. Te is shown in Figure 24 because it is a possible BP and b-AsP dopant. Our MBE is pumped to UHV environment by cryogenically cooled ultrahigh vacuum and has 100 mm wafer capability. Other than Te, a variety of group IV/ and VI dopants are available for use. In addition to single compound b-AsP films, monolayer control of epitaxial layers allows for fabrication of heterostructures for a variety of device applications. In general, depositions were performed with no-substrate heating in order to avoid delamination of the deposited phosphorus. However, blackbody heating from the open-shutter sources resulted in measured substrate temperatures of 25-50 °C. Deposition times varied between 1 and 4 hours, with typical P fluxes of 10^{-7} and As fluxes of 10^{-8}.

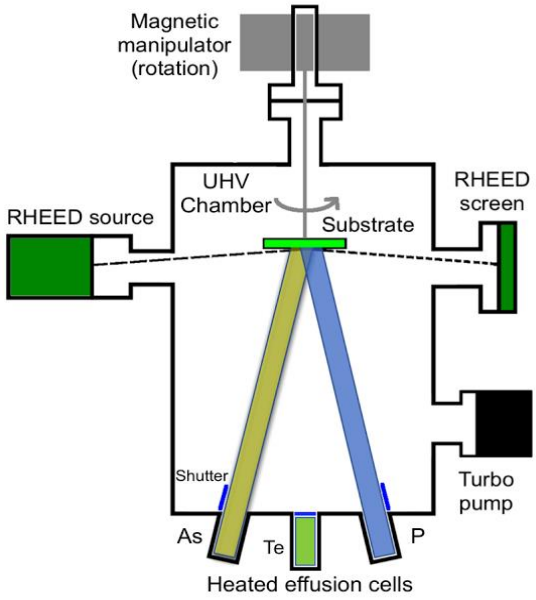

Figure 2.1: MBE schematic showing solid source As and P along with Te dopant. RHEED is used to track progress of growth, and the entire chamber cryogenically is pumped to UHV conditions.

As discussed above, the suspected vapor phase conversion from RP to BP is believed to occur through the cracking of phosphorus. White phosphorus (WP) exists in a P_4 molecular state consisting of four phosphorus atoms. High temperatures results in the dissolution of the P_4 molecule into gaseous P_2 molecules or single P atoms. To mimic the reaction conditions described in the solid state chemistry literature, we employ the use of a phosphorus cracker as seen in Figure 2.2. Here, solid RP is placed in a charging container and transformed to white phosphorus at 400 °C upon use. The white phosphorus is subject to a second high temperature heater which ensures that WP remains in the vapor phase. The gaseous WP diffuses along a high temperature cracking zone where P_4 is cracked to P_2 and P_1 before leaving the nozzle and transporting to the substrate.

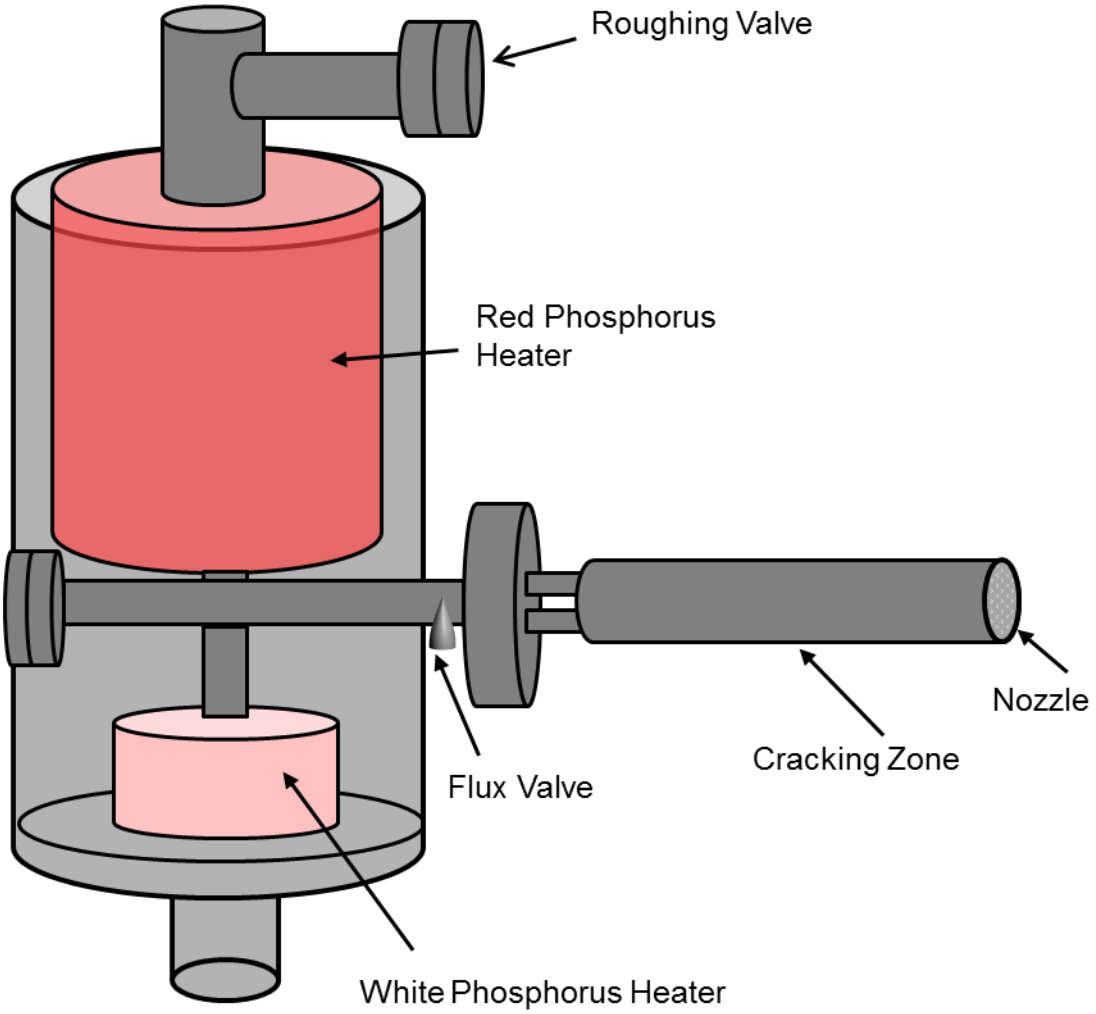

Figure 2.2: Schematic of phosphorus cracker showing RP heater, WP heater, flux valve, and racking zone. The overall reaction is the transformation of amorphous RP to elemental P or P2 molecules.

Depositions on a variety of substrates were performed as seen in Figure 2.3, all with growth times of 2 h. Because BP is a layered material, there is assumed to be no intramolecular bonding between the film and the substrate characteristic of epitaxy. The current 2D material community is undecided on the validity of so-called “van der Waal epitaxy”. With this in mind, substrate structure is expected to have limited influence on deposition. Because the films are so thin, deposition was not visible to the naked eye on all substrates. For all growths, the P_2 flux

was approximately one order of magnitude larger than the As flux. This resulted in the most successful growths. Although the P

Substrate	Prep T (° C)	Dep. T (° C)	P_2 flux (Torr)	As_2 flux (Torr)	Dep. time (min)	Deposition optically visible
SiO2/Si	850	~36	7.1E-07	7.1E-08	120	no
SiO2/Si	850	~35	7.1E-07	7.1E-08	120	no
SiO2/Si	850	~38	1.8E-06	1.8E-07	120	no
InP	680 (~510 actual?)	~50	7.1E-07	7.1E-08	120	no
InP	680 (~510 actual?)	~38	7.1E-07	3.5E-08	120	no
InP	680 (~510 actual?)	~39	7.1E-07	2.2E-08	120	no
InP	680 (~510 actual?)	~38	1.4E-06	2.2E-08	120	no
InP	680 (~510 actual?)	~44	7.1E-07	7.1E-08	120	no
Sapphire	450	200	7.1E-07	7.1E-08	120	no
Sapphire	450	~55	7.1E-07	7.1E-08	120	no
Sapphire	850	~49	7.1E-07	7.1E-08	120	
GaAs	808 (625 actual)	~47	7.1E-07	7.1E-08	120	no
GaAs	808 (625 actual)	~37	7.1E-07	3.5E-08	120	no

Figure 2.3: Depositions on a variety of substrates with respective process conditions. All depositions were prepped for deposition with a bake to drive off low-boiling point impurities. Depositions were done without substrate heating with fluxes of 10^{-7} for P_2 and 10^{-8} for As. Deposition times were 2 hours.

2.3 As-Deposited Characterization

In order to validate the success of the deposition, the wafers were immediately characterized using a variety of different methods. To obtain composition, we performed X-ray photoelectron spectroscopy (XPS). This method was chosen over energy dispersive spectroscopy (EDS) due to its surface sensitivity. Because some of the substrates included either As or P, EDS is an inappropriate technique as substrate signals would be detected since the detection limit of EDS is approximately one micron. In contrast, XPS has a detection limit of approximately 10 nm since the escape depth of the photoelectron is shallow due to small electron mean free path.

This section will focus on the characterization of films grown on InP. Preliminary results for this b-AsP on InP stack were most promising, thus the system received additional attention. Figure 2.8 is a schematic showing the stack studied and Figure 2.9 depicts the both the XPS spectra and a table with the corresponding composition calculations. We looked for signals from several expected elements: As, P, C, In, and O. Because the samples were stored in inert environments before measurement, no oxygen peaks were detected indicating that the film was pristine with no evidence of oxidation. Carbon is expected in all XPS measurements, and was subtracted to obtain the final alloy composition. Indium peaks were also examined but only minimal signals were detected, which indicated that there was no indium in the film layer.

To obtain accurate AsP alloy composition, we compared and contrasted several core-shell peaks for both elements. For arsenic, we looked at the 2p3 and 3d peaks and for phosphorus we scanned the 2p and 2s peaks. The alloy composition for films grown on InP with phosphorus flux 7.1 E-07 and As flux 7.1 E-08 was determined to be $As_{0.78}P_{0.22}$.

Figure 2.4: Schematic of AsP films grown on InP. The thickness was characterized by x-ray reflectivity. Wafer was directly loaded into diffractometer without dicing for XRR measurements.

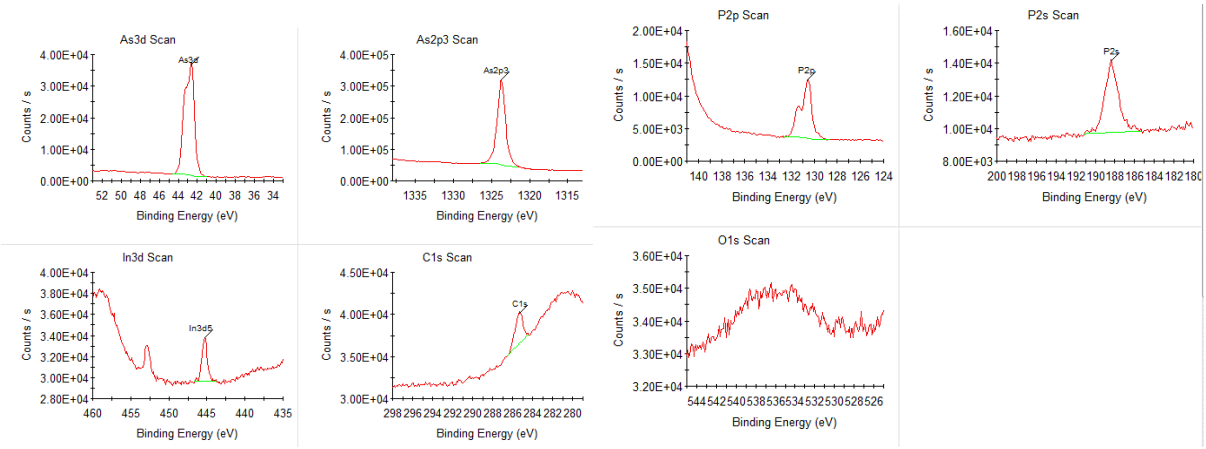

		Concentration (Atomic %)				
Sample	**Spot**	**As**	**P**	**In**	**C**	**O**
As-P Control	1	70	21	0.5	9.4	-
	2	71	20	0.4	9.0	-
	3	70	20	0.6	9.4	-

Figure 2.5: XPS spectra and table showing atomic percentage of scanned elements. XPS measurements give alloy concentrations on this film structure as $As_{0.78}P_{0.22.}$

In order to study the degradation of b-AsP, we performed XPS measurements after exposing the films to air for upwards of three days. Like its pure phosphorus analogue, b-AsP readily oxidizes in air as shown by XPS measurements in Figure 2.10. Phosphorus 2p peaks were scanned, and a peak consistent with phosphorus oxide was identified at the surface of the sample. In Figure 2.10, we see a total of four major peaks, the phosphorus-oxide peak, the elemental phosphorus peak, the InP phosphorus peak, as well as a broad signal which corresponds to the mixing of the InP phosphorus and elemental phosphorus peak. The reason for the changes in binding energy can be rationalized by elementary orbital bonding theory.

In order to understand the evolution of film composition with depth, XPS depth profiling was performed using an in-situ sputter system. The sputter rate was approximately 1nm/second with XPS measurements taken every 10 seconds. Figure 2.11 plots XPS spectra centered on the phosphorus 2p peak. The red line indicates signal taken at 0 etch seconds, while the teal curve and the dark blue curves represent spectra accumulated at 9 seconds and 27 seconds respectively. At 0 etch seconds, core shell peaks corresponding to both elemental P and P-oxide were detected indicating surface oxidation. At sputter time of 9 seconds, XPS emissions were detected consisting of a mix between elemental 2p P and 2p InP peaks, corresponding to signal from both the growth layer as well as the underlying InP substrate. XPS at 37 seconds sputtering revealed solely 2p core-shell signal corresponding to InP. Thus the XPS depth profiling indicates that our b-AsP films, like BP, readily oxidize in air. Figure 30 is a plot illustrating the XPS depth profile experiment by plotting various elemental compositions as a function of sputter depth.

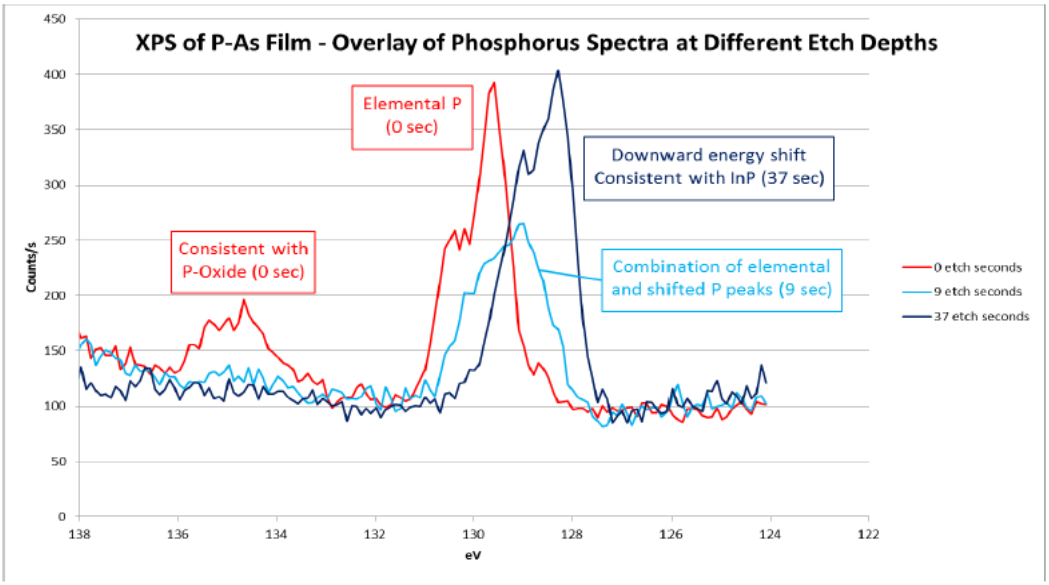

Figure 2.6: XPS measurements centered on the P 2p peak. The spectra at three different etch depths are depicted. The approximate etch rate is 1 nm/sec but is substrate dependent.

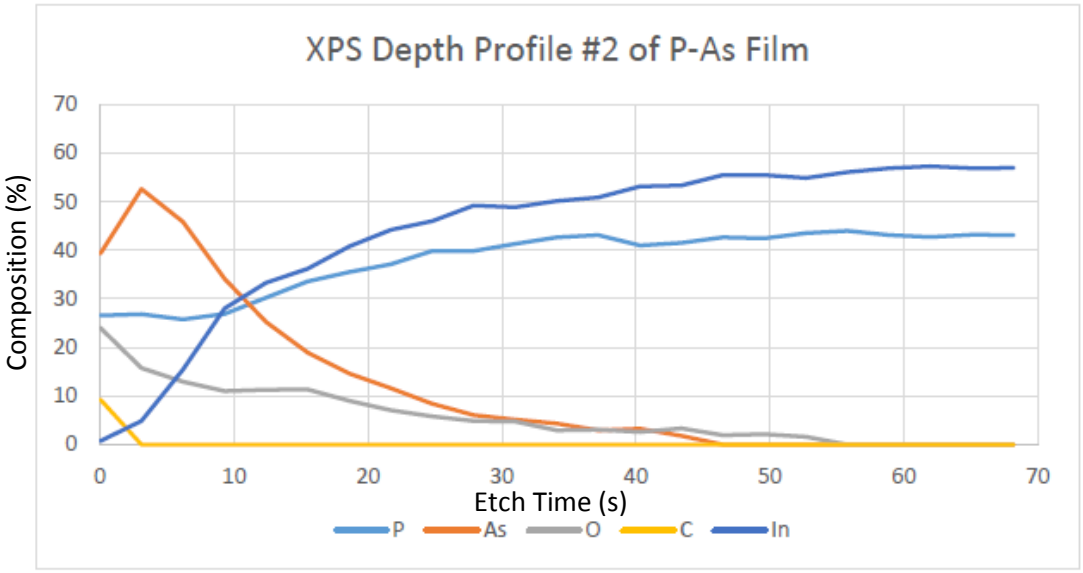

Figure 2.7: XPS depth profile displaying various expected elements. Plotted is % composition which is correlated with % counts versus etch time.

2.4 Substrate Heating During Cold MBE Deposition

Our growths were conducted in the absence of substrate heating. Because the substrate holder is cryogenically cooled, the starting temperature indicated by the thermocouple typically displayed a temperature of -28°C. It's important to note that the thermocouple is located at the back of the substrate. Thus, if the substrate is not a good conductor, a temperature gradient may be present in which the actual temperature at the front of the substrate is hotter than the readout displayed by the thermocouple. In Figure 26, the temperature listed is the final readout temperature after 2 h of growth. Depending on the substrate, the final temperature varied from 30-50°C. This is because of the radiative heating experienced from the open As and P shutters. The temperature during growth is perhaps one of the most important factors in determining growth for b-AsP. This is because of the low vapor pressure of phosphorus as seen in Figure 27 below:

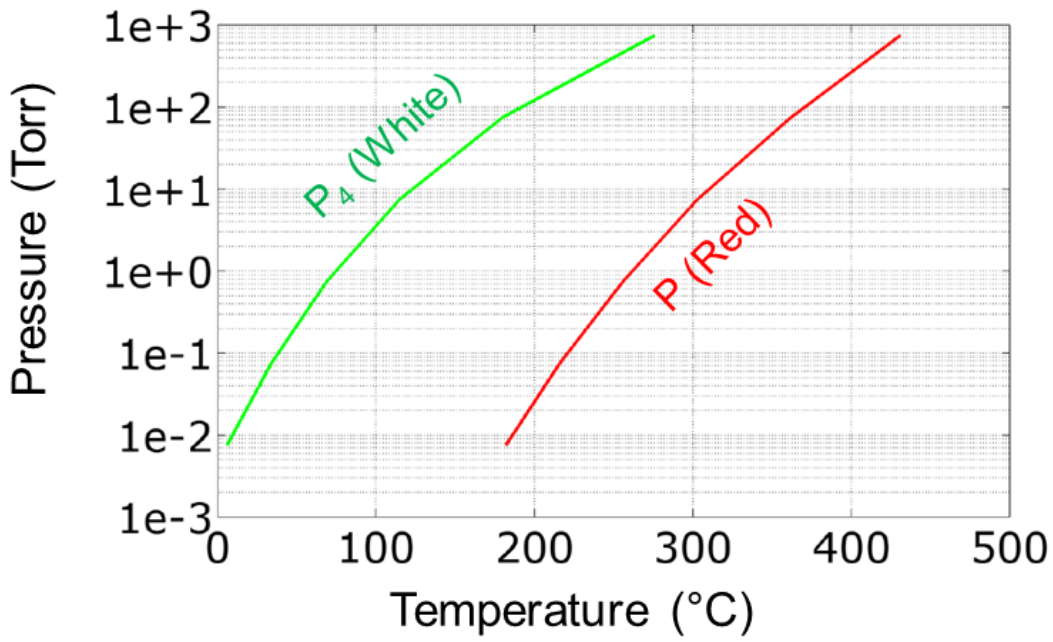

Figure 2.8: Phosphorus vapor pressure curves for two allotropes of phosphorus. The white phosphorus equilibrium is depicted in green whereas the r-P equilibrium curve is depicted in red.

Although As is certainly more stable than P, it was crucial to obtain comparable amounts of As and P on a single uniform film. Allowing the substrate to reach too high of a temperature would certainly result in desorption of the phosphorus from the substrate. Additionally, growth times beyond 2h also would have been detrimental to successful deposition.

One of the major tradeoffs of conducting MBE depositions cold is the lack of film reorganization during growth. For most deposition techniques including CVD, sputtering, and MBE, substrate heating is ubiquitous. This is because the thermal energy provided by substrate heating improves film morphology by providing the necessary driving force for diffusion. As adatoms impinge upon the surface, they diffuse (given sufficient thermal energy) which allows them to migrate to empty lattice sites. Additionally, any film defects and surface stresses that are created during growth can be annihilated given sufficient temperature conditions. Essentially,

providing thermal energy during growth allows films to reorganize, thereby reducing built-in defects. Overall, whenever sufficient thermal energy and time is provided, a system can and will minimize its total Gibbs free energy. Consequentially, by removing thermal heating, defects, vacancies, and the as-deposited microstructure is "frozen" in.

With the deposition restrictions imposed by the low vapor pressure of phosphorus, an alternative approach needed to be taken in order to improve the crystallinity of our films. The solution that was taken was to do a post-growth annealing process. Post-growth annealing processes are common among many different material depositions. Additionally, they can be used to restore structural order following outside perturbation. An example of such is ion implantation used to dope Si. Rapid thermal annealing is used to repair the crystal structure of Si, which is damaged during the high-energy implantation process. The low vapor pressure of P is also a problem for post-deposition annealing. If the annealing temperature is too hot, desorption from the film occurs. Thus the approach taken was to first encapsulate the film, then subsequently anneal. A full section discussing the annealing procedure is found in Chapter 3.

2.5 Delineating b-AsP MBE Growth Rate

A major roadblock in the MBE deposition of b-AsP was the surprising growth rate. The MBE system we used was the Varian Gen II. Our MBE is equipped to allow for single-wafer 3" capability and was previously used for III-V and II-VI material growth such as InP, InGaAs, and InAs. As stated above, our fluxes were on the order of 1E-8 Torr for As_2 and 1E-7 Torr for P_2. Typically, growth rates for the more traditional materials grown on all of our MBE systems using the same source fluxes are on the order of 1 μm per hour. This is alarming because our initial growth rate for our first b-AsP samples were three orders of magnitudes smaller, on the order of

5 nm per hour. We expected the growth rates of b-AsP to be comparable to those of the more traditional III-V materials, especially since the deposition was done cold. To explain the growth rate phenomena, we return to our discussion about substrate heating. The high-temperature cracking zone for the P and As cells are held at 950°C.

Assuming that the cracker acts as an ideal blackbody, the spectral emission can be described by Planck's law below:

$$B_\nu(\nu, T) = \frac{2h\nu^3}{c^2} \frac{1}{e^{\frac{h\nu}{k_B T}} - 1} \qquad (2.1)$$

This relationship gives the spectral radiance, $B_\nu(\nu, T)$ as a function of frequency, ν. The spectral radiance distribution differs for various temperatures. In particular, the peak radiance frequency (or wavelength) is a direct consequence of blackbody temperature. With increasing temperature, the radiance maximum is shifted to higher and higher frequencies. A plot of the Planck's law as a function of temperature is seen below. It's important to note that blackbodies do not radiate monochromatic light, but rather radiate a distribution of wavelengths. This plays an important role into substrate heating as electron excitation processes always generate thermal heat as a by-product. For our experiment, the emission wavelengths from the blackbody and the deposited material bandgap E_g plays an important role in considering substrate heating. To uncover this role, a closer inspection of the blackbody radiation spectra at 1223K (950 °C) must be considered.

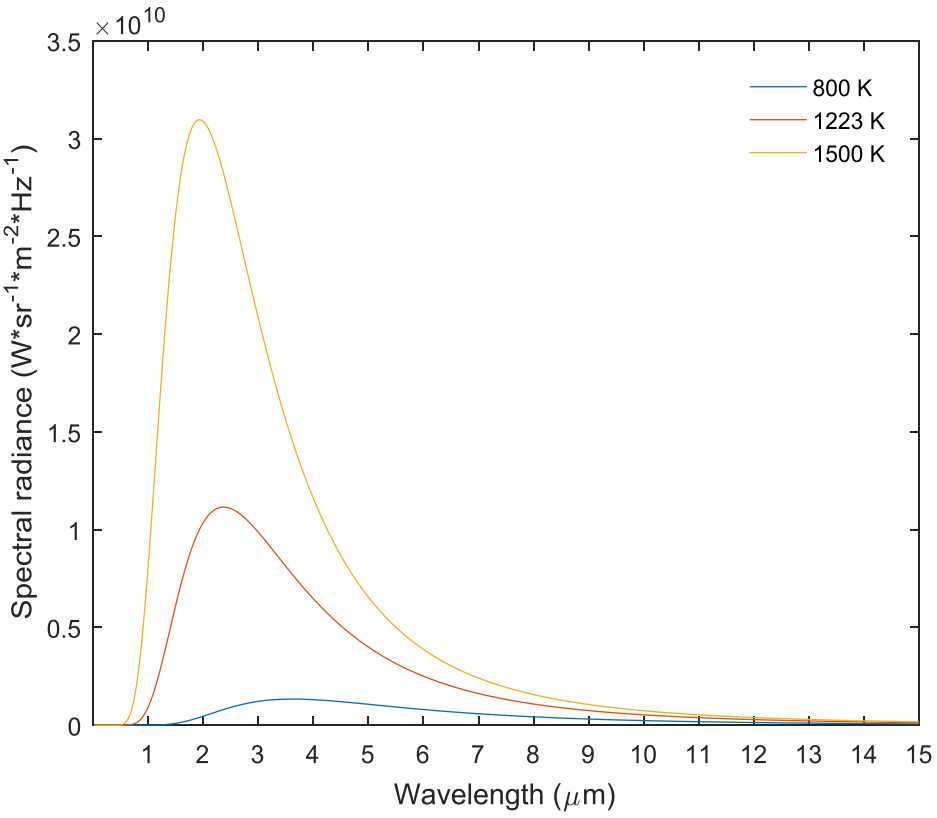

Figure 2.9: Planck's Law for blackbodies at various temperatures. The blue curve indicates the spectral distribution for a perfect blackbody at 800 K, the red curve is one at 1223 K and the dark yellow corresponds to one at 1500 K. As expected, the distribution max shifts to lower wavelengths (thus higher frequencies and energies) as temperature increases.

Figure 2.5 depicts the specific radiative emission spectra for a perfect blackbody at 1223 K. For the case of this model, we will assume that the sources from the crackers are perfect blackbodies, and that the UHV environment within the chamber is a perfect vacuum. Figure 30 is another depiction of the bandgap of b-AsP. As previously discussed, the bandgap is 0.3 eV for b-P and 0.15 eV for b-AsP. This means that significant amounts of the blackbody radiation emitted are absorbed by b-AsP during growth. A depiction of the bandgap for b-P is shown in Figure 31.

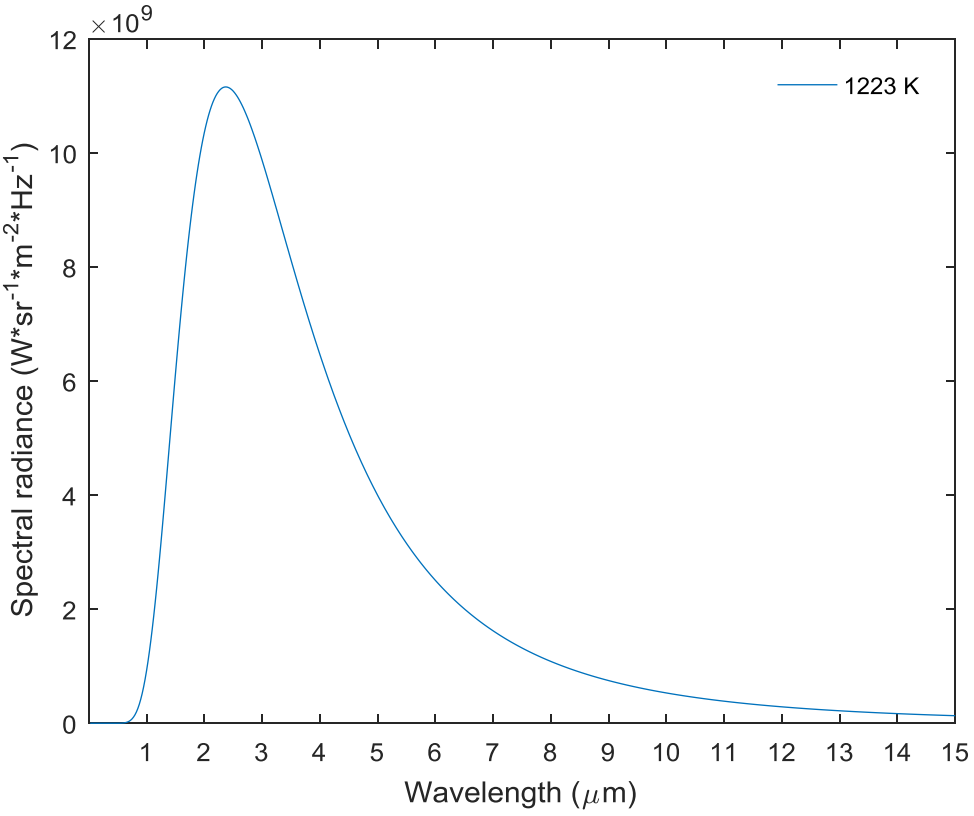

Figure 2.10: Planck's Law for a blackbody at 1223 K. This was the temperature of our phosphorus and arsenic cracker. The maximum is centered at 2.375 μm, or 0.52 eV.

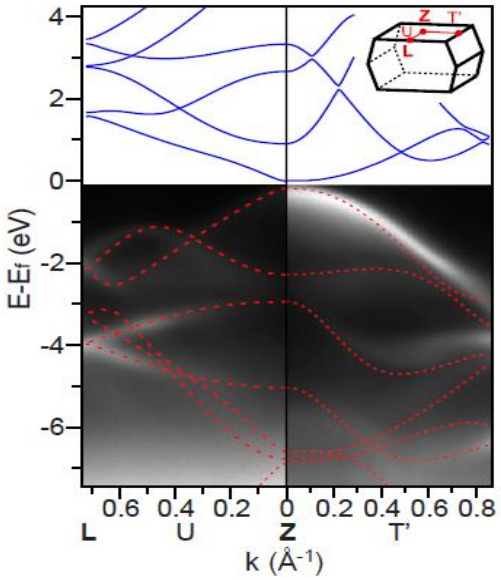

Figure 2.11: Angle resolved photoemission spectroscopy measurements for few layer b-P showing band-structure.

Earlier, we hypothesized that the growth of b-AsP was self-limiting. We did not believe the growth rate was uniform over 2 hours, since that would give the incredibly slow growth rate of ~5 nm/hour. Instead, it was our prediction that at a certain film thickness, the growth halted. From a materials perspective, the bandgap of b-P is known to be layer-dependent, as is that of b-AsP. This is due to quantum confinement; with increasing number of layers, more orbital states can overlap creating larger valence and conduction bands. Consequentially, the bandgap shrinks from a 2 eV in the monolayer to 0.3 eV in the bulk. The bulk value of 2 eV corresponds to 620 nm visible, red light whereas 0.3 eV is 4 μm light. According to Planck's law, there is no radiative emission given off at 620 nm from a perfect blackbody. Instead, the high-energy tail end of the Planck distribution begins somewhere around 1 μm. Thus, when deposition first begins, the b-AsP acts as a window and does not absorb any of the blackbody emission given off from the P and As sources.

However, as deposition proceeds, the number of layers changes, and as a result the material bandgap shrinks. As mentioned in Chapter 1, it is well known in 2D materials that beyond 3 layers, the material starts to exhibit bulk-like properties. For b-P 5 or more layers, the material can be assumed to essentially be bulk like. Black phosphorus has a layer thickness of approximately 5.3 Angstroms, or half a nm. This means that by 3-4 nm of deposited material, the b-P can more or less be assumed to take on bulk-like properties. In the bulk, the b-P absorbs a large portion of the emission from the sources. As a result, the film heats significantly, which limits continual deposition due to desorption. With this hypothesis and a model in mind, we moved to validate our results via experiment.

2.6 Mathematical Model for Substrate Heating during MBE

In order to better understand the self-limiting nature of our growth during MBE, a mathematical model was employed. In particular, the heat transfer effects of radiative heat transfer were examined. First, a comparison of the two materials and their corresponding growth rates was made. A classical material grown at Northrop Grumman Corporation is InP. InP has a direct bandgap of 1.34 eV and is typically observed to have a growth rate of 630 nm/hr. This is two orders of magnitude above the growth rate observed for our b-AsP films. As mentioned previously, it was hypothesized that the heating effects from the hot sources were causing significant temperature rise on the substrate. This in turn, would reduce the sticking coefficient of the P_2 atoms thereby causing re-evaporation of the film. Figure 2.7 presents a table in which the two materials are compared and contrasted with respect to bandgap and growth rate.

Material	E_g (eV)	E_g (μm)	Growth Rate
InP	1.34	0.92	~630 nm/hr
b-AsP	0.15-0.30	8.3-4.1	~4 nm/hr

Figure 2.12: Bandgap and Growth rate comparisons for InP and AsP. The bandgap of InP is 1.34 eV vs the varying bandgap for b-AsP of 0.15 eV to 0.3 eV.

Equation 2.1 listed above provides Planck's distribution as a function of both frequency and temperature. The Planck distribution peak max shifts with varying temperature. The fraction of absorption, $F_{\lambda_1-\lambda_2}$ given in equation 2.3, is the fraction of blackbody spectrum that a blackbody emits between two specific wavelengths. The value is particularly useful when only a

certain region of the blackbody emission spectrum is examined. This is particularly useful when looking at b-AsP, since the bandgap changes as a function of As concentration.

$$F_{\lambda_1-\lambda_2} = \frac{\int_{\lambda_1}^{\lambda_2} E_{b\lambda} d\lambda}{\int_0^{\infty} E_{b\lambda} d\lambda} \quad (2.3)$$

For pure b-P, the bandgap is 0.30 eV, whereas for b-$As_{0.83}P_{0.17}$, the bandgap is 0.15 eV. 0.3 eV converts to 4.1 μm, while 0.15 eV is equivalent to 8.3 μm. This means that for a blackbody emitter at 950 C, a 0.3 eV bandgap material absorbs 0.6209 of the emission spectrum, while a 0.15 eV material absorbs 0.9099 of the absorption spectrum as seen in Figure 2.8.

$$F_{0-4\mu m} = 0.6209$$
$$F_{0-8\mu m} = 0.9099$$

Figure 2.13: Fraction of emission for blackbodies held at 950°C between two emissive windows of: 0-4 μm and 0-8 μm. The fractions of spectral emission between 0-4 μm and 0-8 μm are 0.6209 and 0.9099 respectively.

In order to build a mathematical model to understand radiative substrate heating during MBE, radiation heat transfer must be understood along with some definitions. A blackbody is a perfect absorber and emitter and possesses the following properties:

Blackbodies:

- Blackbodies absorb all incident radiation, regardless of λ and direction
- For a given T and λ, no surface can emit more than a blackbody
- Blackbodies are diffuse emitters (directionally independent)

The first assumption is that blackbodies absorb all incident radiation. What electromagnetic radiation comes into contact with a surface, three physical processes can occur. Either the emission is absorbed, reflected or transmitted. The total fractional sum of these three processes must equal unity. The symbols typically used for each of these phenomena can be summarized in equation 2.4.

$$\rho + \alpha + \tau = 1 \ (2.4)$$

Regardless of wavelength and incident angle, all radiation is absorbed by a perfect blackbody. Additionally, the second assumption states that blackbodies are perfect emitters. Typically, a real substance will not emit the full spectral power predicted by Plank's law due to internal thermodynamic losses. This difference can be quantified by a material constant known as the emissivity. The emissivity of a material is the total spectral emissivity at a given temperature for the material divided by the ideal spectral emissivity of a blackbody at the ssame temperature temperature. The equation is displayed below.

$$\epsilon = \frac{E(T)}{E_b(T)} \qquad (2.5)$$

Naturally, the emissivity is a fractional constant, and thus ranges in value between 0 and 1.

The final assumption is that blackbodies are diffuse emitters, i.e. the emission is directionally independent. A blackbody emits according to the experimentally observed relationship known as the Stefan-Boltzmann law given below:

$$E = \epsilon\sigma T^4 \ (2.6)$$

This states that the total power equals a universal constant multiplied by temperature to the fourth power. The Stefan-Boltzmann law can be applied to real materials by simply multiplying by the emissivity.

$$E_b = \epsilon\sigma T^4 \ (2.7)$$

Given the fundamental physical equations needed to describe radiation heat transfer, we now move to real application of these equations. Geometrically speaking, the view factor is of utmost importance when dealing with radiation heat exchange. The view factor essentially

describes the projection of one surface onto another based simply on geometrical line of sight. Take for instance two parallel discs that are identical in size. If the disks are placed facing each other on the same central axis, the view factor is equal to unity. However, the same cannot be said if the discs are off axis, non-parallel, or rotated. A geometrical representation of the view factor can be seen in Figure 2.9 below.

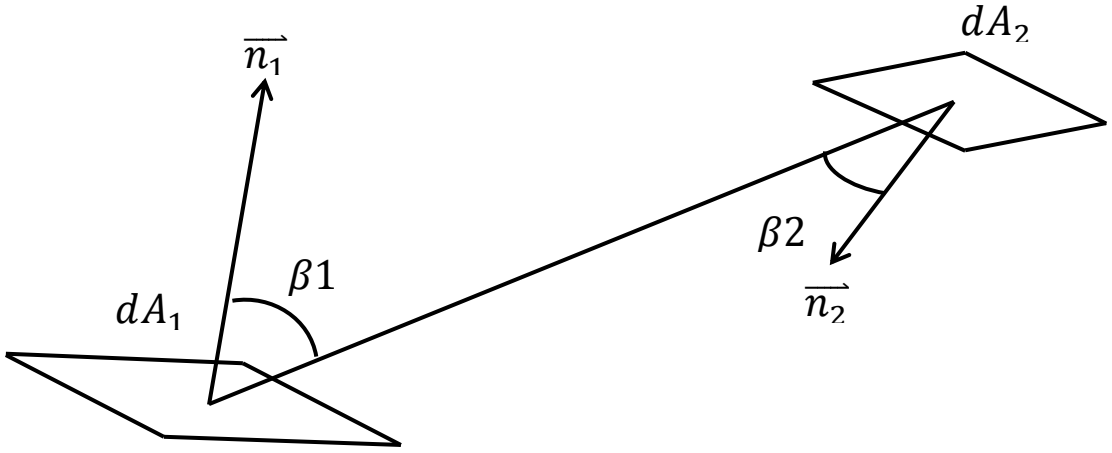

Figure 2.14: Geometric representation of the view factor. Two differential planes are used, dA_1 and dA_2. A center to center line is drawn and the angle between the normal vector and this line defines the angles between the two planes.

The view factor can be mathematically calculated from Equation 2.8 below (8):

$$F_{12} = \frac{1}{dA_1} \iint \frac{\cos\theta_1 \cos\theta_2 \, dA_2 dA_1}{\pi r^2} \quad (2.8)$$

This essentially states that the view factor between surface 1 and 2 is equal to a double integral which sums the differential areas that are capable of being projected onto each other. The view factor has a value between 0 and 1. The view factors of two surfaces are related by the reciprocity relationship given in Equation 2.9 below.

$$A_i F_{ij} = A_j F_{ji} \quad (2.9)$$

Additionally, the sum of all view factors of a surface with all other surfaces much equal one, as given in Equation 2.10 below.

$$\sum_{j=1}^{N} F_{ij} = 1 \quad (2.10)$$

Given these equations which describe radiative heat transfer, we now have the adequate fundamental equations to begin building a heat transfer model. A detailed schematic of the geometries can be seen in Figure 2.10 given below. Here a simplified drawing of an MBE chamber is given, along with all relative heat transfer surfaces. The surfaces of importance are the two P and As sources, the substrate, the substrate holder wall, and the surrounding MBE chamber. Some important values must be named in order to better understand the physical system. The temperature of the crackers is 950°C, while the area is 25 mm. The area of a 3" substrate, in SI units is ~38 mm and the volume is approximately 2.74E-6 m^3. The density of the substrate, which we assign as InP is 4.81E3 kg/m^3, while the heat capacity is 0.31E3 $J*kg^{-1}*K^{-1}$. The temperature of the surrounding cryo-shroud is assumed to be the temperature of liquid nitrogen and is assigned 77 K. The incident angle of emission is assigned to be 30°.

Three important view factors need to be used. The first two are the view factors between the sources and the substrate, which are equal and have a value of 0.0044. The last view factor is between the substrate and the surrounding wall, which is equal to 1- 2*(0.0044). For all intensive purposes the value of F_{1surr} is approximated to equal 1. The substrate holder and the wall are both assigned to be stainless steel, with conduction path length equaling 76 mm, cross sectional area of conduction equaling 0.00961 m^2, and thermal conductivity of steel k_{steel} equaling 16.3 $W*m^{-2}*K^{-1}$.

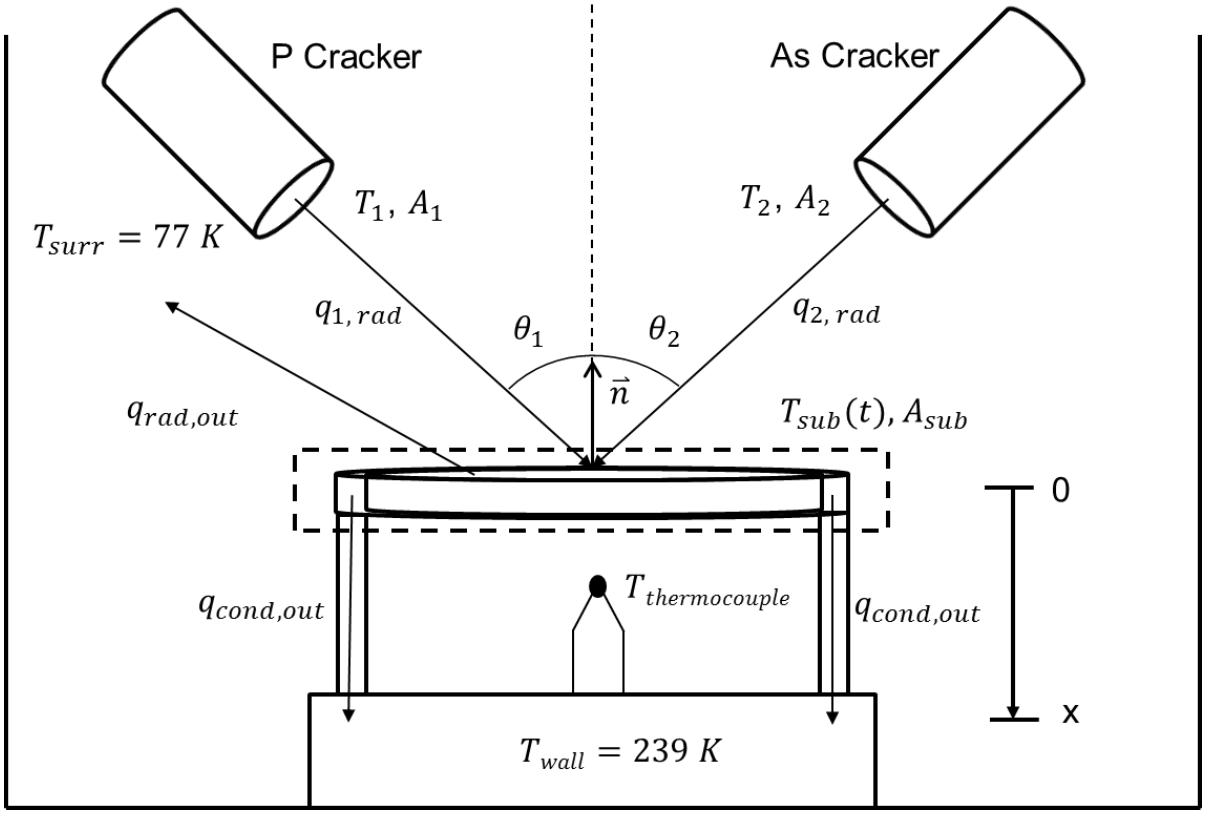

Figure 2.15: Physical system with all relevant surfaces and heat transfer mechanisms described during MBE heating of an InP substrate.

An energy balance taken over a control volume of the substrate gives Equation 2.11 below:

$$\rho v c_p \frac{dT}{dt} = q_{1,rad} + q_{2,rad} - q_{rad,\ out} - q_{\ cond.,\ out} \quad (2.10)$$

The left hand side of the equation represents the total accumulation of heat during the process. The right hand represents the total heat in and out of the control volume. Two heat values enter the control volume, namely the two radiative heating from the sources. The substrate loses heat via two mechanisms, emission from the substrate to the surrounding wall, as well as conduction heat loss out the substrate through the stainless steel substrate holder.

With the governing heat transfer equation set up, we need to make some assumptions in order to simplify the mathematics which are given below.

Assumptions:

- All surfaces behave as blackbodies (i.e. blackbody emission and total absorption)
- Substrate is isothermal at a specific time
- 1-D conduction
- T_{wall} goes as experimentally measured thermocouple temperature

The fourth assumption is of particular importance, and essentially states that the temperature of the wall is not constant with respect to time, and rather changes as the thermocouple temperature. The thermocouple resides protrudes from the wall and resides at the back of the substrate, though no physical contact is made. Thus the thermocouple is by no means the actual temperature of the substrate. We can now fully express the mathematics of our energy balance specifically seen in Equation 2.12 below:

Energy Balance over Control Volume:

$$Accumulation = In - Out + Gen. \quad (2.11)$$

$$\rho v c_p \frac{dT}{dt} = A_1 F_{1sub} \sigma ({T_1}^4 - {T_{sub}}^4) + A_2 F_{2sub} \sigma ({T_2}^4 - {T_{sub}}^4)$$
$$-A_{sub} F_{subsurr} \sigma ({T_{sub}}^4 - {T_{surr}}^4) - \frac{kA}{L}(T_{sub} - T_{wall}) \quad (2.12)$$

This differential equation can be solved iteratively using the Euler method. Essentially, the differential is replaced by a series of discretized step size and solved successively for different values of the independent variable. Euler's method is given by Equation 2.13 below.

Solve Iteratively (Euler Method):

$$y'(t_0) \approx \frac{y(t_0+h)-y(t_0)}{h} \quad (2.13)$$

where h is the step size

Matlab was used to generate the numerical model. The code can be found in Appendix I. First, we examine the maximum radiative heating by ignoring the heat loss terms. The result is the temperature profile given in Figure 2.11 below. We see a linear temperature profile with heating rate of approximately 0.727°/s. This is essentially the temperature profile given the substrate is heated only by the blackbody sources.

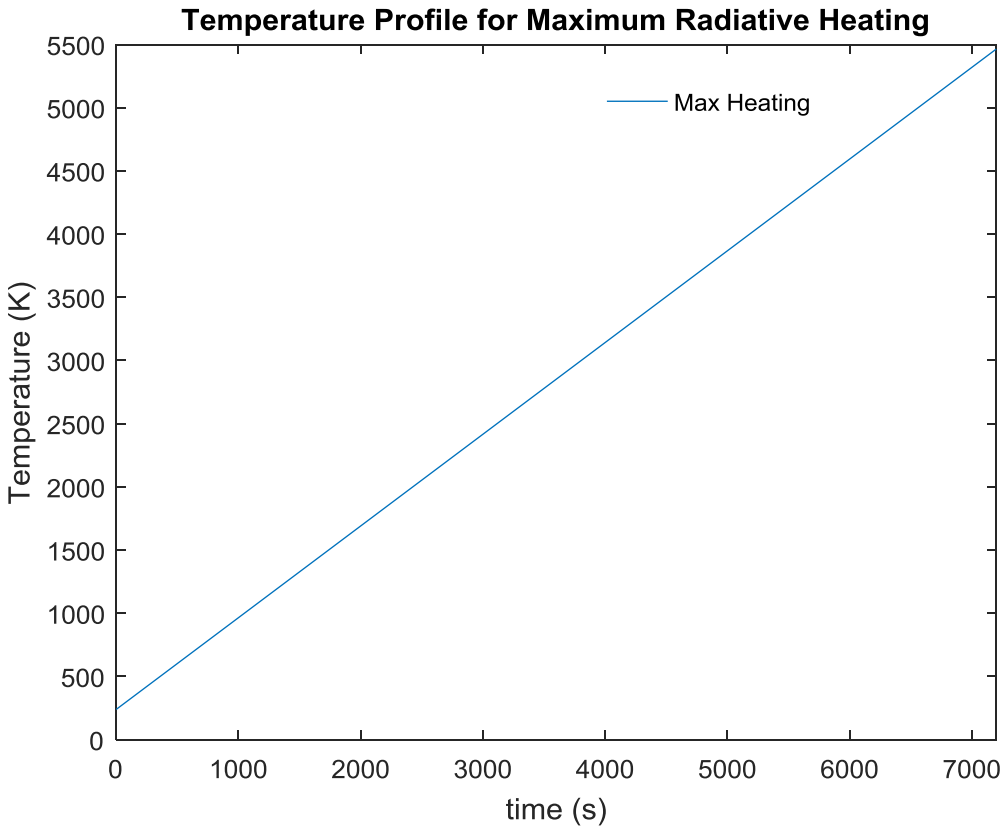

Figure 2.16: Temperature profile for maximum heating condition.

Next, the temperature profile the maximum cooling condition was examined. This again, was taken by ignoring the heating terms in the differential equation and solving for the temperature profile. The results are given in Figure 2.12.

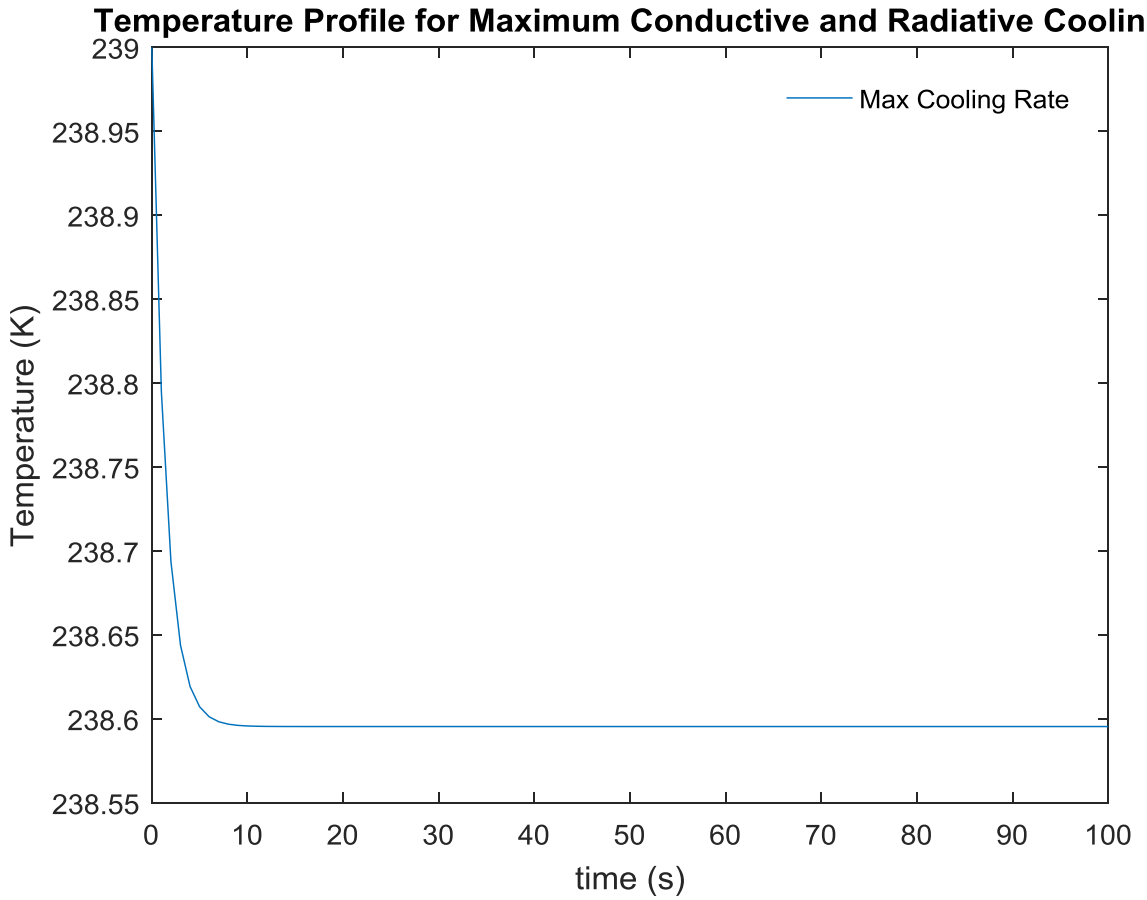

Figure 2.17: Temperature Profile for Maximum Cooling

For maximum cooling conditions, we see an abrupt drop within 5 seconds in temperature about half a degree to 238.6 K. The temperature then stabilizes at this temperature for all times. An effective model should lie between the maximum and minimum conditions to be viable. Solving the total differential equation gives the temperature profile seen in Figure 2.13. As visualized, the temperature makes a polynomial-like rise to approximately ~34°C in about 30 min, then saturates and holds at this temperature for long times. Figure 2.14 shows that our model is indeed bounded by the upper and lower limits described in the figures above.

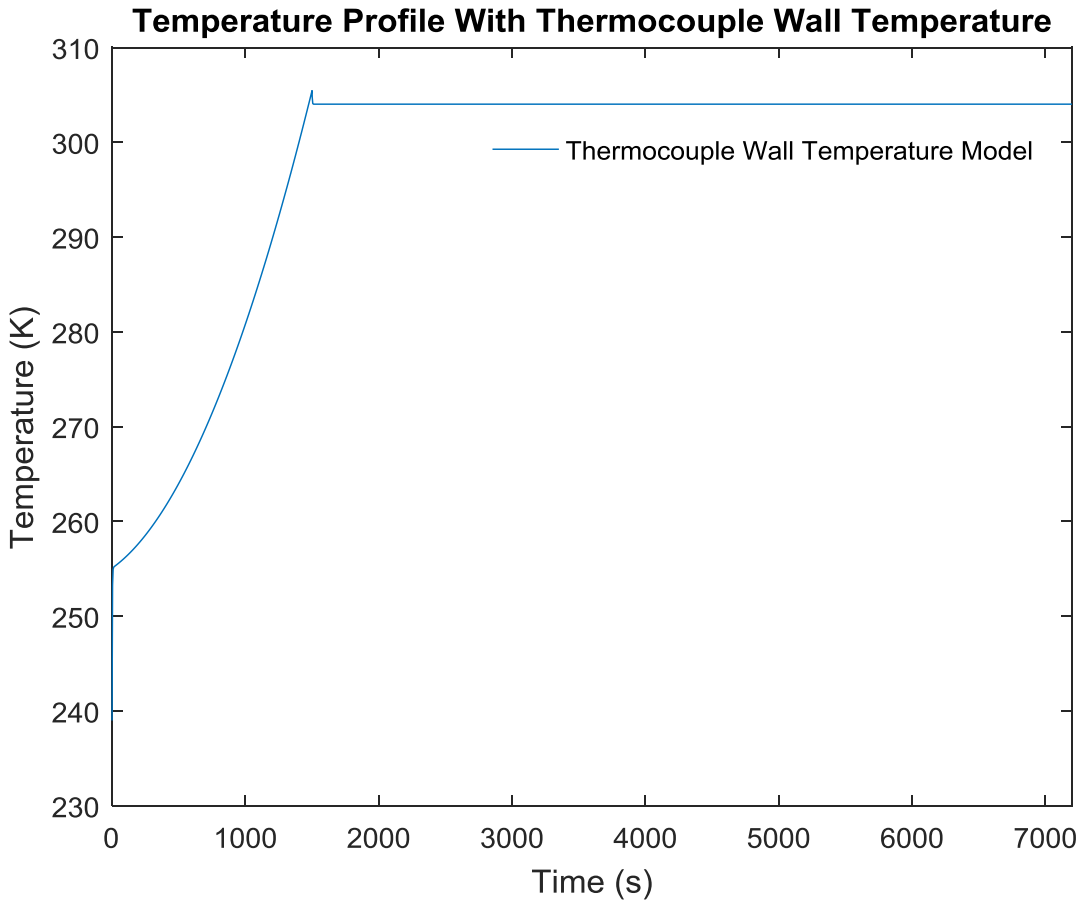

Figure 2.18: Total differential equation solved for radiative heating due to MBE.

Although many critical assumptions had to be made in order to construct this model, the results help enlighten as to what is physically going on to the substrate temperature. As growth proceeds, the substrate indeed heats up as expected, despite the lack of substrate heating. Although the rate at which it heats may be inaccurately predicted by the model, the model affirms the hypothesis that the radiative heating effects dominate the cooling effects, thus resulting in temperature rise during growth. This allowed for us to make experimental adjustments given the model and experimental results that show that the substrate heats during deposition. Because of the high vapor pressure of phosphorus, and in particular P_2, the heating effects experienced by the substrate can be reasonably be assumed to result in re-evaporation of

P_2 during deposition. The critical assumption that the wall temperature goes as the thermocouple is perhaps the largest leap from physical reality. It is possible that the temperature saturates at a hotter temperature than the 34°C as predicted by the model. In either case, the 34°C predicted by the model still results in significant vapor pressure as seen by Figure 2.15. Additionally, because deposition occurs in UHV, the driving force for re-evaporation is even larger, as predicted by Le Chatelier's principle. Using our model, we can thus make experimental adjustments in order to grow thicker films, which will be discussed in later sections.

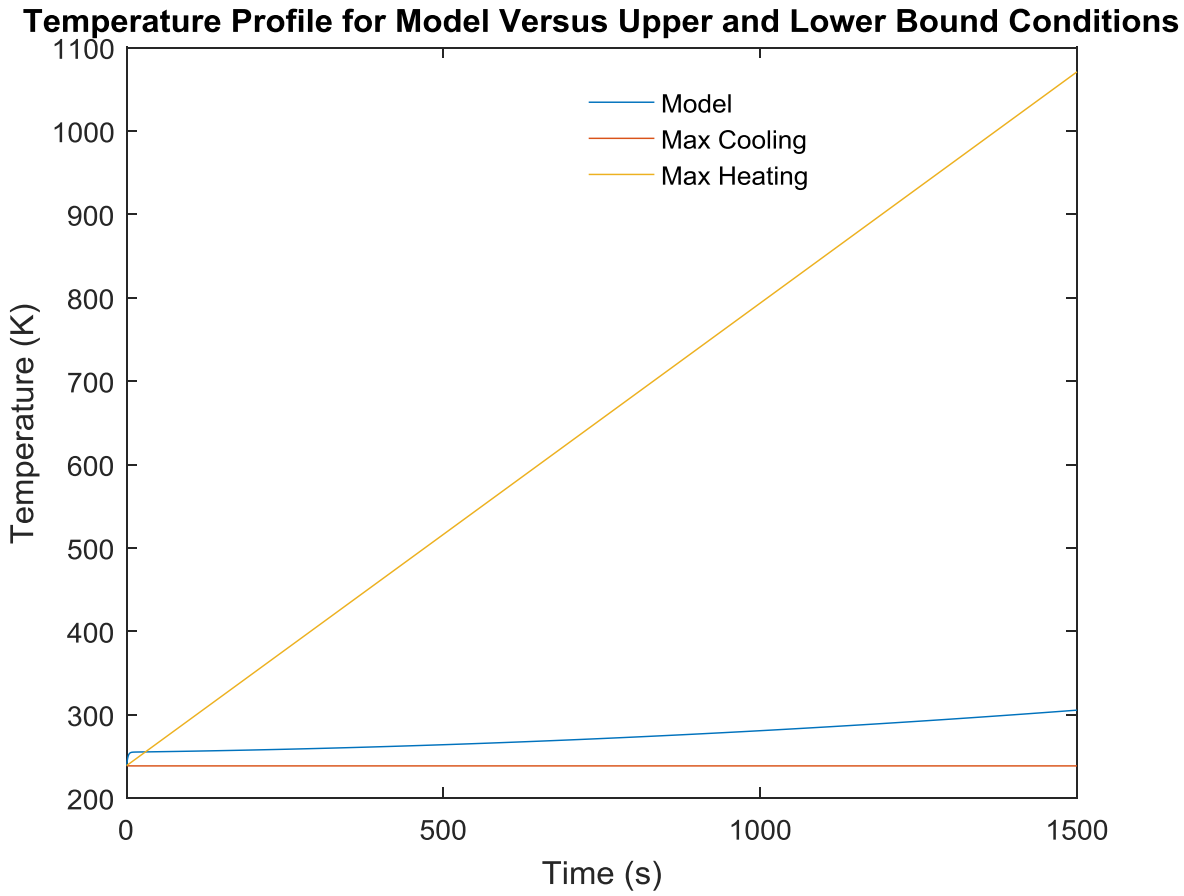

Figure 2.19: Max cooling, max heating and total model results plotted on the same graph. The model resides within the upper and lower bounds, as expected.

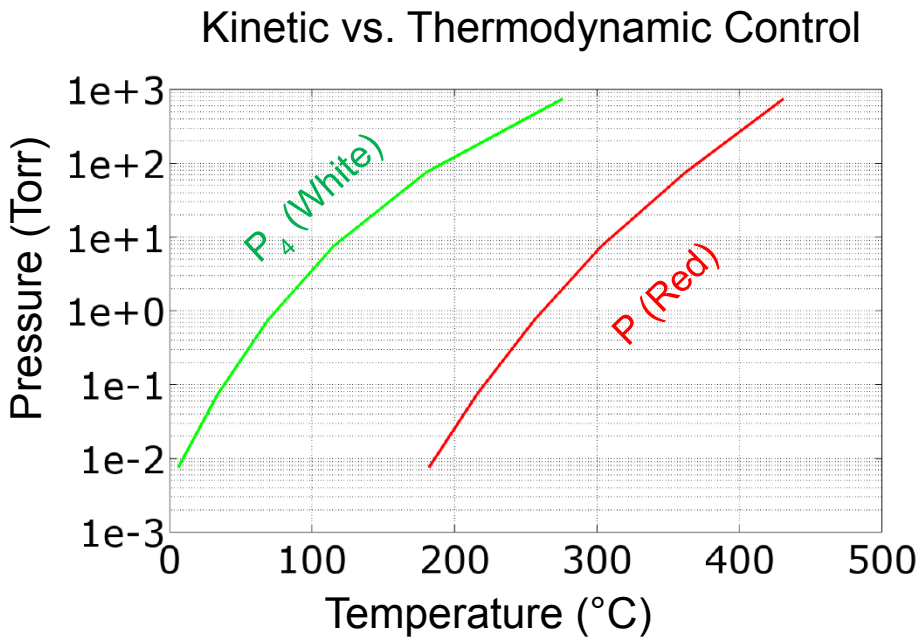

Figure 2.20: Vapor pressures of phosphorus as a function of temperature

2.7 Depositions of Pure Phosphorus

Depositions of pure phosphorus were also attempted, though the primary focus of this thesis is on b-AsP. b-AsP was chosen because initially, our group's efforts towards depositing pure phosphorus via MBE was unsuccessful. However, when growth was conducted with the aid of Pt and Pd catalyst, our group was previously able to deposit amorphous P and AsP. A schematic of the process can be seen in Figure 2.12 below.

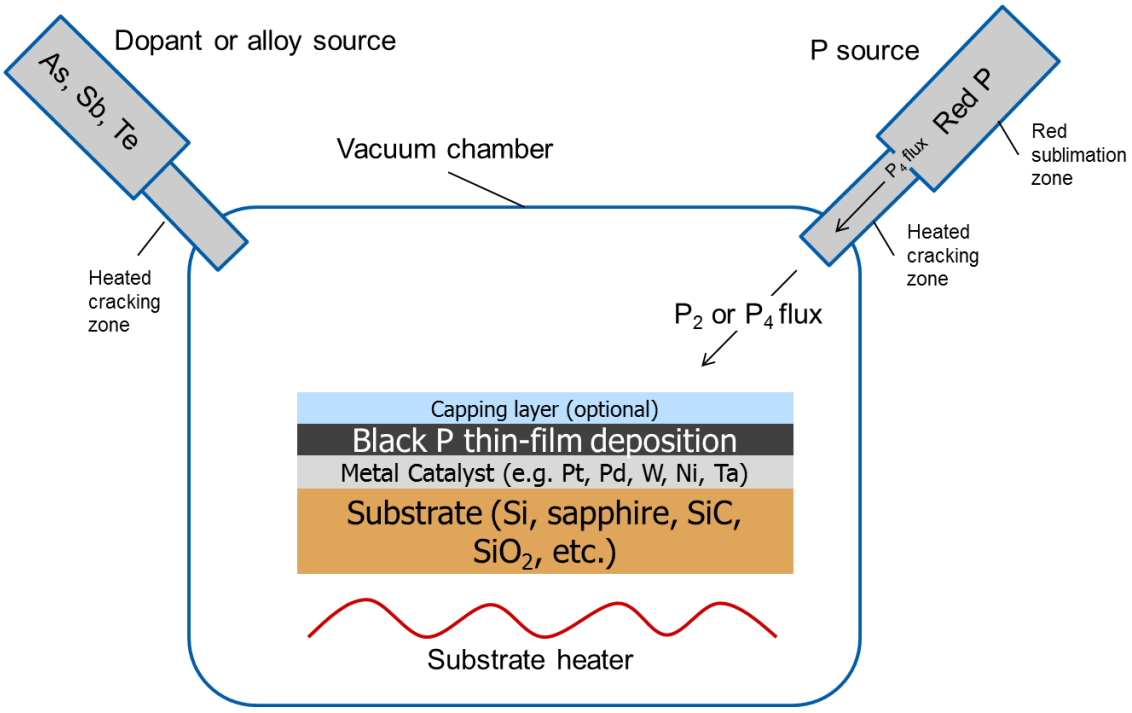

Figure 2.21: Catalytic MBE schematic with phosphorus and As/Sb/Te sources. Both of the solid sources are equipped with a high temperature cracker, which can be used to dimerize P_4 and As_4.

The catalytic growths were conducted in the presence of substrate heating as compared to cold. Typical deposition temperatures ranged from 200-300 °C, with growth times of 60 minutes, and P flux of 7.1E-7 Torr. Typically, an adhesion layer was deposited in order to prevent delamination of the metal catalyst from the substrate surface. Several different metal catalysts were attempted, including Pt, Ti, and Ta.

Preliminary samples were characterized by Raman spectroscopy to investigate the successfulness of our technique. A more detailed treatment on Raman will be given in Chapter 3, though for the sake of discussion, some results will be presented here. The results of our initial Raman can be visualized in Figure 32.

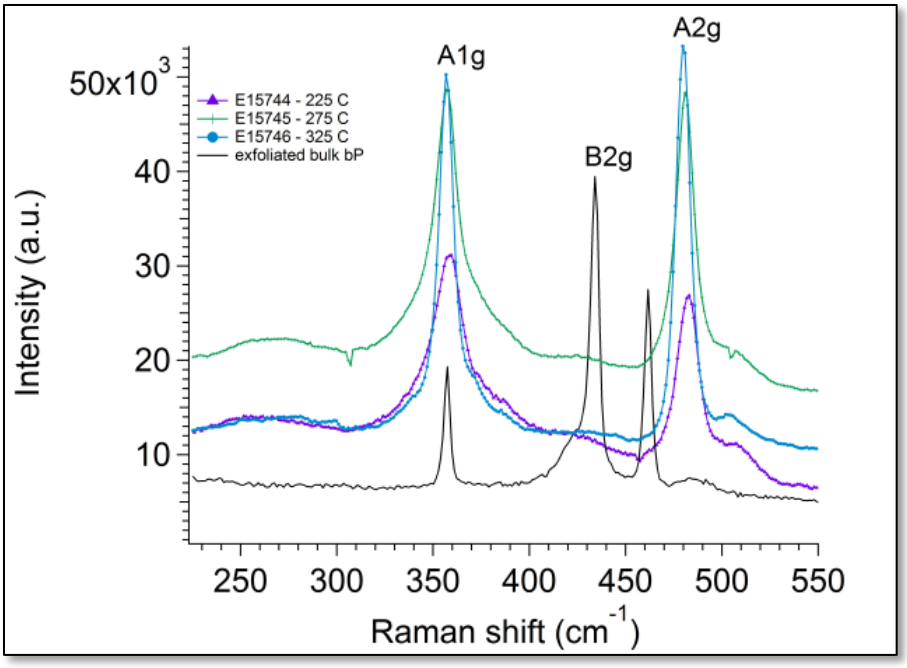

Figure 2.22: Raman Spectra for b-P grown via catalytic MBE. The catalyst used was Pt. The black line indicates the exfoliated bulk b-P spectra, whereas the colored lines all indicate MBE of b-P at different processing temperatures.

A clear discrepancy is seen between the spectra of bulk b-P as compared to catalytically grown b-P. Most importantly the B_2^g mode, centered at 430 cm^{-1} is absent for all as grown films. A few speculative reasons for the suppressed peak include substrate interference, the presence of catalyst, and the overall poor morphology of the film. Unlike bulk b-P, the synthesized thin films are substrate bound, which for such thin active regions can prohibit certain Raman active modes. For instance, if the B_2^g mode is a vibrational mode in the direction orthogonal to the substrate, the bounded nature of the substrate/film interface may interfere with the B_2^g vibrations. The presence of catalyst may also disrupt certain bond-dependent modes. For instance, B_2^g is undoubtedly a P-P mode, thus if significant amounts of Pt is present, a P-Pt mode may dominate as compared to a P-P mode. Finally, the B_2^g Raman mode may be absent because of the overall film morphology. The lack of structural order within the film can greatly modify the vibrational

modes. Since vibrational modes are essentially the sum of constructive interferences of individual bond vibrations, the absence of a well-defined crystal structure will certainly alter the crystal Raman modes. Indeed, amorphous materials often show different Raman spectra as compared to their crystalline counterparts, as seen in the well-studied Si system as well as the amorphous b-P transistor seen above.

We characterized one of our films using a variety of electron microscopy techniques. The film stack examined was consisted of a 5 nm Al_2O_3 ALD cap, the deposited phosphorus film (unknown thickness), 100 nm of Pt catalyst, 10 nm Ti adhesion layer, and the Al_2O_3 substrate. Cross-sectional TEM images show an extremely rough interface between the substrate and the deposition layers along with a large film region containing an indistinguishable mix of the Pt catalyst, phosphorus, and Al_2O_3 layers. Because the depositions were done at elevated temperatures, the intermixed regions are attributed to the diffusion of activated species. An image of the cross-section of the film can be seen in Figure 2.14 below. The compromised growth layers are a large concern and were one sign that our metal-catalyzed process was not successful. A zoom-in image can be seen in Figure 2.15.

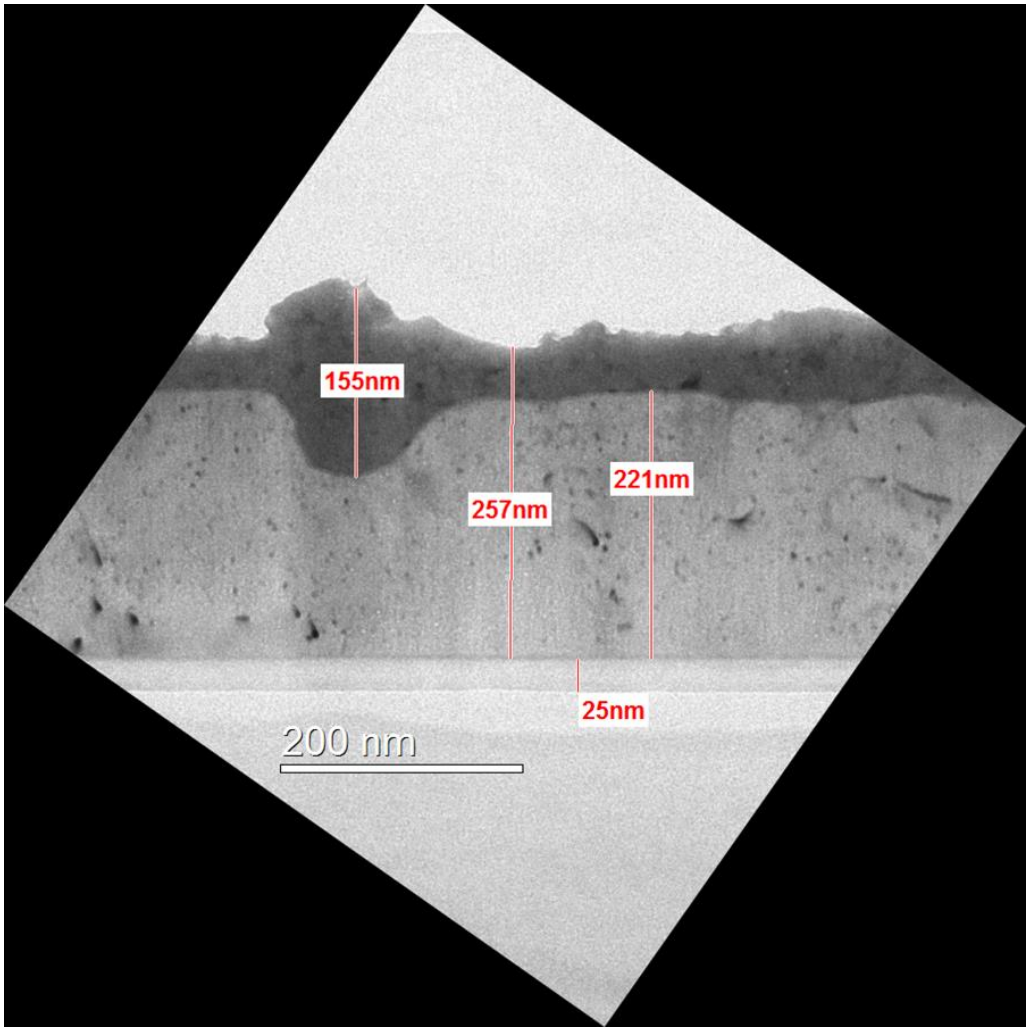

Figure 2.23: Cross-sectional low resolution TEM image of metal-catalyzed phosphorus growth. The bottom 25 nm is the Pt protection layer which is e-beam deposited during the FIB process. Situated above the Pt is the substrate, and above that the intermixed deposition layers.

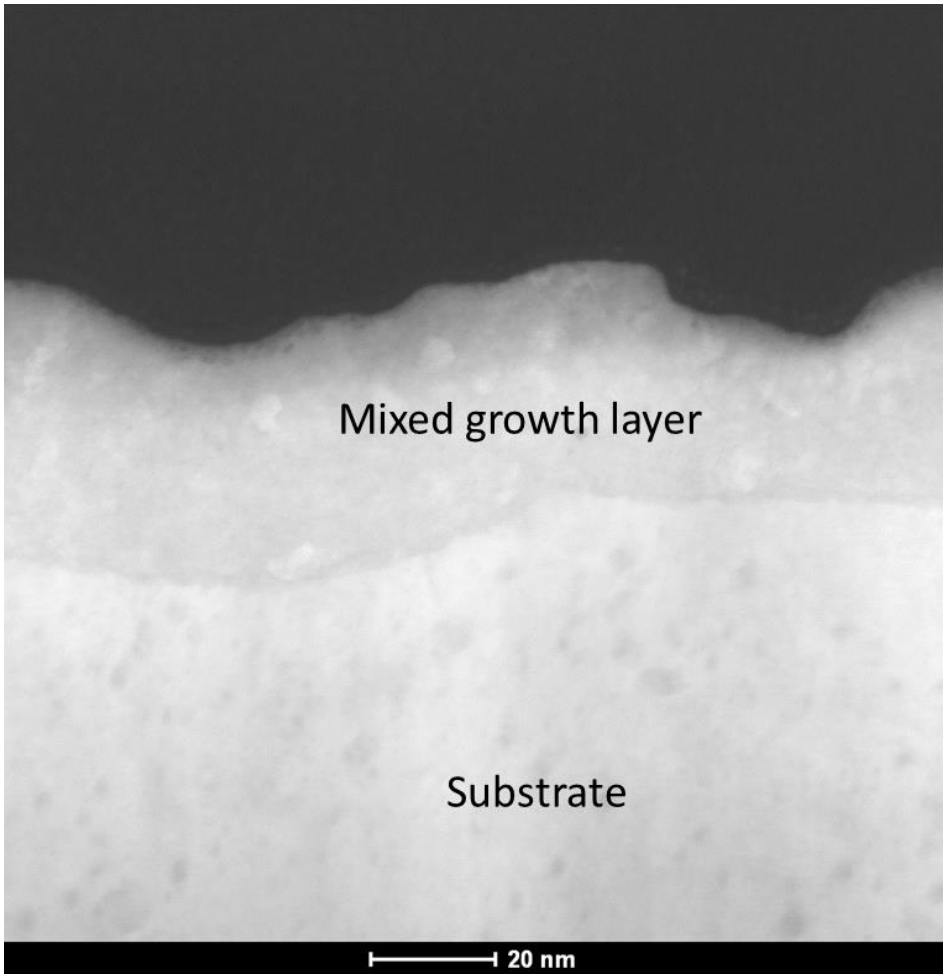

Figure 2.24: Cross-section of film-substrate interface via low-resolution TEM. As depicted, the 100 nm Pt and the phosphorus and cap layer and indistinguishable.

We further characterized our films using in-situ EDS. We mapped the interface of the substrate and the perceived film layer to obtain compositional information. Figure 2.16, below, shows our results. As expected, the results indicate a completely inter-diffused heterogeneous deposition layer. Additionally, substantial Al diffusion from the substrate was seen as well. The mixing of these elements essentially rendered the phosphorus film useless for further metrology and/or device fabrication. Significant Pt was detected in the phosphorus layer, which undoubtedly changes the chemical nature of the phosphorus. An amorphous mixture of all expected elements instead is seen, which points to the inadequacy of this process. Thus, the

combination of both the substrate heating during growth as well as the presence of 100 nm of metal catalyst proved to be unsuccessful for depositing pure phosphorus on-wafer via MBE.

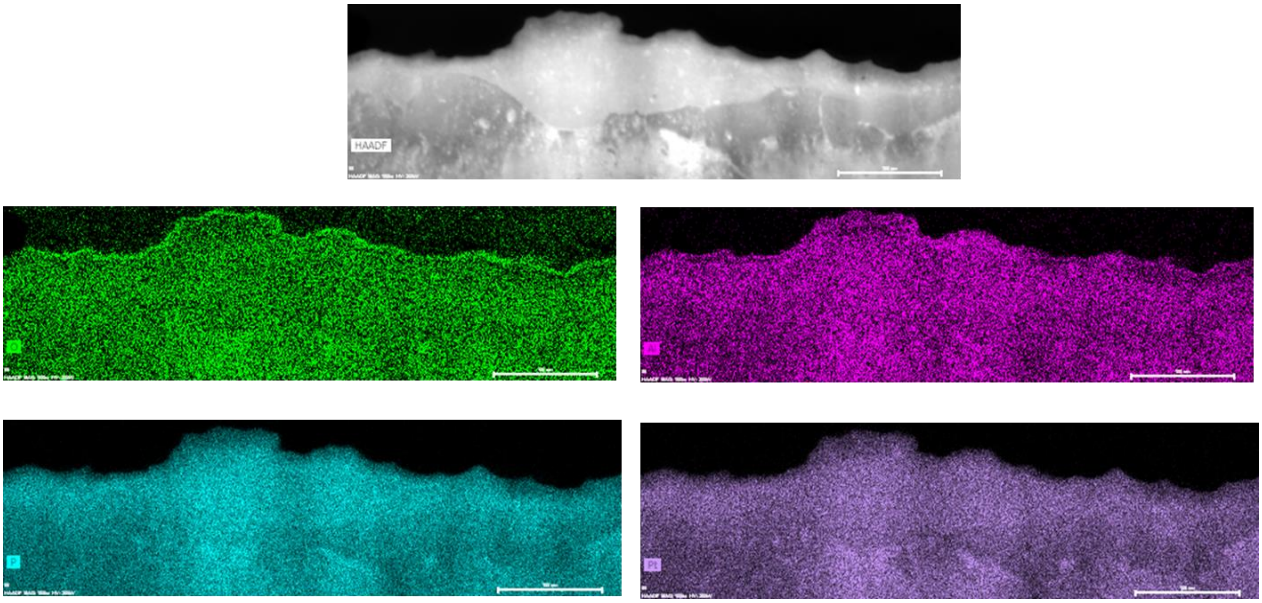

Figure 2.25: Cross-sectional EDS map for O (green), Al (purple), P (teal), Pt (pink). Pt is seen throughout the entire interface as well as Al. This seems to indicate significant intermixing of the elements during growth.

In lieu of these discrepancies in Raman signal along with our negative TEM and EDS results, we concluded that our catalytic MBE approach needed some serious modification. Growing pure b-P (as compared to b-AsP) on wafer was and still is highly desirable. While b-AsP boasts a narrower bandgap, pure b-P exhibits hole mobilities on the order of 1000 $cm^2V^{-1}s^{-1}$. The on-substrate approach is also a helpful tool in order to create various 2D semiconductor heterojunctions that may potentially have a variety of applications.

One of the primary problems with why phosphorus deposition in the absence of catalysts was unsuccessful is because of the low vapor pressure of phosphorus. For pure phosphorus depositions, the adsorption of the elements is much more sensitive to temperature. This is due to the discrepancy of sticking coefficients between phosphorus and arsenic. Arsenic is well known

to have a very high sticking coefficient, and can adsorb to many substrates even at cryogenic temperatures. Typically, in our lab, we see As sticking to all surfaces including viewing ports. Phosphorus, on the other hand, is well known to suffer from a low sticking coefficient. The sticking coefficient is a well-known constant that is a strong function of temperature. As a result, my hypothesis was to deposit phosphorus as cold as possible. Previously, I described the methodology of improving growth rate of b-AsP. The same method was applied to depositions of pure P, with promising results. While the film –thickness was still much thinner than those of b-AsP, successful deposition of pure P on-wafer was confirmed. The discrepancy in growth rate is attributed to the difference in sticking coefficient as discussed above.

Characterization of phosphorus films was performed to confirm successful growth. Films were first observed under scanning electron microscopy (SEM). SEM images can be found in the figure below.

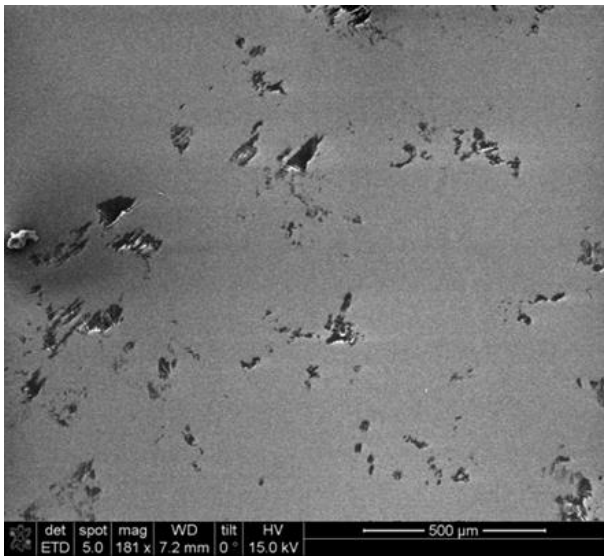

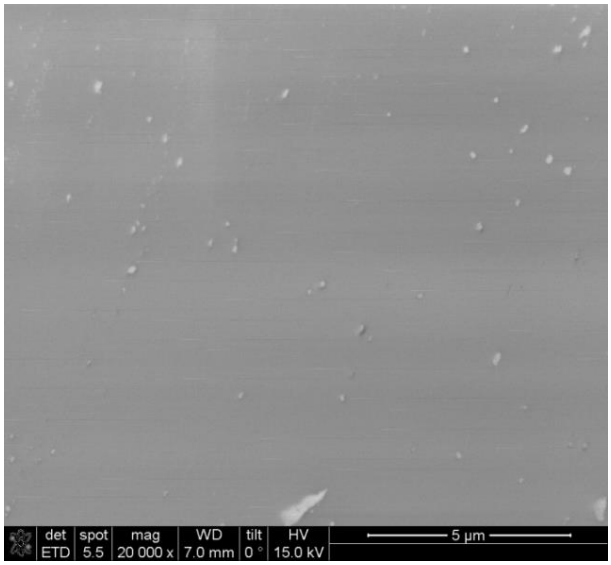

Figure 2.26**:** SEM images of phosphorus thin film deposited on sapphire. No structural morphology was visualized.

SEM imaging yielded little useful information. The thin films were characterized by XRR, and the thickness was found to be 9 nm. Because the SEM images were acquired prior to recrystallization, the expected morphology was an amorphous r-P film. This is because in the absence of high pressure or high temperature, the crystalline b-P solid phase would not have the sufficient thermodynamic conditions (P, T) to form. As a result, neither polycrystalline nor single crystalline structure was expected. SEM images validated this fact, as typically, grains that are on the order of microns can be observed. Additioanlly, the film thickness is so thin and relatively smooth that imaging of the surface would be ineffective via SEM. For most 2D materials, both monolayer and few-layer samples require TEM imaging as compared to SEM. This is because the resolution limits of SEM are inadequate to image small variations in film topology for thin and smooth films. As a result, no morphology of significance was detected via SEM.

The real impetus of getting our samples into an SEM was to obtain compositional information via EDS. By taking advantage of the electron gun afforded by the SEM, other

characterization techniques can be performed including EDS and electron backscatter diffraction (EBSD). For the purpose of validation, we wanted to confirm phosphorus presence by picking up a phosphorus peak via EDS. To do this, we collected data at the growth ring of our 3" wafer. At the growth ring, an interface occurs where there is deposited material and bare substrate. This is a consequence of the loading process for MBE, where the wafer holder essentialy shields a thin ~2 mm ring around the outside of the substrate. As a result, the region that is in contact with the stainless steel substrate holder is not exposed to the beam path(s) in MBE. While diffusion of species into the growth ring can occur (especially at hotter growth temperatures), the ring is for the most part, pure substrate. This allows us to do some convenient comparisons in EDS signatures at this region. Our EDS results can be summarized in the figures below.

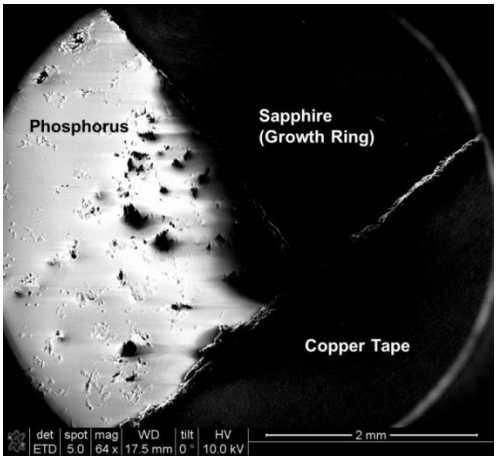

Figure 2.27: SEM image of growth ring. Three regions are noted. The phosphorus deposition region, the sapphire growth ring, and the copper tape. The copper tape was utilized to ensure good connection with ground, in order to avoid charging during sample exposure to the electron gun.

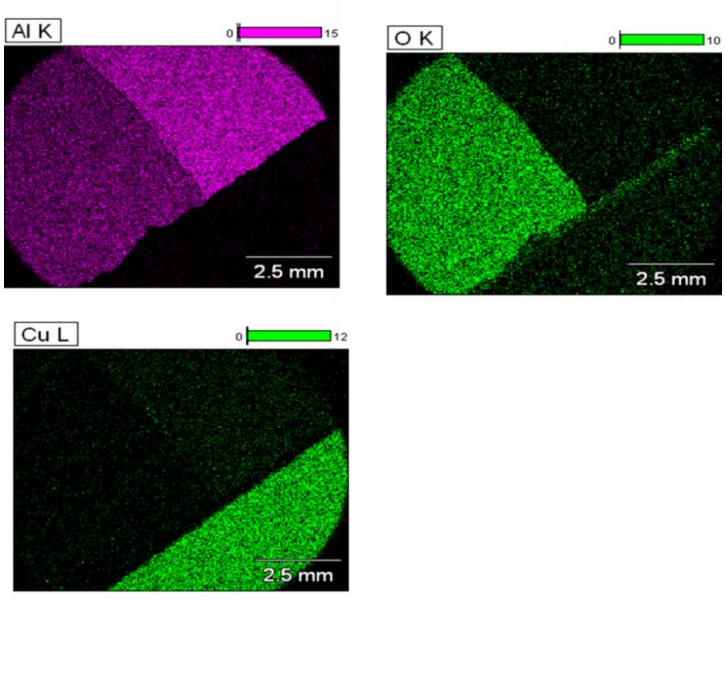

Figure 2.28: EDS composition map for Al, O, and Cu. The observed signals are in line with what was expected.

EDS depth resolution is a direct consequence of accelerating voltage. Resources discussing EDS in depth are abundant in the literature, thus an in-depth discussion will not be discussed in this thesis. The phosphorus scan from the EDS showed negligible signal in the topography map. However, the Al, O, and Cu all showed strong signals and were successfully identified in the correct places. The phosphorus signal was very low due to two reasons: the nm scale thickness of the film and the detection limit of EDS. As mentioned above, EDS depth resolution is a function of the electron beam accelerating voltage. Monte Carlo simulations have accurately described and depicted the interaction volume of electron beams at different accelerating voltages. Typically, the interaction volume of an electron beam is around 1 μm. Because our film is only on the order of 5 nm, it constitutes only .5% of the entire interaction volume. The detection limit for EDS is typically 1000 ppm or 0.1 wt%. Accordingly, lighter element phosphorus is likely to show a weaker signal as compared to the Al and Cu heavier

elements. As a result, at the growth ring region, we were unable to detect any significant signal for elemental phosphorus, seen in Figure 2.20 below.

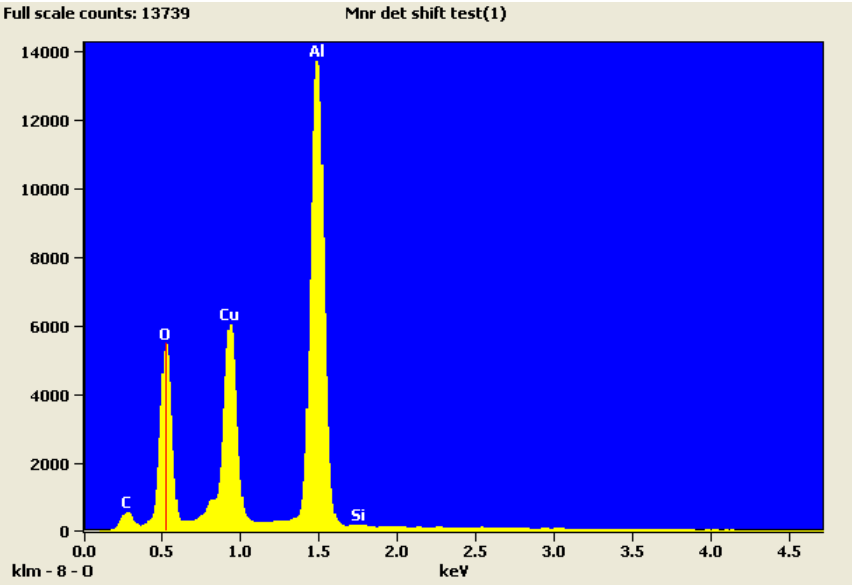

Figure 2.29: EDS scan for phosphorus grown on sapphire at the growth ring.

Despite not being able to detect phosphorus in the region of the growth ring, a scan of the middle of the wafer revealed more favorable results. However, the signal of the phosphorus detected is still an order of magnitude smaller than the peaks detected for elemental Al and O. This is to be expected due to reasons listed above. Additionally a potential explanation for the favorable responses away from the growth ring is simply because there is more phosphorus in the sampling region. The EDS scan which showed a positive result is seen in the figure below.

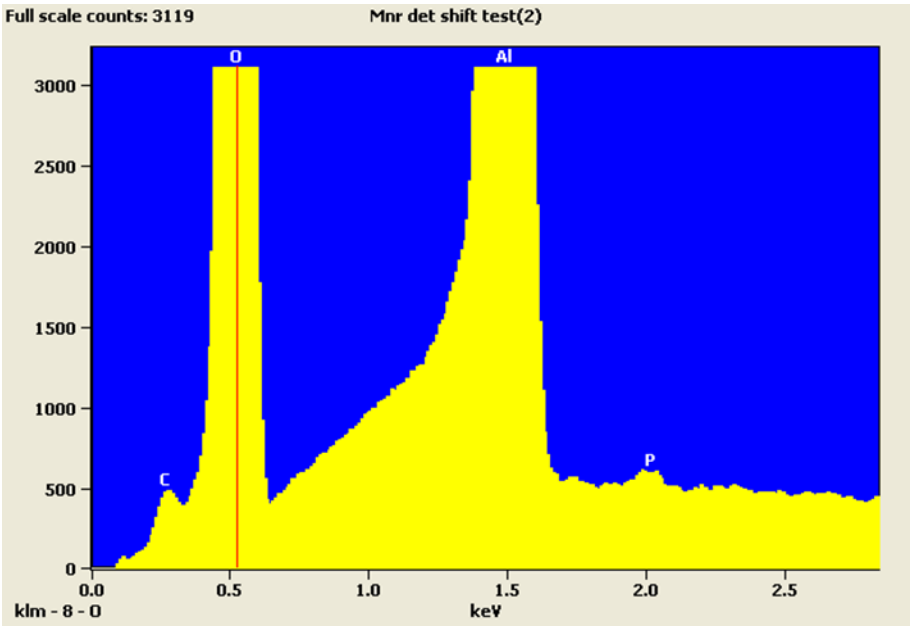

Figure 2.30: EDS scan for phosphorus grown on sapphire in a region away from the growth ring. The phosphorus peak is visible and occurs around 2.0 keV. However, the peak intensity is still very low as compared to the Al and O signals.

Conclusion and outlook:

In conclusion, a positive EDS signal along with XRR verifies the presence of a thin film of elemental phosphorus that we successfully deposited on a sapphire substrate. By closely monitoring the temperature of the substrate, we were able to do iterations of depositions within temperatures between -28°C and 10°C. Growth was halted once the substrate temperature rose above 10°C, a consequence of the blackbody radiative heating. We used a similar method described above for the deposition of thicker b-AsP films. Utilization of this growth technique allowed for us to demonstrate successful deposition of pure phosphorus on a sapphire substrate. Growth was confirmed both visually and the presence of a thin film was substantiated by XRR measurements. Future work involves the conversion of the r-P to b-P. Currently in our group,

efforts are being made towards attaining this goal. Due to the hardness and toughness of sapphire, high pressure approaches may be explored. However, based on the evidence presented in this body of work, it is my belief that the low-pressure route described in this thesis can be a viable route towards synthesizing large area b-P on wafer.

2.8 References

(1) Arthur, J. Molecular Beam Epitaxy. Surf. Sci. 2002, 500, 189-217.

(2) Panish, M.B. Molecular Beam Epitaxy. Science. 1980, 208, 916-922.

(3) Sze, S.M. Semiconductor Devices. 2nd ed.; John Wiley & Sons, Inc. 2002.

(4) Liu, W. Fundmanetals of III-V Devices. John Wiley & Sons, Inc. 1999.

(5) Chen, Y.; Bagnall, D.M.; Koh, H.; Park, K.; Hiraga, K.; Zhu, Z.; Yao, T. Plasma assisted molecular beam epitaxy of ZnO on c-plane sapphire: Growth and characterization. J. Appl. Phys. 1998, 84, 3912-3918.

(6) Goldstein, L.; Gias, F.; Marzin, J.Y.; Charasse, M.N.; Roux, G. Le. Growth by molecular beam epitaxy and characterization of InAs/GaAs strained-layer superlattices. Appl. Phys. Lett. 1985, 47, 1099-1101.

(7) Bean, J.C.; Feldman, L.C.; Fiory, A.T.; Nakahara S.; Robinson, I.K. $Ge_x Si_{1-x}$/Si strained-layer superlattice grown by molecular beam epitaxy. J. Vac. Sci. Technol. 1984, 2, 436-440.

(8) Welty, J.R.; Wicks, C.E.; Wilson, R.E.; Rorrer, G.L. Fundamentals of Momentum, Heat, and Mass Transfer. John Wiley & Sons, Inc. 2008.

Chapter 3: Atomic Layer Deposition, Annealing, and Subsequent Characterization of AsP Thin Films

3.1 Motivation:

Because our films were demonstrated to oxidize in air by XPS, it was necessary to encapsulate them in an encapsulation layer for protection during processing. Processing steps implemented include a post-growth annealing procedure. The rationale used for including this step was to induce a phase change from the as-deposited amorphous film to the crystalline b-AsP film. This chapter begins with a brief fundamental discussion on the mechanism and surface science behind atomic layer deposition (ALD). Next, the annealing conditions that were attempted along with results are discussed. Finally, detailed characterization results including Raman and electron microscopy techniques are shown for our annealed films.

3.2 ALD Fundamentals: Surface Kinetics and Mass Transport

3.2.1 Abstract

The surface chemistry and physics of Atomic Layer Deposition (ALD) is reviewed. A detailed description of the underlying mechanistic principles of ALD is presented, including discussion on reaction types and kinetics, surface chemisorption, and growth mechanisms. A general expression for the surface chemisorption is derived from fundamental chemical rate kinetics. In addition, the mass transport properties of ALD are examined and the relevant governing equations and parameters are introduced. By heavily considering both the surface

reaction rate kinetics and the mass transfer of the system, a rigorous physical description of ALD is obtained. Understanding this process is critical to current nanoscale research, as ALD is an excellent tool for fabricating complex nanostructures.

3.2.2 Introduction

Atomic Layer Deposition (ALD) is a thin film deposition technique capable of fabricating high-quality, high-aspect, uniform inorganic thin films. Specifically, ALD has the ability to deposit exceptionally conformal films onto very complex structures while maintaining precise thickness control (sub-monolayer). These benign characteristics differentiate ALD from other surface deposition techniques, and allow ALD to be used for a variety of applications where high precision is required such as in the semiconductor industry. Although experiments and the methodology of ALD as seen in the literature date back as early as the 1960s, intense multidisciplinary research regarding the technique did not occur until the 1990s and beyond. The rapid growth of the semiconductor industry during this time led to an increased demand in the miniaturization of microelectronic devices in order to further increase computing power. This served as the impetus for the influx of theoretical and experimental studies on ALD, along with the discovery of numerous applications of the technique. ALD is one of the main enablers of the rapidly growing field of nanotechnology as the precise sub-monolayer coating mechanism enables coating of complex nanostructured.

The fundamental operation of ALD is shown in the schematic below. Essentially, ALD utilizes sequential exposure of the substrate to two different chemical precursors. The precursors undergo gas-solid surface reactions and are self-limiting in nature. Because the chemical reactions are self-limiting, the films formed are extraordinarily conformal as the precursors have

a higher affinity to chemisorb to the substrate as compared to each other. Thus unlike other deposition techniques where various uneven growth modes such as the Volmer-Weber and Stranski-Krastanov are common, ALD yields smooth, uniform films. In addition, the statistical approach commonly used as a physical description of deposition techniques is not valid for ALD again due to the self-limiting nature of the surface chemical reactions.

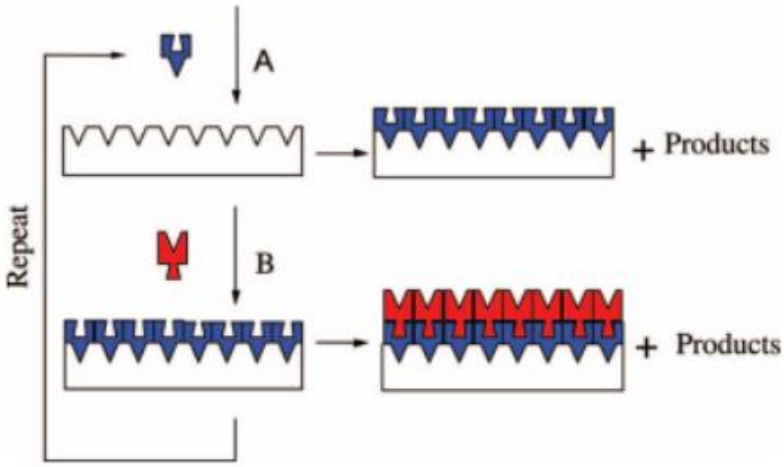

Figure 3.1: The typical ALD process involving sequential exposure of precursors A and B to the substrate. Notice the pin-hole free, conformal growth of the film, along with the repetition of the AB growth mechanism. It should be noted that after each self-limiting chemical reaction occurs, a purge is required to remove any remaining unreacted precursor molecules.

Understanding the underlying physical principles that govern ALD is desirable in order to formulate and implement new applications of ALD to state of the art devices. For instance, with ongoing intense research focused on fabricating and investigating new nanostructures, ALD could serve as a useful technique in functionalizing these materials. This purpose of this work is twofold: first, to give the reader a rigorous yet comprehensible description of the surface reaction kinetics and second, to illustrate the mass transport principles involved in ALD.

3.2.3 Surface Science of ALD

There are two types of adsorption processes involved in deposition, physisorption and chemisorption. The primary difference between the two involves the different interaction mechanisms involved. In physisorption, weaker intermolecular bonds such as hydrogen or Van-der Waals forces are involved. In physisorption, the chemical structure of the adsorbent molecules do not change, and in general the process is reversible. In contrast, chemisorption involves the breaking and subsequent formation of new bonds and can be irreversible or reversible. For a reaction to be self-limiting, the adsorption process must be irreversible by definition since a reversible mechanism would result in non-conformal deposition.

Comprehending the kinetics of the adsorption kinetics can be described by the two elementary adsorption and desorption elementary rate reactions.

$$\begin{aligned} \| * + \mathrm{A(g)} &\xrightarrow{r_a} \| * \mathrm{A} \\ \| * \mathrm{A} &\xrightarrow{r_d} \| * + \mathrm{A(g)} \end{aligned} \quad (3.1, 3.2)$$

Here, r_a represents the rate of reaction of adsorption, and r_d is the rate of reaction of desorption. It is now useful to now define what's known as chemisorption coverage, denoted most commonly as Q. The chemisorption coverage is essentially the fraction of occupied sites, whereas the quantity 1-Q is the fraction of unoccupied, free sites. We can now define the rates of adsorption and desorption in terms of Q as given below.

$$r_a = k_a p(1 - Q) \quad (3.3)$$

$$r_d = k_d \mathrm{Q} \quad (3.4)$$

It is observed that the rate of adsorption is linearly proportional to the partial pressure p, of the adsorbent species. k_a and k_d values are the adsorption and desorption rate constants, and

have an Arrhenius dependence on temperature, as expected from rudimentary chemical kinetic theory.

$$k_i = A\, e^{-E_i/RT}. \quad (3.5)$$

We can now perform a mass balance taking the surface of the substrate as a control volume. As with all mass, energy, and momentum balances, the general continuity equation is given as

Accumulation = In-Out + Gen

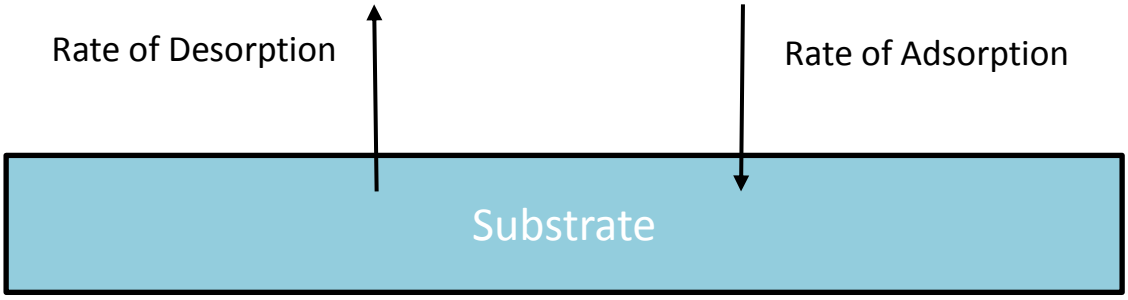

Figure 3.2: Schematic of substrate control volume. The mass transfer is given by balancing the rate of adsorption with the rate of desorption.

However, with the assumption of no chemical reaction at the surface, the generation term goes to zero thus the surface adsorption balance is

$$\frac{\mathrm{d}Q}{\mathrm{d}t} = r_\mathrm{a} - r_\mathrm{d} = k_\mathrm{a}\, p(1-Q) - k_\mathrm{d}\, Q. \quad (3.6)$$

Further simplifications can be made if the system is assumed to be at steady-state, or when the situation is saturated with precursors. At steady-state there is no change in chemisorption coverage with time, thus the left hand side of the equation can be set to zero. The chemisorption coverage can then be solved for, giving the equilibrium value, denoted Q^{eq}. This expression in reaction kinetics is commonly referred to as the Langmuir isotherm,

$$Q^{eq} = \frac{k_a p}{k_a p + k_d} = \frac{1}{1 + (Kp)^{-1}}. \quad (3.7)$$

and the physical assumptions can be clearly corroborated mathematically by expressing chemisorption coverage in this form.

For instance, as discussed earlier, one of the requirements of self-limiting reactions is that they must be irreversible. This occurs during ALD when the system is saturated with precursor gas. An irreversible surface reaction would mean that the rate of desorption reaction is zero, thus the rate constant kd must also be zero. Plugging this into the above equation, it's clear that the equilibrium surface chemisorption simplifies to unity. This is corroborated by experimental results, as ALD is observed to deposit conformal films without the presence of many pinholes or unoccupied surface sites. It's important to note that the chemisorption coverage is not a function of precursor partial pressure when the assumptions of steady state and irreversible reaction are applied. When the system is transient and the reaction proceeds reversibly, the equilibrium chemisorption coverage dependence on partial pressure is seen in the figure below.

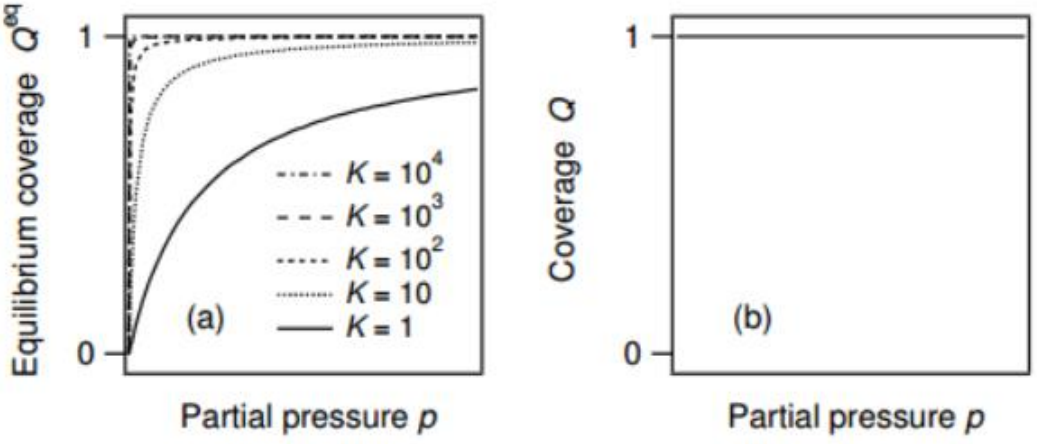

Figure 3.3: Equilibrium coverage as in both the transient reversible condition (left) and the steady-state irreversible condition (right). Logically, at higher K the equilibrium coverage

reaches unity at low partial pressures if the equilibrium constant is large enough. This is because K is defined as k_a/k_d thus if K is large the rate of adsorption k_a must be large.

The transient behavior is obtained by solving the ordinary differential equation of the mass balance. The solution is given by the equation below.

$$Q = Q_{eq}(1 - e^{-(k_a p + k_d)t}) \quad (3.8)$$

3.2.4 Mass Transfer Considerations of ALD

Although the self-limiting nature of the chemical reactions limits the randomness of the impinging flux upon the substrate, the mass transport conditions of the system must still be considered. In the following section, a brief overview of the relevant physical transport principles are discussed. The exposure of the precursor molecules to the substrate is dependent on the flow characteristics. In brief, if there is a superimposed velocity of the precursor molecules over the substrate, then the system is said to be in forced convection. Assuming the flow over flat plate geometry, the Reynolds number can be calculated and the system will be determined to be either in laminar or turbulent flow. The Reynolds number is given as

$$Re = \frac{\rho u_\infty x}{\eta} \quad (3.9)$$

where ρ is the fluid density, $\upsilon_\infty$is the superimposed fluid velocity, $x_c$is the position on the plate, and L is the length of the plate. The Reynolds number is a dimensionless number which gives the ratio of inertial to viscous forces. At low velocities and thus Re, the flow is described as laminar, with a predictable velocity profile in the direction of the imposed velocity. With a high Re (thus usually a high velocity), the flow behavior can transition from laminar to turbulent. Turbulent flow is characterized by highly unpredictable, random flow patterns. The critical

Reynolds number, or the transition between Laminar and Turbulent is 300,000 for the flat plate geometry. The schematic of the flow profile is referred to below

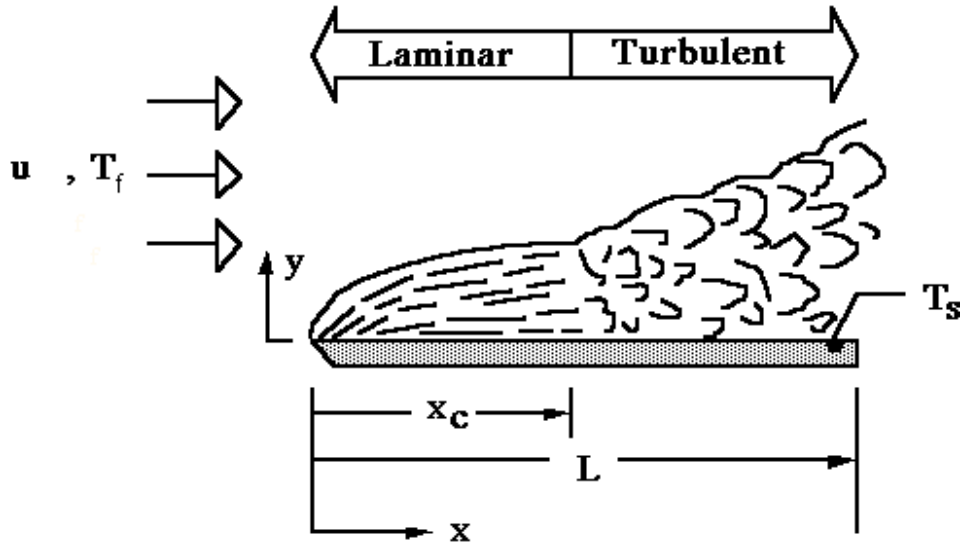

Figure 3.4: Schematic of flow over flat plate including Laminar and Turbulent flow regimes. At a set superficial velocity, there is a characteristic length where a transition between flow modes is observed from laminar to turbulent. The dimensionless Reynolds number is directly proportional to the flat plate length. Reynolds numbers above 10^6 for flat plate flow are characteristic of turbulent flow.

Once knowledge of the flow regime is obtained, the average Sherwood number, or the ratio between the convective and diffusive mass transfer coefficients, can be calculated using an empirically determined correlation for flat plate geometry, shown below:

$$\overline{Sh_x} = 0.644 Re_x^{1/2} Sc^{1/3} \quad (3.10) \text{ for average Laminar flow}$$

$$Sh_x = 0.0296 Re_x^{4/5} Sc^{1/3} \quad (3.11) \text{ for local Turbulent flow}$$

$$\overline{Sh_x} = (0.037 Re_x^{4/5} - 871) Sc^{1/3} \quad (3.12) \text{ for average mixed flow}$$

$$Sh = \frac{KL}{D} \quad (3.13)$$

where *K* is the convective mass transfer coefficient, *L* is the length of the plate, and *D* is the mass diffusivity. *Sc* is known as the Schmidt number and is the ratio of viscous diffusion rate to molecular mass diffusion rate and is equal to the kinematic viscosity divided by the mass diffusivity coefficient.

$$Sc = \frac{v}{D} \quad (3.14)$$

Once the Sherwood number is calculated, the flux of the precursor gas can be calculated using the mass transfer flux equation below

$$N_A = k_c(C_{AS} - C_{A\infty}) \quad (3.15)$$

It should be noted that this is a rather limited description of the mass transfer of precursor gasses onto the substrate. In state-of-the-art ALD systems, the precursor vapor is mixed with inert carrier gases and bubbled into the reaction chamber. Thus due to the bi-component nature of the injected gases, the transport equations for a single-component system may not be valid. Furthermore, assuming flat plate geometry may not be a rigorous enough description of the actual physical set-up. Experimental set-ups available for commercial purchase often feature carrier gas injection perpendicular to or at an angle not parallel to the substrate surface. Thus for calculating the Reynolds number in this situation, knowledge of the relevant correlation for the given flow geometry is essential.

In addition, the mass transfer analysis shown above is a simplified description of the transport picture as only an average value for the mass flux is given. Knowledge of the fully developed concentration profile requires a rigorous derivation of the boundary layer velocity profile. The boundary layer description requires solving a 2-D partial differential equation using relevant boundary conditions and a similarity transform. The governing equation is given as

$$v_x \frac{\partial c_A}{\partial x} + v_y \frac{\partial c_A}{\partial y} = D_{AB} \frac{\partial^2 c_A}{\partial y^2} \quad (3.16)$$

The full derivation of the concentration boundary layer PDE and its solutions are beyond the scope of this review. However, the reader is referred to numerous texts devoted to the fundamentals of fluid, mass, and heat transport.[3,4] This more rigorous approach, though more mathematically involved, gives spatially distinct solutions within the boundary layer, an obvious advantage to the lumped mass transfer coefficient method described above. Currently, a variety of software, such as COMSOL Multiphysics, can compute theoretical solutions to user implemented boundary layer equations and conditions. The utility of computing power should not be overlooked, as boundary layer velocity, heat, and concentration profiles can essentially be probed with very high spatial resolution. For the purposes of ALD, detailed information of the boundary layer behavior of the system is paramount to determining the molecular impingement flux and thus time dependency of the deposition process.

It should be noted that if there is no superimposed velocity, free convection mass transfer conditions apply and the Reynolds number analog, the Grasshof number is checked to determine flow behavior. Free convection for ALD is not a desirable flow condition, as the time of deposition would be significantly increased thus decreasing fabrication throughput.

3.2.5 Conclusion

To obtain a complete description of the time-dependent description of the ALD process, knowledge of the fundamental surface science is essential. In this work, the reaction kinetics of the chemisorption deposition process is derived and discussed in detail. Using fundamental

chemical kinetic theory, an equation for the chemisorption coverage is derived and simplifying assumptions are presented. In addition, the mass transport considerations of ALD are discussed by examining the flow over flat plate geometry. Although the description is somewhat limited, the fundamentals of mass transport and the lumped mass transfer coefficient method are reviewed. In addition, the importance of understanding the mass transfer properties is highlighted as a time dependence of precursor gas exposure to the substrate can be quantified. With ALD applications widely diversifying including deposition upon carbon-based nanostructures and nanomaterials, understanding the underlying physics of this process is critical. ALD has been called an "enabler" of nanotechnology and will continue to be a useful technique in nanotechnology.

3.3 Thermal Annealing of AsP Films

Our low-pressure route for conversion from the as-deposited film to a crystalline b-AsP film utilizes thermal annealing and traditional recrystallization techniques. Because the deposition was done cold, the film quality was expected to be poor since no thermal energy was provided for film reorganization. Essentially, the deposition that was conducted was not a slow, reversible process characteristic of equilibrium growth. Thus the low vapor pressure of phosphorus inhibited the use of any in-situ thermal annealing. As a result, a post-annealing step was hypothesized to be beneficial for inducing the phase transformation from a seemingly amorphous AsP film to orthorhombic b-AsP. Unfortunately, because b-AsP is a relatively unexplored, new alloy, literature reports on the material's phase equilibria is scarce if not nonexistent. As a result, the strategy was to direct our experiments based on the more well-known diagram of b-P. Pictured below is another phase diagram for b-P, this one constructed

from successful experimental conversions of different allotropes of phosphorus to the black phase.

As depicted in the phase diagram, transformations from white phosphorus to black phosphorus occur can occur at temperatures below 200 °C with hydrostatic pressures ranging from 0.5 to 4 GPa. However, the white phosphorus to black phosphorus transition is difficult, namely because of the high vapor pressure of white phosphorus. RP to BP phase transitions can occur at ambient temperatures, though high hydrostatic pressures ranging from 4 GPa to 8 GPa are required. Finally, an empirical linear phase equilibria between RP and BP has been proposed as seen in the red line in Figure 3.5. At higher temperatures, phase transitions can theoretically occur at lower pressures.

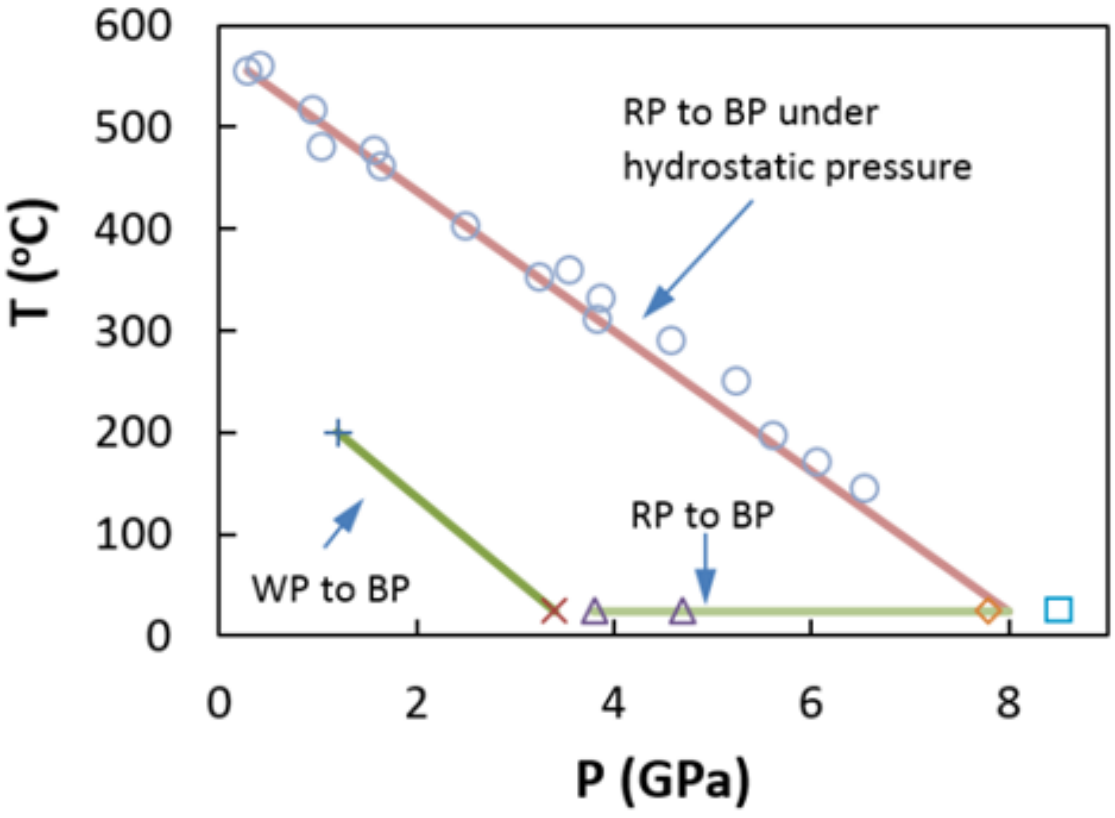

Figure 3.5: Phase diagram depicting successful experimental work on synthesizing b-P. Phase transformations from white phosphorus and red phosphorus to b-P have been demonstrated. The red line indicates an empirical phase equilibria extrapolated from experimental results for the thermal and hydrostatic conversion of RP to b-P.

One of the primary motivations behind the making of this thesis was to exploit the low pressure region of the b-P phase diagram. While synthesizing bulk samples under high hydrostatic pressure may be acceptable, the on-wafer synthesis of b-P is much more restrictive. This is primarily due to the limiting nature of the substrate hardness and toughness. Most semiconductor substrates, including Si and other III-V substrates will fracture under high hydrostatic pressures. As a result, a method that involves low-pressure conversion is highly desirable. Figure 3.6 is another depiction of the b-P phase diagram, with region of interest indicated on the plot.

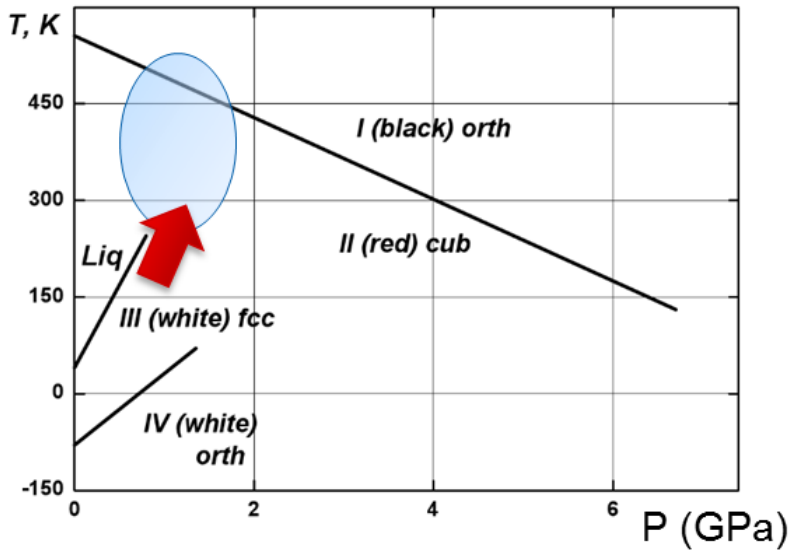

Figure 3.6: Full phosphorus phase diagram with region of interest circled. Annealing experiments were based off of low pressure and high temperature conditions.

It was postulated that if thin films were exposed to temperatures exceeding 450 K, that a low-pressure phase transformation could occur. In Chapter 2, ALD deposition was discussed, and was presented as a possible method for encapsulating thin films of b-AsP. The rationale was to protect thin films of b-AsP from oxidation while processing. With annealing determined to be the post-growth methodology utilized to transform on-substrate RP to b-P, the encapsulation layer now serves two more purposes. First, encapsulation with metal-oxide prevents desorption of the film during annealing- particularly at the higher temperatures. Second, encapsulation also serves to allow for pressure buildup within the film, thus driving the system toward more favorable conditions for transformation.

A schematic of the encapsulated film stack, along with a cartoon of the annealing process is seen in Figures 3.7 and 3.8 below. In order to repeat multiple iterations of the annealing, the 3" wafer was diced into 1 cm x 1cm pieces. These pieces were exposed on the edges to atmosphere, though the aspect ratio of the film is so large that edge oxidation effects were generally ignored.

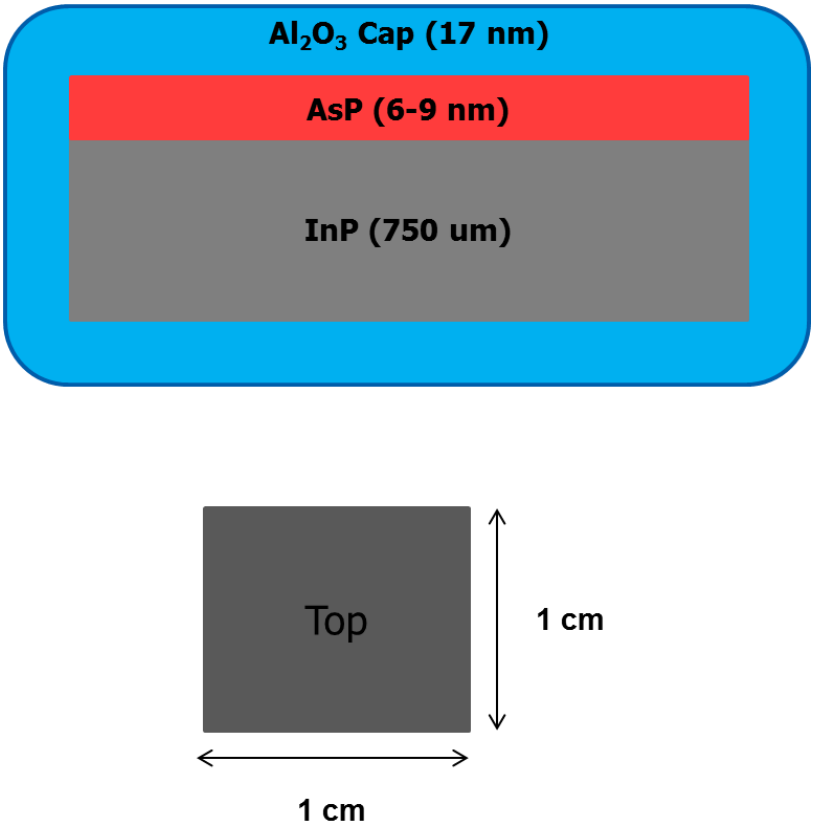

Figure 3.7: Schematic of encapsulated AsP film stack. Substrate is InP, followed by AsP deposition layer, and encapsulated by 17 nm Al_2O_3.

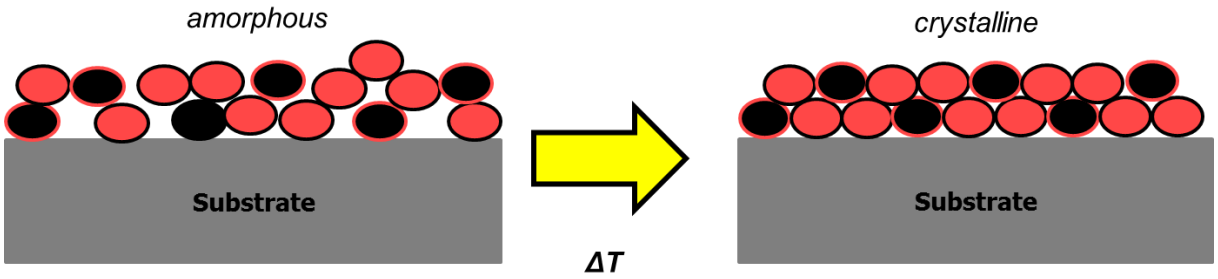

Figure 3.8: Cartoon depicting annealing process. Amorphous film on-substrate is exposed to high temperatures to induce a phase transformation to a crystalline state.

In order to step through all possible process conditions for conversion, a matrix of annealing conditions was attempted. The annealing parameters are shown in Figure 3.9 below. Boxes that are filled with solid red indicate conditions in which annealing was unsuccessful,

whereas those filled with green indicate successful results. The success of each condition was validated by Raman scattering spectroscopy, which will be discussed in more detail in the section below. It is important to note that the most promising annealing conditions were those that had extremely long annealing times. Phase transformations, like chemical reactions, are balances between thermodynamic and kinetic control. The temperature essentially provides the driving force for the process to occur, while the annealing time accounts for the kinetics of transformation. From the chart below, it is clear that the phase transformation appears to be kinetically limited. This means that despite adequate thermodynamic conditions, the process still takes quite a bit of time to complete. The best conditions were 250-400°C at times of 1 to 10 days.

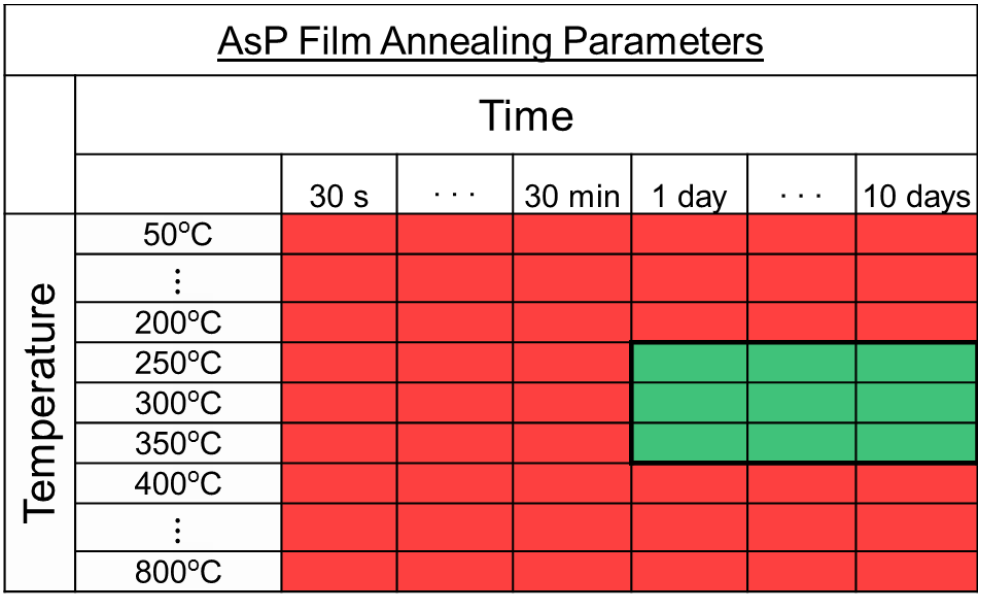

Figure 3.9: Matrix of annealing conditions attempted for conversion of on-substrate AsP to the black phase. Temperatures ranging from 50 to 800°C were attempted at 50°C intervals and times ranging from 30 seconds to 10 days were attempted.

Annealing to improve morphology is a well-known material process. Ultimately, the goal was to cause a transformation from the amorphous red state to the orthorhombic black phase.

Figure 3.10 as seen below depicts the in-plane crystal structure along with the unit cell for b-AsP. Given sufficient thermal energy, post-deposition transformation to this phase is the goal of this thesis. The reason a crystalline phase is preferred over the as-deposited amorphous phase is due to enhanced performance of the former in devices. In particular, the field-effect mobility largely depends on the morphology of the film.

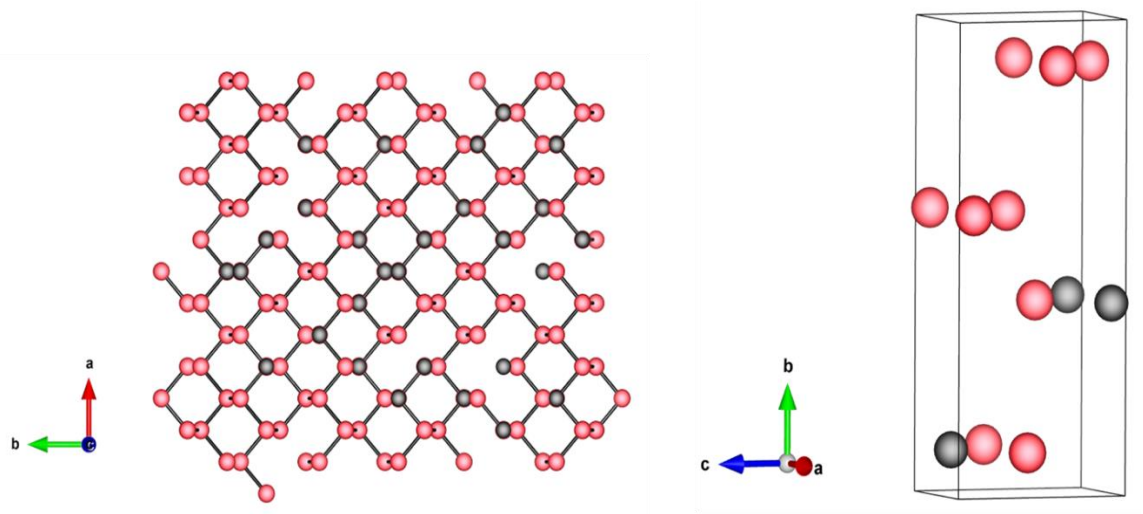

Figure 3.10: Depictions of the crystal structure of b-AsP alloy. The black holes represent phosphorus atoms and the red atoms represent the arsenic atoms. The left image is the in-plane structure along the a and b unit vectors. Similar to a carbon nanotube, a zigzag and armchair direction is seen. The right image is the unit cell of orthorhombic b-AsP, containing portions of three individual layers.

Typically, amorphous films suffer from lower field-effect mobilities as compared to their crystalline counterparts. This is a consequence of the lack of order within the film, which causes unpredictable band structures along with many defects. The grain boundaries and defects caused by an amorphous film effectively scatter free carriers during transport. For FETs, channel lengths are typically on the order of several microns. As a result, free carriers in an amorphous film must traverse across many such boundaries from source to drain. Crystalline films, on the other hand,

contain a pristine lattice with well-ordered, continuous band structure. As a result, the number of scattering events is less than an amorphous film, and is much more favorable for electronic and optoelectronic applications.

In summary, the goal of this thesis is to explore such transitions en route to developing a new method of synthesizing crystalline b-AsP on-wafer. While high-pressure routes have been demonstrated to be successful for bulk synthesis and more recently on-substrate synthesis, such methods have strict limitations on choice of substrate materials. In order to one day realize b-P and b-AsP integration into a wide range of devices, more conventional semiconductor substrates need to be employed for device applications. As discussed in the deposition section, our MBE process is conducted in the absence of heating; such process conditions inhibit surface diffusion and as a result, equilibrium growth. Thus the methodology proposed is to use a post-deposition annealing process to recrystallize the crystalline phase from the as-deposited amorphous film. Rather than using a high pressure approach, the low-pressure high-temperature transformation region of the phase diagram is explored. Results of this two-step method are discussed in subsequent sections, with promising characterization results.

3.4 Raman Spectroscopy

Initial characterization of b-AsP films grown on InP were performed using Raman scattering spectroscopy. Raman scattering is a spectroscopy tool used to probe phonon vibration modes within a material. Through an optical aperture, monochromatic laser sources of various wavelengths are passed from the source to the sample surface. The incoming photons interact with phonon vibrational modes within a lattice and as a result either lose or gain energy. The loss

of energy is known as a Stokes shift, whereas photon-phonon coupling resulting in an increase in photon energy is known as an anti-Stokes shift. After interacting with the lattice, the photons then return through the same aperture and are routed to a CCD detector which is set to detect signal close in energy to the Rayleigh line. Because vibrational modes are low in energy, Raman is measured in the inverse centimeter wavenumber unit cm^{-1}.

3.4.1 Raman Fundamentals

Because Raman measurements make up a large portion of this thesis, a more rigorous treatment of the technique will be given here. This section will serve to give a basic overview of the fundamental physics involved in Raman scattering. While by no means exhaustive, the purpose is to give the reader a survey of an extremely useful nondestructive characterization technique for a wide range of materials. Because the application space of this thesis involves solid materials, we focus now on the characterization of solids despite Raman being applicable for gasses and liquids.

Figure 3.11 displays spectra for the bulk b-AsP as reported by Liu et al. As expected, the Raman modes vary with alloy composition. This is because vibrational modes depend solely on the bonding within a material; in particular, the atomic weight of the bonding species involved as well as the bond strength. Pure BP exhibits three Raman active modes corresponding to the A^1_g, B^2_g and A^2_g peaks. With increasing As concentration, new As-As and As-P modes appear with red-shifted energy as a result of the heavier mass of As versus P. This results in less energetic vibrational modes as phonon vibrations can be loosely modelled by the classical mechanics ball and spring model. At compositions of b-$As_{0.83}P_{0.17}$, the more energetic B^2_g and A^2_g phosphorus modes are severely dampened, with more distinct As-As vibrations appearing in the 200- 275

cm^{-1} wavenumber range. As a result, Raman scattering spectroscopy can be used to fingerprint b-AsP alloys since the Raman active modes are heavily composition dependent.

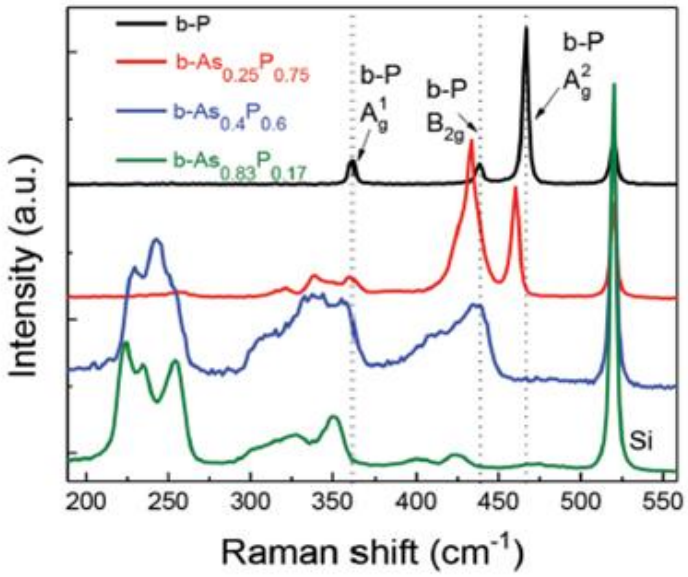

Figure 3.11: Raman spectra of various compositions of b-AsP alloys. The Raman modes can be seen to heavily depend on alloy composition.

We performed Raman scattering spectroscopy measurements on our as-grown InP samples to obtain structural information on our films. The as-deposited spectra can be found in Figure 3.12. We confirmed our composition by XPS to be $As_{0.78}P_{0.22}$ which most closely matches the bulk b-As0.83P0.17 alloy synthesized by Liu et al. Comparison of Raman spectra shows that our measured peaks match reasonably well with the literature. Specifically, the broad signature at Raman shift 200-250 cm^{-1} and the broad peak between 300-360 cm^{-1}. However, unlike the literature spectra, Raman peaks measured from our films were not well-defined. This was believed to result from poor crystallinity within our films. Because Raman scattering is heavily dependent on crystal structure, sharp and well-defined Raman peaks are indicative of lattices with good ordering. An example of this can be seen in RP as shown in **Figure 33**. RP is an

amorphous network of phosphorus and as such contains no long-range bond ordering. The Raman spectrum for RP consists of one extremely broad signature with wavenumber range 350-500 cm^{-1} with no distinct peaks. With this in mind, we believed our films as-deposited suffered from poor-crystallinity.

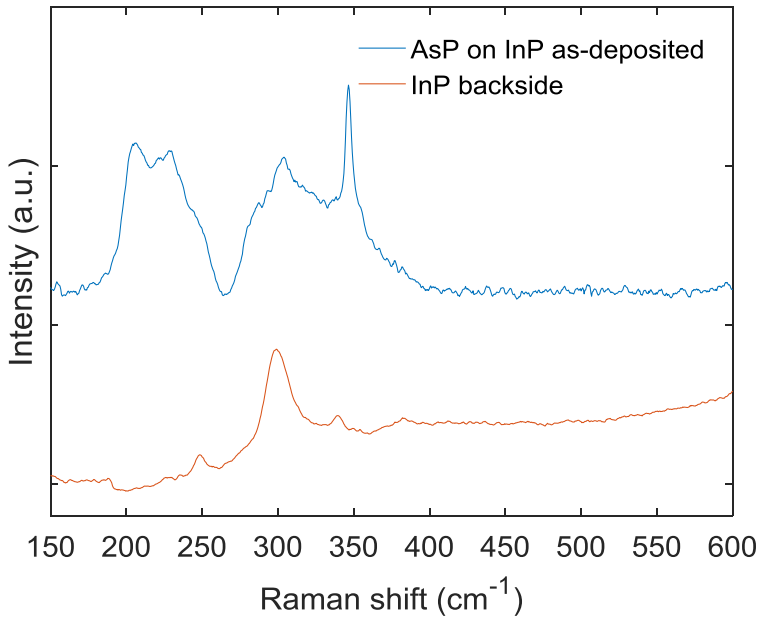

Figure 3.12: Raman spectra of as-deposited AsP on InP. The red curve is spectra taken from the substrate whereas the blue curve corresponds to the spectra taken from the film.

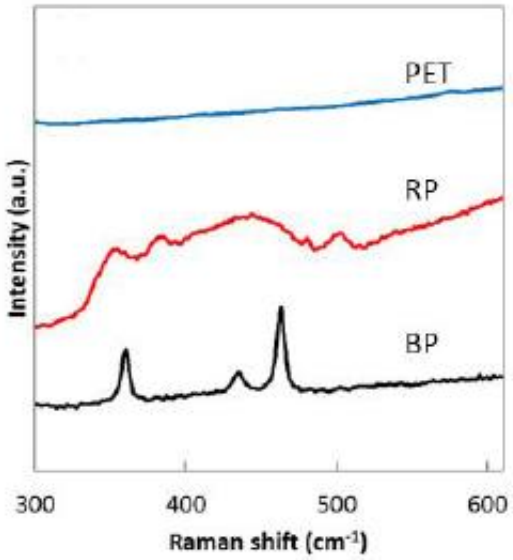

Figure 3.13: Raman spectra for PET flexible substrate, amorphous RP and crystalline BP. Crystalline BP shows well-defined Raman signatures as compared to the broad and undistinguishable signal from RP.

3.5 Electron Microscopy

In order to best understand further understand the structure of our films, we visualized our stacks using transmission electron microscopy. The first batch of films was sent to a collaborator at Brookhaven National Laboratory for analysis. At best, Raman spectroscopy provides a semi-quantitative overview of the structure of our films. To extract and visualize the exact structure of our films, an electron microscopy technique must be used. Transmission electron microscopy has the capability to provide nanometer scale resolution at the worst and atomic scale resolution at the best. Images of our film stack would be able to give us thickness information as well as any noticeable deformations or artifacts from deposition. Cross-sectional TEM first requires the construction of a cross-section from the original film. Our collaborators at Brookhaven used a focus ion beam process to mill out a trench for subsequent TEM exposure. We repeated the process at UCLA, which is discussed below.

Figure 34 below is a low resolution TEM image taken by a JEOL 1400 TEM. The JEOL 1400 TEM is a low magnification TEM with accelerating voltage of 120 kV. While not nearly as powerful as high-resolution TEM (HRTEM) modules, the JEOL 1400 provides useful structural information on the nm scale. Microscopy images reveal an AsP film with thickness 5.9 nm, and an encapsulation Al_2O_3 layer thickness of 17.08 – 18.37 nm. Interestingly, the film is not nearly as smooth as one would expect from an MBE process. Typically, because of the precise monolayer control afforded by MBE, films have uniform thickness and do not possess significant roughness.[5] However, for our films, we attribute both the film and oxide layer roughness to the annealing process.

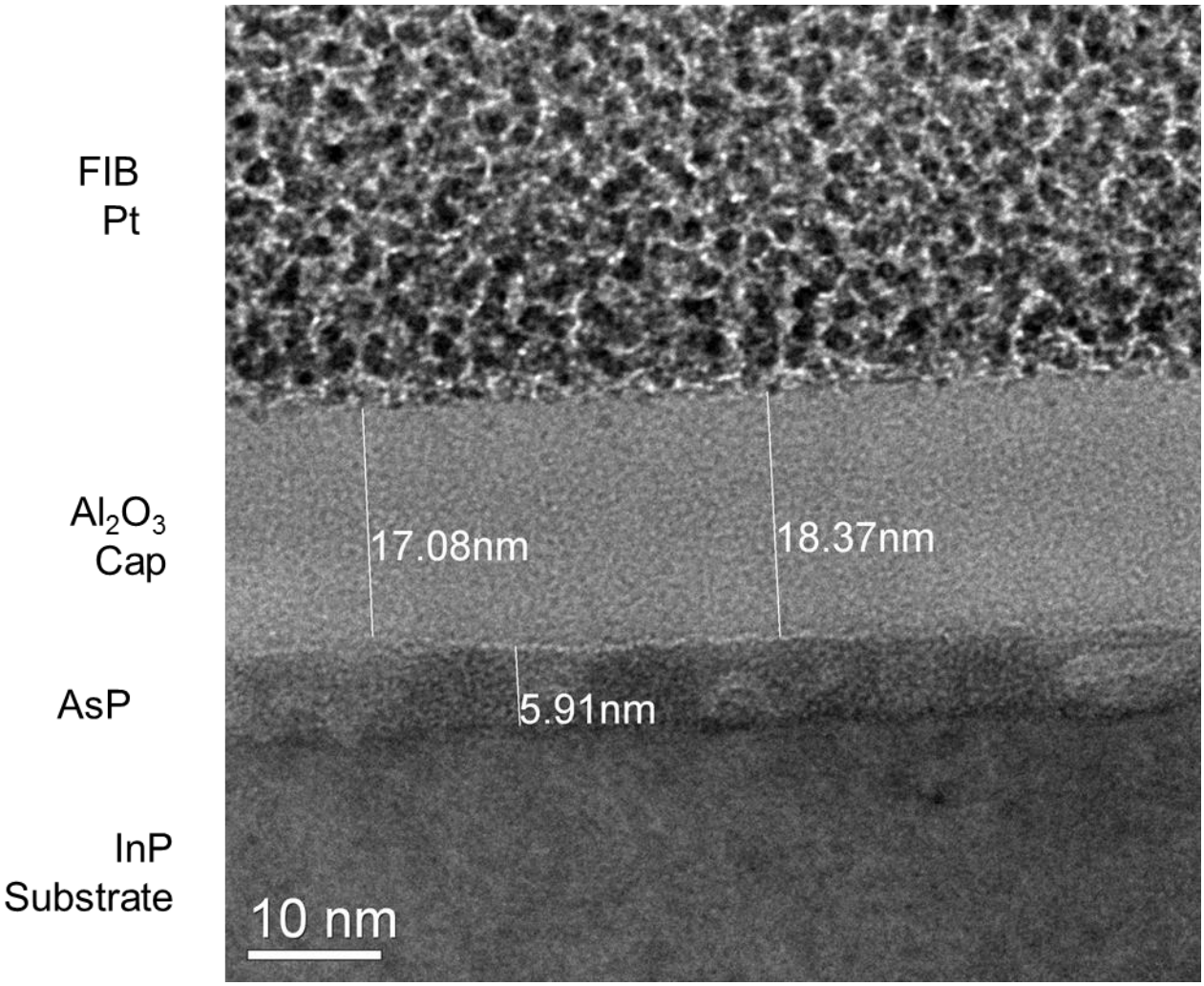

Figure 3.14: Cross sectional TEM image taken from the JEOL 1400. The film stack regions that are visible include the InP substrate, the AsP layer, as well as the Al_2O_3 passivation layer. Thicknesses are also identified from the microscopy images, which are identified in the image.

Scanning Transmission Electron Microscopy Imaging:

Figure 3.15 depicts a low magnification scanning transmission electron microscope (STEM) image of our cross-section as obtained by a Hitachi 2700 STEM. Conceptually and practically, STEM functions similarly to TEM in that an electron beam is passed through a sample and either the subsequent transmitted (bright field) or diffracted (dark field) beams are detected. However, STEM differs in that the electron beam is focused to a much smaller spot, typically on the order of sub-nanometer diameters. The beam is then scanned across the region of interest and stitched to give an image. The small spot size of STEM allows has advantages for characterization techniques in which spatial resolution is significant. For instance, line scans of compositional methods such as electron energy loss spectroscopy (EELS) and energy-dispersive X-ray spectroscopy (EDX) can be accomplished using an STEM.

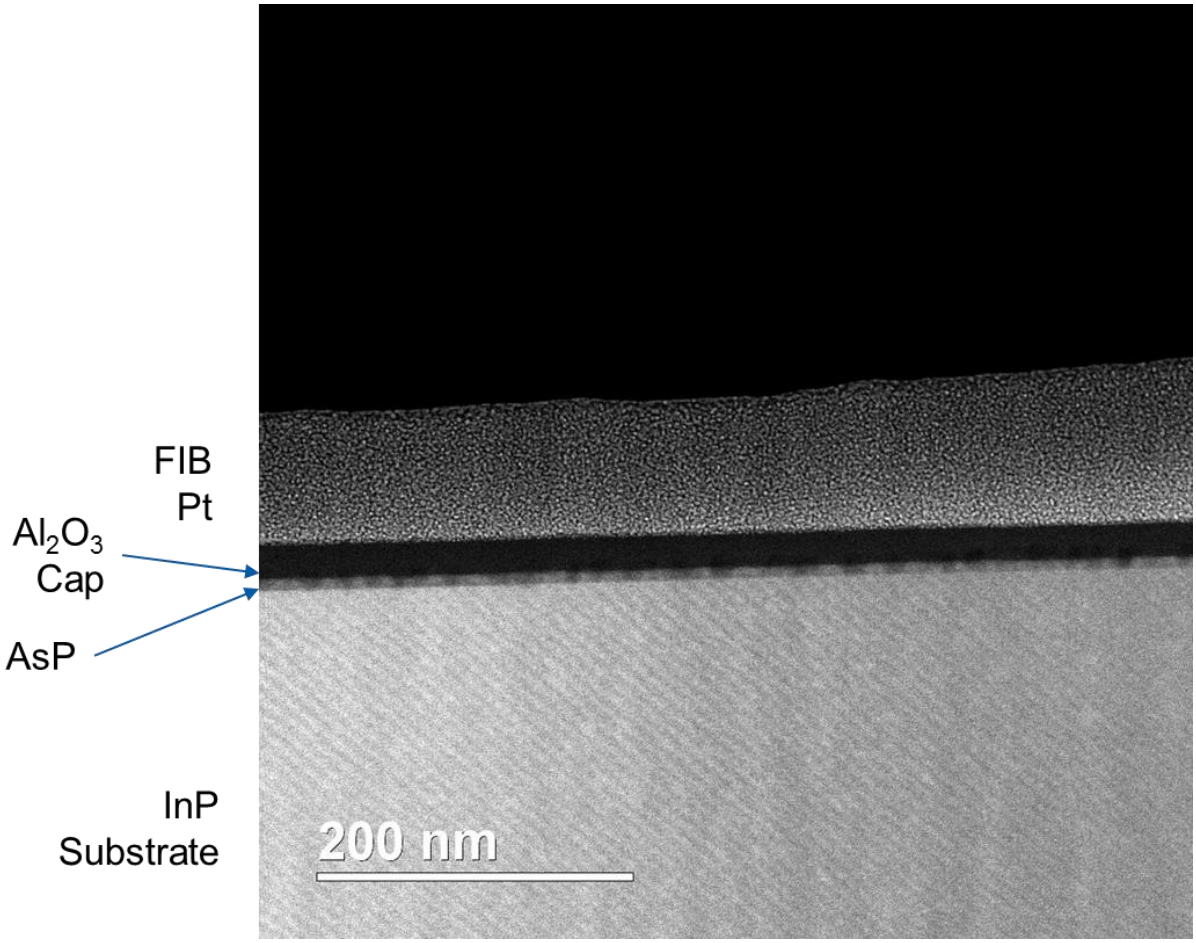

Figure 3.15: Cross-sectional low resolution STEM image of film stack. Crystalline InP is seen as well as the AsP and Al_2O_3 layers. The FIB Pt protection layer is also visualized.

High magnification images were also obtained from the Hitachi 2700 STEM as seen in Figure 36. Under high resolution, the image plane clearly depicts the crystal structure of InP. The incident electron beam images the perpendicular image plane. For InP, this is the (111) face. Somewhat discouragingly, the AsP layer shows no crystallinity under STEM imaging. Initially, it was thought that the deposition layer was amorphous, despite seeing indications of improved crystallinity from the Raman spectra. However, upon discussion with committee members, and in particular, Professor Mark Goorsky, a possible explanation was given. Although the InP zone

axis is in focus here, grains within the AsP layer may not be aligned to the incident beam. Essentially, for a plane to be visualized under TEM and STEM, the incident beam must be orthogonal to a plane within the grain. Because it was believed that the annealed film was polycrystalline, many different orientations of grains were expected. Additionally, because our process was not epitaxial, we expected no preferred orientations within the AsP film. As a result, by simply tilting the substrate, different orientations may be able to be detected.

Interestingly, the thickness measured from our STEM differed from those obtained by the JEOL TEM. Previously, the AsP layer was determined to be approximately 6 nm, whereas in our STEM measurements, we see a 9 nm AsP layer. One reason for the discrepancy could be that the deposition is so non-uniform that there is a 3 nm deviation within the same sample. However, more realistically, we believed that the measurements from the JEOL TEM were off. Since the magnification is so much lower, inaccuracies in the thickness measurements could cause an underestimation or overestimation of the film thickness. However, our XRR measurements aligned best with the JEOL TEM measurements, with a 6 nm film thickness. Because we were unable to identify any crystalline features within our films, we decided to repeat the process at our facilities at UCLA.

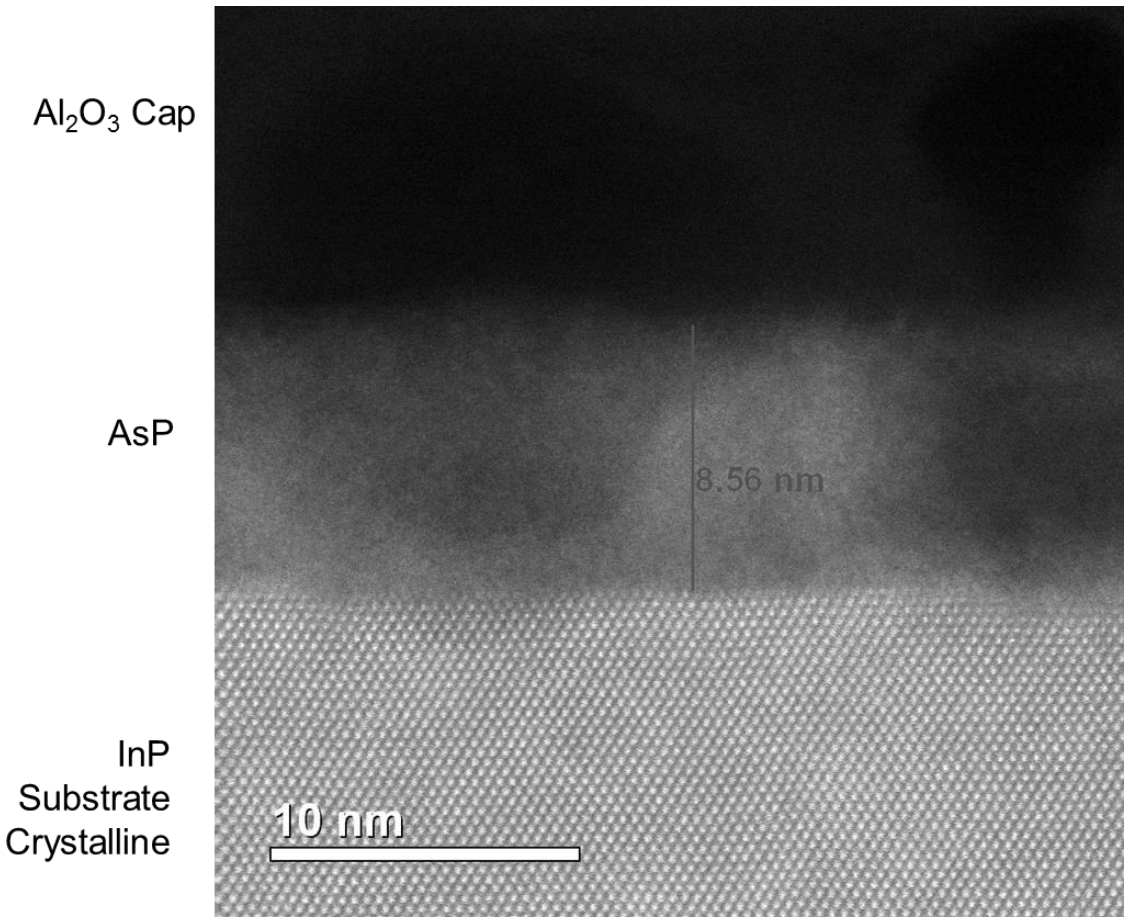

Figure 3.16: High resolution STEM images which shows crystalline InP substrate and seemingly amorphous AsP deposition layer. The thickness of the deposition layer was measured to be 8.56 nm, a 2 nm change from that measured from the JEOL TEM.

Dark Field STEM

The high-resolution STEM images were collected in annular dark-field. For electron microscopy, dark-field detects the scattered electrons as compared to transmitted beam. In particular, annular dark field microscopy was employed to generate Figure 3.16. Because the detection mode is in dark-field, the contrast within the film can be seen but without any conclusive distinguishing features. Given that within the AsP film itself shows some contrast, it

was expected that using a different electron microscopy visualization technique, that more of the structure of the film layer may be able to be seen.

Electron Energy Loss Spectroscopy:

Electron Energy Loss Spectroscopy (EELS) is a particularly useful technique that can potentially give compositional information of a sample. EELS is run in STEM mode and essentially measured the energy loss of an incident electron beam due to interaction with the specimen. Inelastic scattering of the incident beam can be caused by a variety of interactions including band-to-band transitions, intra-band transitions, phonon excitations, and core shell ionizations. Although not nearly as accurate as EDX, the core shell ionizations can give compositional information of various materials. EELS line scans are made possible by STEM mapping since in STEM, the electron beam is both focused to a much smaller spot size and is able to be scanned across samples.

Figure 37 depicts EELS measurements obtained from Brookhaven for our films. In order to validate the composition of our films as measured by EDX, we chose to scan a vertical line down the cross-section of our film stack. Additionally, EELS served as an adequate metrology technique to detect any oxidation during the annealing process. There are three regions of interest here which would yield different expected compositional profiles, the Al2O3 passivation layer, the AsP deposition layer, and the substrate. Figure 37 focuses on the oxidation of the film. Interestingly, we saw significant oxygen content both in the Al_2O_3 oxide as well as in the AsP deposition layer. A couple different explanations can be given for the seemingly high oxygen content. First, the annealing process could have caused significant interdiffusion between the AsP and oxide layers. However, although the oxygen species diffusion is relatively mobile (high diffusivity)[6], Al_2O_3 is relatively inert and has been demonstrated to be thermally stable at

temperatures much higher than our process conditions. Thus oxygen interdiffusion, while possible, does not offer a reasonably sound explanation for the high oxygen content within the AsP film. Perhaps the primary reason for the detected oxygen is indeed oxidation of the film. Although the samples were passivated with ALD Al_2O_3, the 3" wafers were subsequently cleaved to yield many 1 cm x 1 cm samples. As a result the edges of the films were exposed to ambient conditions. Additionally, the sample handling was not under hermetic conditions. We shipped the samples under atmosphere, and additionally, during loading in the TEM and STEM conditions, the samples were not under nitrogen or vacuum. We now suspect that our films were exposed to atmosphere for prolonged periods of times (weeks), which could be a sufficiently long timescale in which edge oxidation could compromise the film.

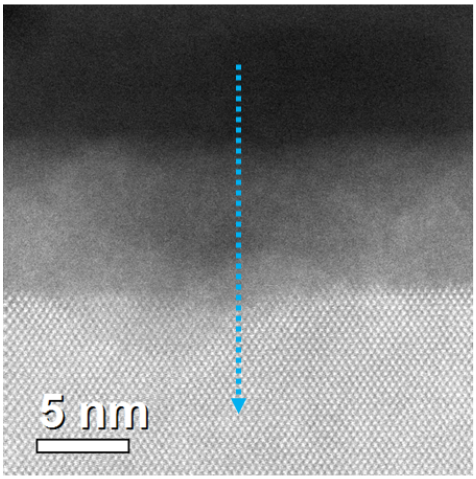

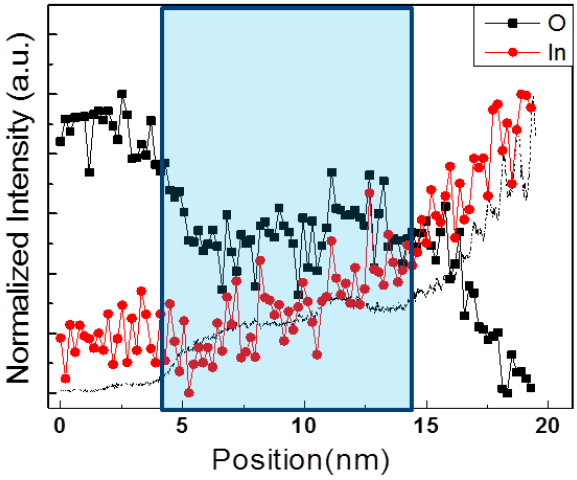

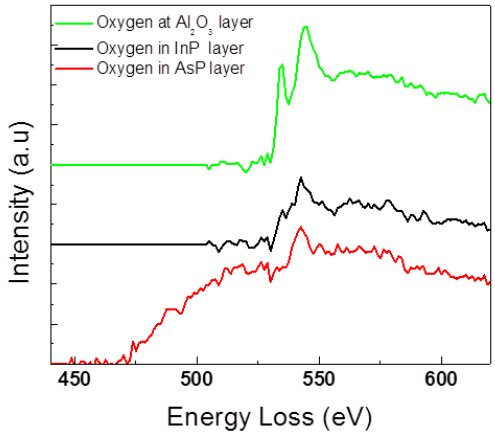

Figure 3.17: EELS line scan performed in STEM mode Hitachi 2700. The dashed blue line indicates the vertical profile that was probed. The top right figure shows our three different matrices, with the highlighted blue box indicating our film region. The bottom right plot depicts oxygen peaks detected in each of the film stack regions.

3.6 FIB/TEM Experiments at UCLA

Because of the many questions that remained following electron microscopy analysis at Brookhaven, TEM experiments were repeated at UCLA. In order to cut out a cross-section, we used a FIB process embedded into our SEM system. First, a Pt protection layer was e-beam evaporated onto our film. Upon exposure to an electron beam, the film began to form bubbles. This is attributed to heating effects and outgassing upon exposure to the energy from the electron beam. These artifacts were seen to evolve in-situ, and may have damaged the film. Figure 3.18, depicted below depicts a top-down image of the film-stack surface, with altered regions of Al_2O_3 depicted along with the e-beam Pt.

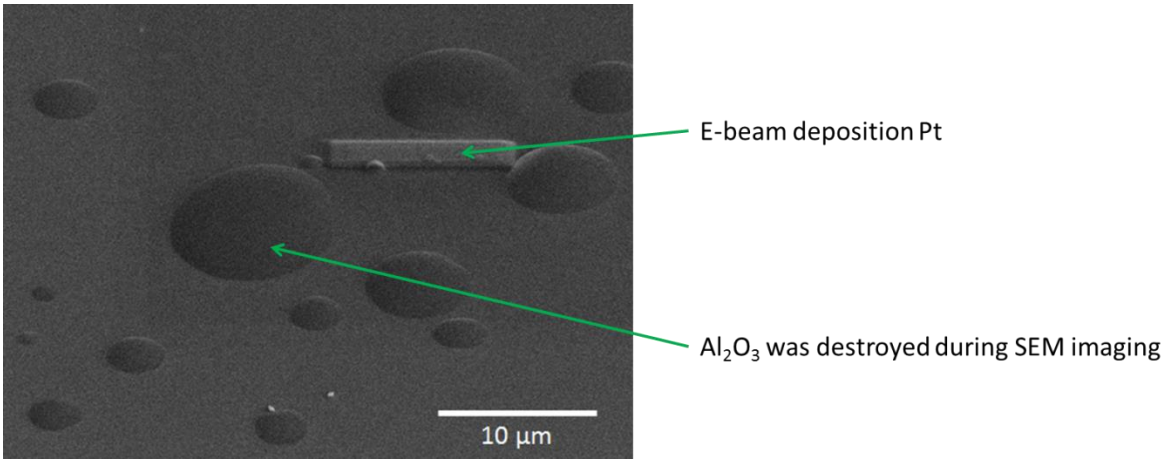

Figure 3.18: SEM top-down image of Al_2O_3, AsP, and InP film stack. Green arrows depict the e-beam deposition Pt protection layer as well as regions in which the Al_2O_3 may have been destroyed.

Following Pt deposition, a trench like structure was milled out. The shape of the trench defined was a 3D V shape, which is the conventional shape and method for cross-sectioning samples. The cross-section is then lifted off using a needle and placed on a copper grid for imaging. Once the cross-section is separated from the original film stack, it is then subject to thinning from the ion beam. The sample must be sufficiently thin (~100 nm) in order for the specimen to be able to transmit the e-beam during TEM. An SEM image of the cross-section is seen in Figure 3.19. There appears to be large regions of the film, on the order of 1 μm that were destroyed during the FIB process. This most likely occurred during FIB thinning of the sample. Several reports have commented on the instability of b-P, especially when subjected to an electron beam.[7] This explanation can be extended to b-AsP as well; thus we attribute the film damage to the volatile nature of our material.

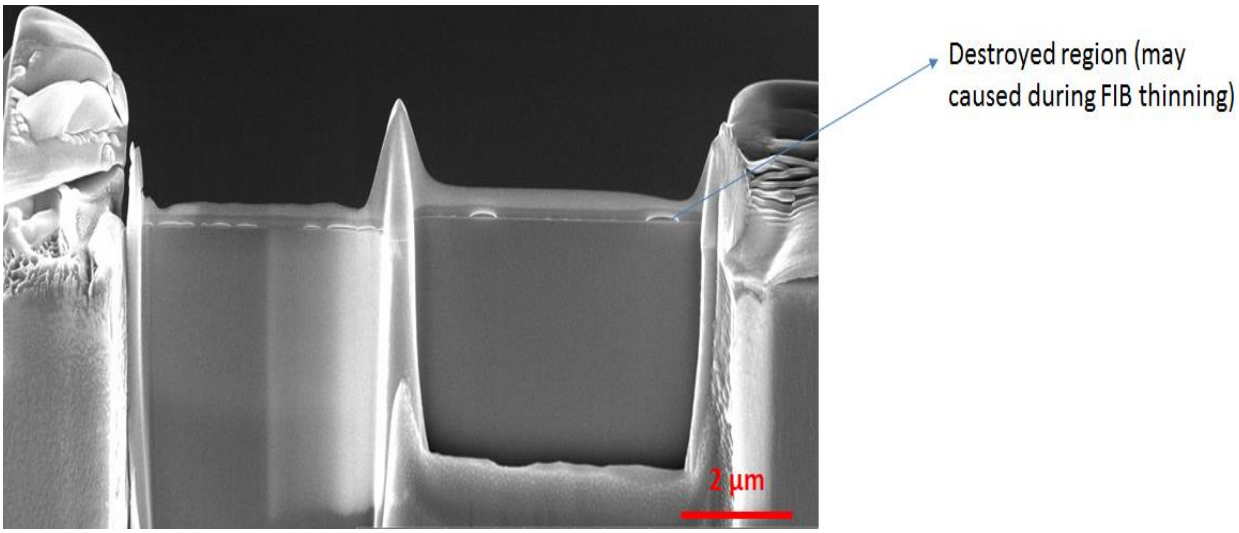

Figure 3.19: SEM image of cross-section of AsP on InP. Image reveals regions in which the film was destroyed due to FIB thinning.

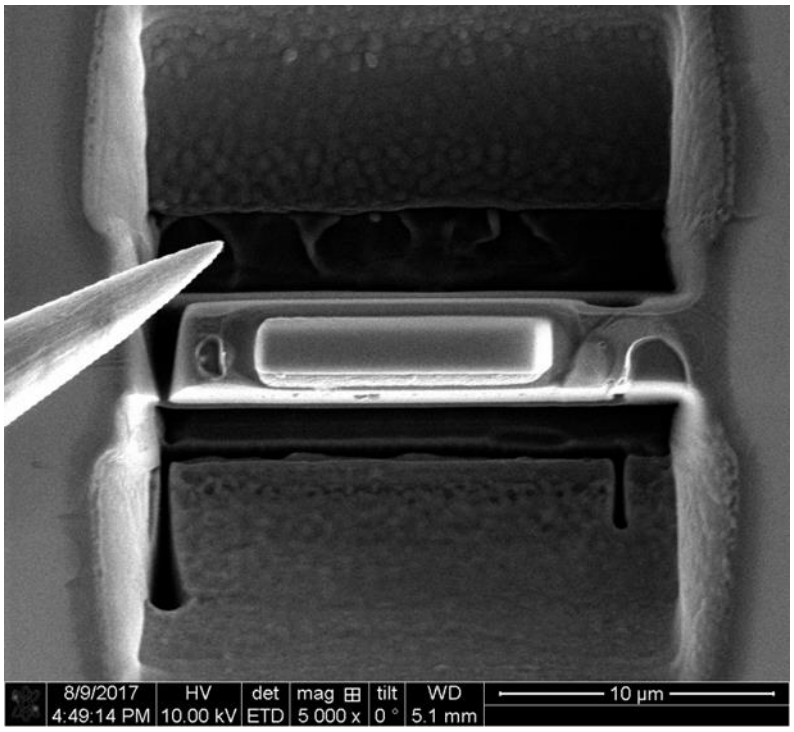

Figure 3.20: SEM image of lift off of Pt protected cross-section. The needle is attached to the Pt layer, which subsequently helps elevate and remove the embedded cross-section from the film.

The TEM used at UCLA boasts far better resolution than the tool used at Brookhaven. Experiments were conducted by Tingyu Bai, a collaborator from Professor Mark Goorsky's group. We subjected our films to 300 kV e-beam in a FEI Titan TEM in the hopes of elucidating the morphology, and in particular the crystallinity of our films. Because of its immense e-beam accelerating voltage, the Titan boasts atomic resolution; as a result, localized atomic arrangement and order can be visualized. Figure 42 displays a high resolution TEM (HRTEM) image of our film stack. As compared to images from the JEOL 1400 TEM as well as the Hitachi 2700 STEM, much more structural information can be visualized from this micrograph taken from the Titan. The image shows an amorphous matrix with small, crystalline grains on the order of 5 nm. No contrast was seen between the Al_2O_3 passivation layer, and the AsP layer, though the Pt and the substrate are distinguishable from the deposited layers.

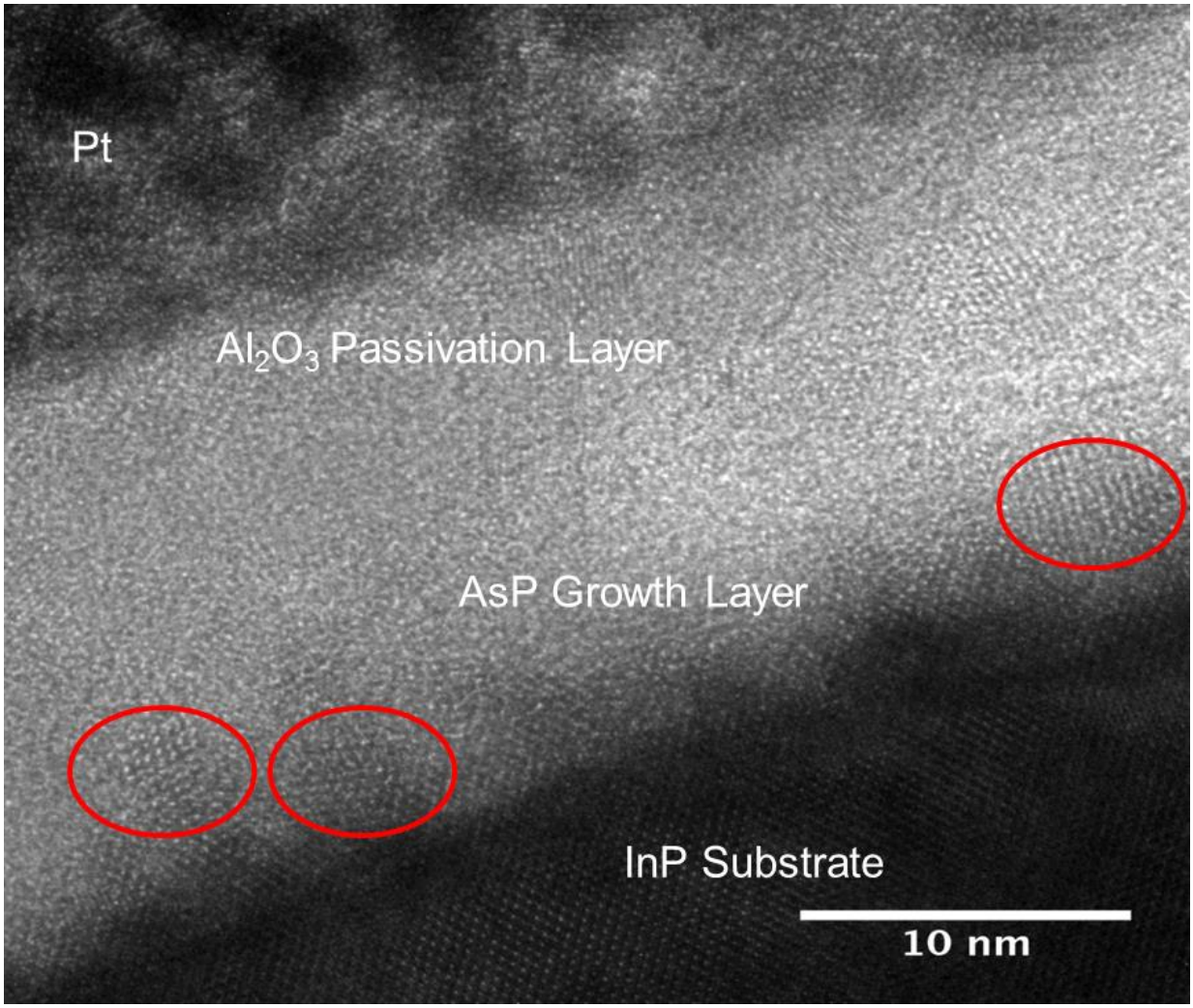

Figure 3.21: HRTEM image of film stack. Atomic resolution is seen. AsP growth layer and Al2O3 passivation layer do not show distinguishable contrast. Nanocrystalline grains throughout the deposited layers are seen.

In order to identify the grains and which crystal structure they represent, the HRTEM image was analyzed using Image J software. By measuring the d-spacing of each family of planes and comparing them to the known data from the International Centre for Diffraction Data (ICDD) X-ray diffraction database, each grain can be identified. Additionally, by measuring the angle between two different planes and comparing to theoretical planar angles, the crystal structure of the visualized grain can be further validated. In our film, we see crystallized grains

of InP, Al_2O_3 and what we confidently believe is b-AsP. Further discussion of our successful methods can be seen in our submitted manuscript, which is published in this thesis in Chapter 5. Al_2O_3 is known to crystallize under certain annealing conditions[8], especially when deposited via ALD. This is because Al_2O_3 initially goes down amorphous under standard deposition conditions. With thermal annealing, the barrier to transform to a crystalline state is relatively low, and as a result polycrystalline films can be created. As far as InP grains within the growth layer, elevated temperatures are known to cause In diffusion[9], which bonded with the P region to create InP.

In conclusion, we characterized our films by examining cross-sections of our films via various electron microscopy techniques. Two sets of experiments were conducted, one at Brookhaven National Lab and another using our facilities at UCLA. Cross-sections were created via FIB techniques, and film thicknesses were able to be identified via SEM and TEM. By using STEM mode, our collaborators at Brookhaven believed that our AsP films were still amorphous despite having undergone an annealing process. Additionally, EELS measurements conducted in STEM mode revealed an oxidized AsP film, most likely a consequence of poor handling of our samples. Experiments conducted at UCLA were much more promising. Although SEM images revealed a partially damaged film following the FIB process, relatively useful TEM images were still able to be obtained. By utilizing our HRTEM FEI Titan, single atom resolution was able to be obtained, and images revealed an amorphous matrix with nanocrystalline grains. Thermal annealing resulted in crystallization, and the favorable results are summarized in Chapter 4.

3.7 X-Ray Diffraction

Perhaps the most obvious method for obtaining crystal information is X-Ray Diffraction (XRD). However, several limitations of the sample prevented us from obtaining useful information from XRD. In general, XRD is a bulk technique which requires either polycrystalline, textured, or crystalline samples to obtain signals for allowable Bragg reflections. As mentioned above, the films were on the order of 6 nm with nanocrystalline morphology. It is unlikely that such a film would possess enough ordering to give off strong enough reflections for XRD. Despite these hurdles, we decided to perform XRD measurements at the synchrotron facilities at Brookhaven national labs. Figure 43 shown below is a plot of the θ-2θ scans for b-P along with b-AsP, while Figure 44 displays our thin film θ-2θ scan conducted at the synchrotron at Brookhaven.

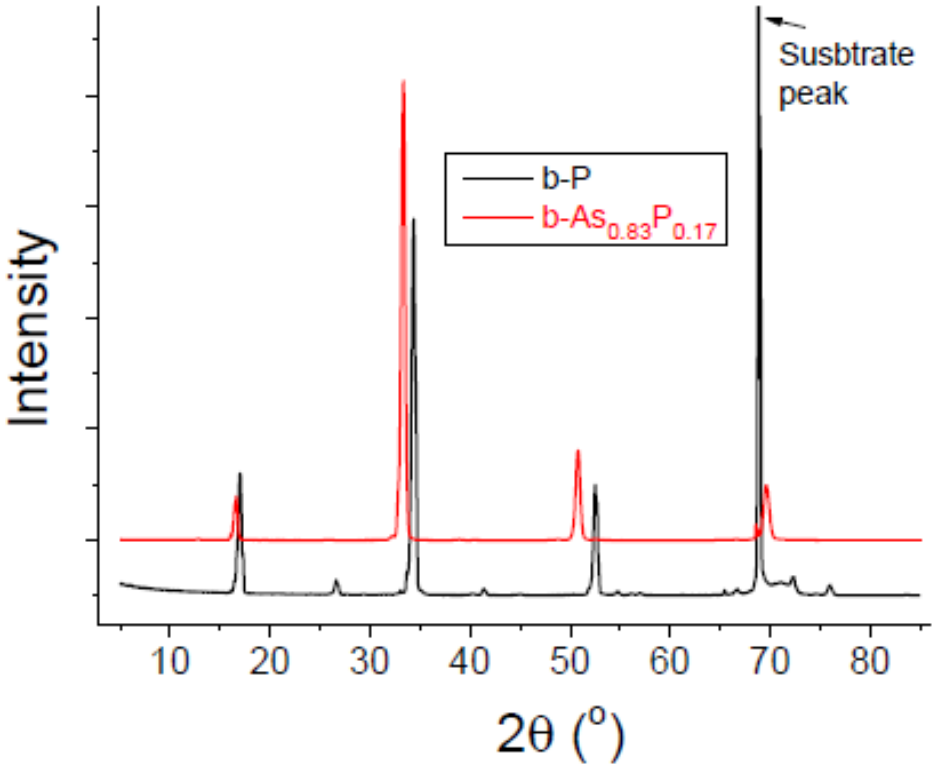

Figure 3.22: XRD θ-2θ scan for bulk b-P as well as bulk b-AsP. Several reflections are shown for b-P, though the major ones are at 17°, 34° and 52°. The reflections for b-AsP are shifted to smaller angles and are occur at 16°, 33°, and 51°

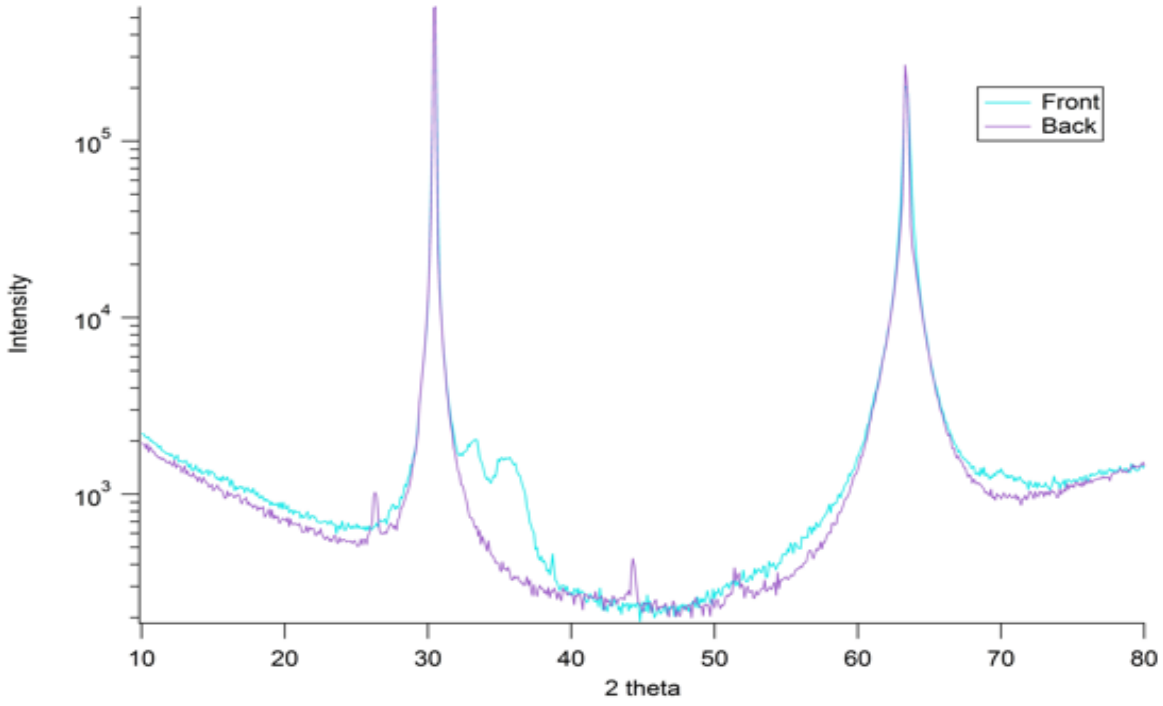

Figure 3.23: XRD θ-2θ scan for b-AsP thin films. Two broad, weak reflections are shown, one at 34° and another at 36°.

The reflections seen in Figure 43 for both b-P and b-AsP are at similar angles because both materials have an orthorhombic crystal structure. The small shifts in angles arise from the difference in lattice parameter between the two. Because b-AsP contains the larger As atom, an expected shift in lattice parameter, cell volume and subsequent d-spacing is expected. Since the d-spacing is directly related to the angle of reflection given by Bragg's law, an angle shift is expected. From the data obtained for our thin films, two broad week reflections are shown at 34° and another at 36°. While this may indeed be a real reflection, the data we obtained is

inconclusive. Similar experiments were repeated at UCLA without using synchrotron radiation. Again, conclusive XRD evidence was not obtained, most likely due to the fact that the film simply is not crystalline enough to give off strong Bragg reflections. As a result, the synthetic process of our films needs to first be optimized before further XRD measurements can be performed.

3.8 High Temperature Annealing

Although low-temperature annealing results demonstrated the most success as evidenced by Raman as well as TEM, high temperature conditions were also attempted. The rationale behind these experiments was to investigate the effect of having a higher driving force on crystallization. Although nanocrystalline grains were visualized for annealing conditions between 250-350 °C, grain sizes were only on the order of 5 nm. Figure 45 is another depiction of the phase diagram of b-P. Theoretically, going to higher temperatures should provide a higher driving force for nucleation. For diffusional transformations, a two-step nucleation followed by growth occurs. Several texts provide more in-depth detail on the topic which can be found in the references. In solidification, there is a tradeoff between driving force and nucleation, since the final state is at a lower temperature than the initial melt. However, in our system, the black phase is in the higher temperature, thus both the diffusion rate and the driving force are increased at higher temperature.

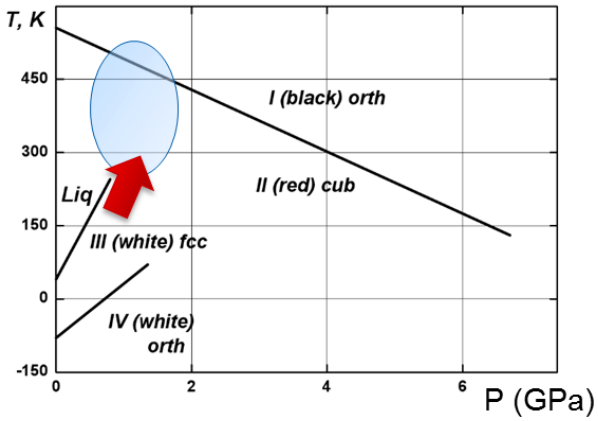

Figure 3.24: Black phosphorus phase diagram, including temperature dependent r-P to b-P empirical phase equilibria boundary.

In order to successfully anneal AsP, different materials needed to be chosen both for substrate as well as for passivation. This is because the original InP/AsP/Al_2O_3 stack did not survive under high annealing temperatures. It is well known that many of the III-V materials breakdown at temperatures above 350° C. As a result, a more robust substrate needed to be chosen. Additionally, cracking of the passivation layer due to pressure buildup also caused the Al_2O_3 to fracture at higher temperatures. To eliminate these material failures, we chose 300 nm SiO_2 on Si for our substrate and a Si_4N_3 passivation layer. The temperatures attempted were in the range between 500 and 700°C. The Si_4N_3 was deposited via a low temperature PECVD process; and a schematic of the entire film stack can be seen below.

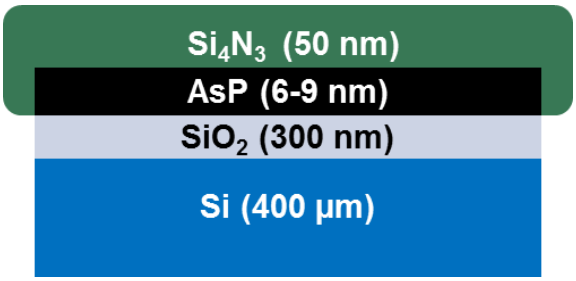

Figure 3.25: Schematic of film stack used for high temperature annealing process. The substrate is SiO_2 on Si and the passivation layer is Si_4N_3.

High-temperature annealing led to destruction of the films as evidenced by a variety of different metrology techniques. Figure 47 shows the Raman spectra for the post-annealed films. While the As-As and P-P vibrational modes located at 240 cm^{-1} and 435 cm^{-1} appear unaltered, the mixed mode is significantly shifted and a new signal is seen. The mixed As-P mode at 300 cm^{-1} is shifted nearly 50 cm^{-1}; which is probably a consequence of substrate and passivation layer interactions. Additionally, a previously undetected peak at 475 cm^{-1} is seen. The inconsistencies in Raman data most likely indicate that a new compound is formed. The high temperature annealing caused significant interdiffusion at the film interfaces, thus resulting in a compromised film.

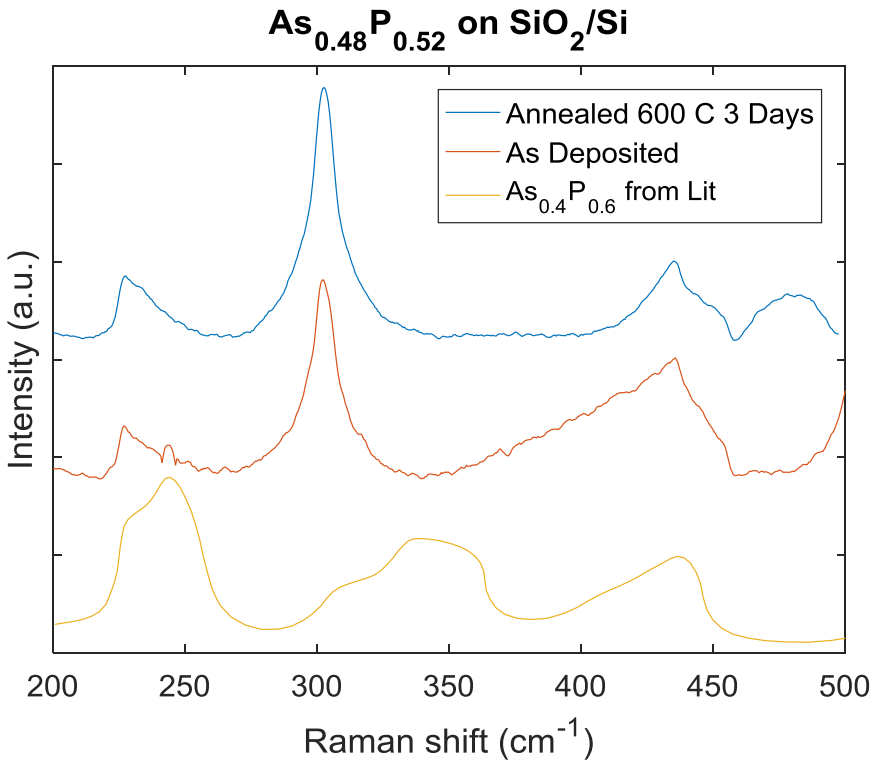

Figure 3.26: Raman spectra of film stacks annealed at high temperatures. For this sample, the temperature chosen was 600 C. The annealed film showed the evolution of a new peak at 475 cm^{-1}.

In order to visualize our film stacks and further troubleshoot the Raman catastrophe, we cross-sectioned our films and visualized them using TEM. Additionally in STEM mode, we obtained compositional information by conducting a line scan and analyzing via EDX. Under HRTEM, we see a totally interdiffused Si_4N_3 and AsP film. Selected area diffraction also showed no signal, a consequence of there being no crystallinity within the film. The EDX showed no detectible As or P peaks. The metrology results clearly indicate that the film was totally destroyed. Figure 48 depicts the HRTEM results from high temperature annealing, while Figure 49 shows the EDX results from STEM mode.

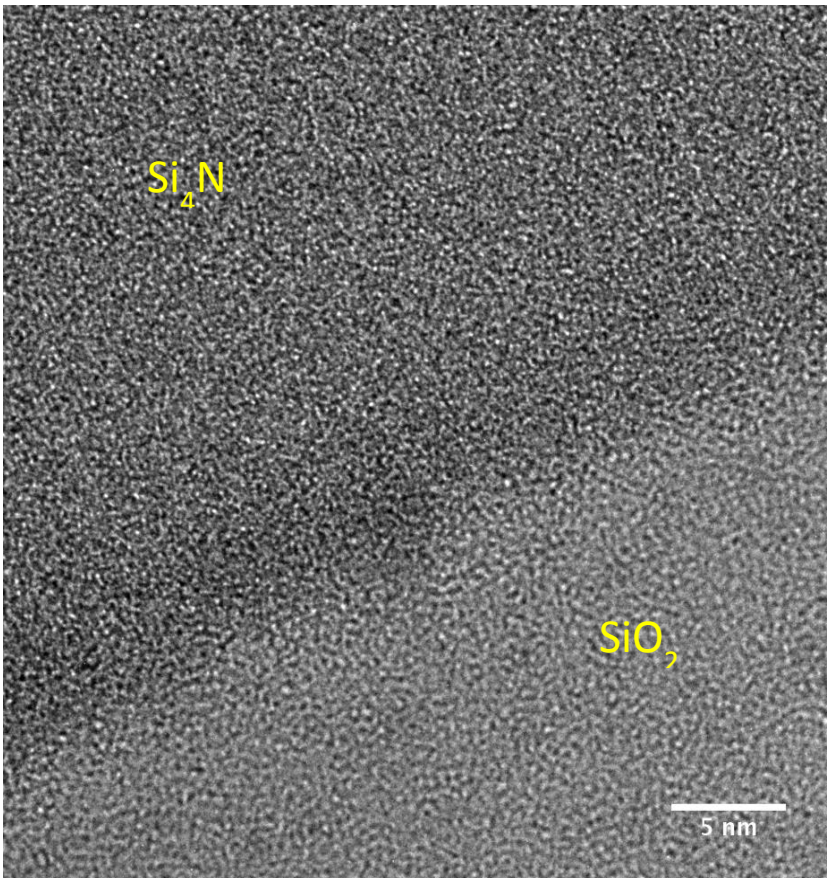

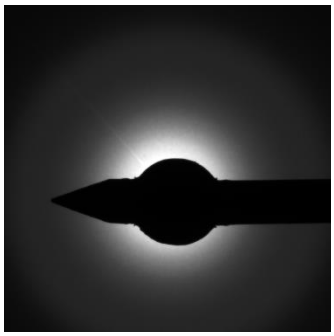

Figure 3.27: HRTEM image for samples annealed at high temperatures. Right image shows SAD image. No crystallinity is seen in the Si_4N_3 region, which is indistinguishable from the AsP. However, the SiO_2 substrate is visible.

Alarmingly, no As or P signals were detected form the EDX plots. In addition to a line scan, a selected area was also probed and analyzed. It is possible that because of the interdiffusion, the As and P atoms were so mixed and sparse that no signal whatsoever was detected. In any case, EDX validates the assumption that the films were totally destroyed from annealing above 500 °C.

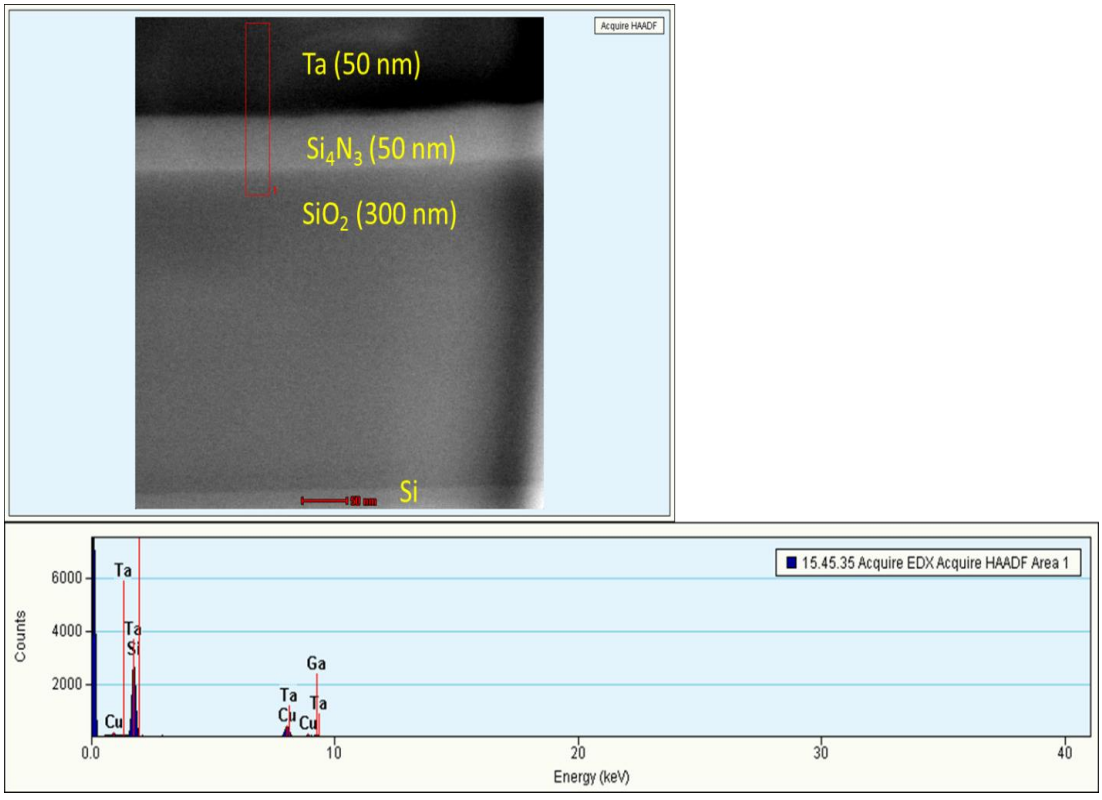

Figure 3.28: STEM mode EDX data for the highlighted red box seen above. EDX shows no As or P peaks, evidencing a destroyed film.

3.9 References

(1) George, Steven M. "Atomic layer deposition: an overview." *Chemical Reviews* 110.1 (2009): 111-131.

(2) Puurunen, Riikka L. "Surface chemistry of atomic layer deposition: A case study for the trimethylaluminum/water process." *Journal of applied physics* 97.12 (2005): 121301.

(3) Denn, Morton. *Process FLuid Mechanics*. 1. Prentice Hall, 1998. Print.

(4) Bergman, Theodore, Adrienne Lavine, Frank Incropera, and David DeWitt. *Fundamentals of Mass and Heat Transfer*. 1. Wiley, 2011. Print.

(5) Panish, M.B. Molecular Beam Epitaxy. Science. 1980, 208, 916-922.

(6) Ramanarayanan, T.A.; Rapp, R.A. The diffusivity and solubility of oxygen in liquid tin and solid silver and the diffusivity. Metallurgical Transactions. 1972, 3, 3239-3246.

(7) (Xia F, Wang H, Jia Y., Rediscovering black phosphorus as an anisotropic layered material for optoelectronics and electronics. Nat. Commun. 2014, 5:4458.

(8) Jakschik, S.; Schroeder, U.; Hect, T.; Gutsche, M.; Seidl, H.; Bartha, J. W. Crystal- lization behavior of thin ALD-Al_2O_3 films. Thin Solid Films. 2003, 425, 216–220.

(9) Dong, H.; Cabrera, W.; Galatage, R. V.; Santosh, K. C.; Brennan, B.; Qin, X.; McDon- nell, S.; Zhernokletov, D.; Hinkle, C. L.; Cho, K.; Chabal, Y. J.; Wallace, R. M. Indium diffusion through high-k dielectrics in high-k/InP stacks. Appl. Phys. Lett. 2013, 103, 061601.

Chapter 4: Wafer-Scale Deposition and Recrystallization of Black-Arsenic-Phosphorus Thin Films

4.1 Abstract

Herein we report the wafer-scale synthesis of few-layered black arsenic phosphorus (b-AsP) alloys via two-step solid-source molecular beam deposition (MBD) and subsequent hermetic thermal annealing. We characterized our thin films with a variety of compositional and structural metrology techniques. X-ray photoelectron spectroscopy and energy dispersive spectroscopy determine compositions of $As_{0.78}P_{0.22}$ for our thin films, while x-ray reflectivity measurements indicate film thicknesses of 6-9 nm. High-resolution transmission electron spectroscopy images reveal a nanocrystalline morphology with orthorhombic b-AsP grains on the order of ~ 5 nm. Raman scattering spectroscopy is employed to characterize the vibrational spectra of our thin films; and the results obtained are in agreement with previously reported b-AsP spectra. Evidence of uniform wafer-scale growth is substantiated by Raman mapping. We simulate crystal structure, bandgaps, and Raman spectra from first-principles DFT-based computations and find excellent agreement with our experimental results. This work is the first demonstration of on-wafer synthesis of b-AsP. Our large-area growth technique enables the development of next-generation b-AsP devices for optoelectronic, digital and RF applications.

4.2 Introduction

Two-dimensional (2D) black phosphorus (b-P) has recently garnered significant interest as a unique, low-symmetry layered material due to its inherent anisotropic optical and electronic

properties, high carrier mobility, and tunable, direct bandgap [1-6]. Akin to graphene and the transition metal dichalcogenides (TMDs), b-P is a layered material which exhibits strong in-plane covalent bonding and weak interlayer van der Waals (VDW) interactions. As a result, b-P can be micromechanically exfoliated to obtain both few-layer and monolayer [6,7]. Previous studies on exfoliated b-P have revealed a thickness-dependent direct bandgap ranging from 0.3 eV in the bulk to ~1.7 eV at the monolayer limit [8-10]. Additionally, b-P has been demonstrated to possess an electrically tunable direct bandgap over a range of ~250 meV [11,12]. These unique structural and optoelectronic properties have enabled the fabrication of a wide variety of devices with remarkable performance including p-n junction diodes, infrared photodetectors, field-effect transistors (FETs), gas sensors, thermoelectrics, and battery electrode materials [13-18].

The capability of b-P to absorb mid-wavelength infrared (MWIR) distinguishes it from other layered 2D material analogues. For instance, extensively studied 2D graphene is gapless, while the more recent 2D material MoS_2 possesses a 1.8 eV bandgap in the visible range [19,20]. Devices that operate between 0.25-0.40 eV MWIR and 0.10-0.15 eV long-wavelength infrared (LWIR) regimes have utility for defense applications such as thermal imaging and night vision. Recently, synthesis of black arsenic-phosphorous alloys (b-AsP), with bandgaps smaller than that of b-P, has enabled access to the LWIR region which was previously difficult with traditional 2D materials [21,22]. Modulation of b-AsP stoichiometry allows bandgap tunability. The bandgap of b-AsP may range from 0.3 eV for b-P to 0.15 eV, making b-AsP an attractive material for LWIR optoelectronics. Structurally, b-AsP maintains the orthorhombic crystal structure and symmetry of the monoelemental b-P . Due to its puckered crystal structure, b-AsP similarly demonstrates anisotropic electronic and optical properties. Initial b-AsP back-gate FET devices have shown

hole mobility of 110 $cm^2 V^{-1} s$ which validates the feasibility of b-AsP integration into a variety of electronic and optoelectronic devices [23,24].

While both b-P and b-AsP exhibit promising properties and an array of potential applications, their large-area on-wafer synthesis has remained elusive to date [24]. Although orthorhombic b-P is the most thermally stable allotrope of phosphorus, it is also the most difficult phase to synthesize using traditional growth techniques (i.e. solidification, chemical vapor deposition, epitaxy) since it is traditionally synthesized at high-pressure. Experimental results for the conversion of amorphous red-phosphorus (r-P) to b-P have been successfully shown at 5 GPa at 25°C as well as 1.2 GPa at 200°C. Recently, a low-pressure route to free-standing, bulk single crystal b-P and b-AsP via vapor-phase reaction using metal-halide catalyst was reported [25,26]. Subsequently, the first successful on-substrate synthesis of b-P using a two-step growth and conversion process was demonstrated [27]. This approach utilized vapor-phase deposition of r-P onto a polyethylene terephthalate (PET) substrate, followed by a high pressure (10 GPa) room temperature conversion using a multi-anvil cell. Nano-crystalline morphology was observed with grain sizes on the order of 10 nm. Recently, Xia et al. further improved their process by converting r-P to highly crystalline b-P at process conditions of 700°C and 1.5 GPa [28]. Conversions were conducted on sapphire substrates with grain sizes on the order of tens of microns. While novel, the method utilizes custom, complex tooling that can be inefficient and costly for large-are production. Additionally, the high-pressure nature of the process dramatically limits the choices of viable, robust substrates due to substrate fracture. Very recently, b-P inks for inkjet printing have been developed and subsequent photonic and optoelectronic applications have been demonstrated [29]. However, shortcomings of inkjet printing for device fabrication, such as non-

uniformity and poor crystallinity, are sufficient reasons to explore alternative deposition technologies [30]. Thus, b-P and b-AsP integration into modern devices via development of a new low-cost, on-wafer, scalable synthesis approaches is highly desirable.

In this work we present a novel synthetic route to synthesizing b-AsP on-wafer. Our two-step approach involves the deposition of thin film b-AsP on 3" wafers via molecular beam sources, followed by a post-growth hermetic annealing process. We subsequently characterized both structural and optical properties of our thin films. Chemical compositions of our b-AsP alloys are determined by X-ray photoelectron spectroscopy (XPS) and energy dispersive spectroscopy (EDS). Transmission electron microscopy (TEM) reveals an amorphous film recrystallized with nanocrystalline grains sized at ~5 nm. Raman spectroscopy measurements confirm signatures consistent with bulk b-AsP, and suggest improved film crystallinity as a result of annealing. Additionally, evidence of conformal, large-area growth is substantiated by Raman mapping. To validate our experimental results, we perform first-principle density functional theory calculations and simulate the Raman spectra for varying composition and thickness b-AsP alloys. Our calculations are in good agreement with our experimental results. Using our model, we also predict theoretical bandgap values. Our results are found to match well with previous work. Our novel growth method is a low-pressure, scalable, and facile on-wafer approach which will promote the rapid integration of b-AsP into a variety of electronic and optoelectronic on-chip devices.

4.3 Results and Discussions

4.3.1 Molecular Beam Deposition Growth

Thin b-AsP films (6-9 nm) were deposited via solid-source molecular beam deposition (MBD) using a Varian Gen II on (001) 3" InP substrates. Both the absence of substrate-film intramolecular bonds and the lattice-mismatch between orthorhombic b-AsP and InP point to a non-epitaxial growth mechanism. InP substrates were subject to a pre-deposition bake at 510°C to drive off trace moisture and low vapor pressure contaminants. Due to the high vapor pressure of phosphorus, depositions were done in the absence of substrate heating to prevent re-evaporation from the substrate surface. Deposition began at substrate temperatures of -34°C, a result of the cooling from the cryogenic substrate shroud, though radiative heating from the molecular sources during the 2 hour growth heated the substrate to a final temperature of ~34°C. The As_2 source flux was measured to be 7.1×10^{-8} Torr while the P_2 flux was recorded to be 7.1×10^{-7} Torr. Despite the order of magnitude difference, the as-deposited thin-film alloys showed comparable amounts of As and P due to the discrepancy in the P_2 and As_2 sticking coefficients [31]. Depictions of our experimental setup can be found in the supplementary material. Figure S2 depicts the two stage phosphorus cracker used in our system. Previous studies have suggested that vapor-solid deposition routes to b-P require P_2 precursors as compared to gaseous P_4, which we emulate with our three stage phosphorus cracker, depicted in the supplementary materials Figure S1 [32]. Solid red phosphorus is charged at 350°C and converted to solid white phosphorus. A heater sublimes the white phosphorus into gaseous P_4 which subsequently passes through a high temperature cracking zone held at 950°C. A similar cracker was used to produce

our As_2 beam. Film thicknesses were obtained from x-ray reflectivity (XRR) measurements and were found to be 9 nm.

Because b-P is well known to oxidize in ambient conditions [33], deposited thin films were passivated with 17 nm of Al_2O_3 through a low temperature ALD process. Encapsulation also served the purpose of inducing internal stress within the thin-film during annealing, thereby increasing the thermodynamic potential for phase transformation. A matrix of annealing conditions, seen in Figure S3, was attempted ranging from temperatures 50-700°C and times 30 seconds to 10 days. A narrower range of conditions at low temperature (250-350°C) and long dwell time (3-10 days) had the most success as qualified by our Raman results. This is in agreement with previous synthetic pathways reported for both bulk and on-film growth which all seem to be kinetically limited. Short anneal times of < 1 day yielded no change in Raman signal, while higher temperatures resulted in substrate and passivation layer degradation and mechanical fracture. We are currently exploring film stacks consisting of alternative, more robust substrate and encapsulation materials in order to accommodate higher annealing temperatures. Figure 4.1a depicts our complete synthetic route, with MBD of As and P, hermetic passivation, and annealing. Figure 4.1b highlights the low-pressure region of interest on the T-P phase diagram for b-P that this work explores. Although the phase diagram for b-AsP will undoubtedly differ from that of b-P due to differences in thermodynamic mixing potentials for alloys versus monoelemental species, few accurate phase diagrams exist for the relatively unexplored b-AsP material. Figure 4.1c shows a low-resolution TEM image of our complete film stack, thus confirming successful deposition.

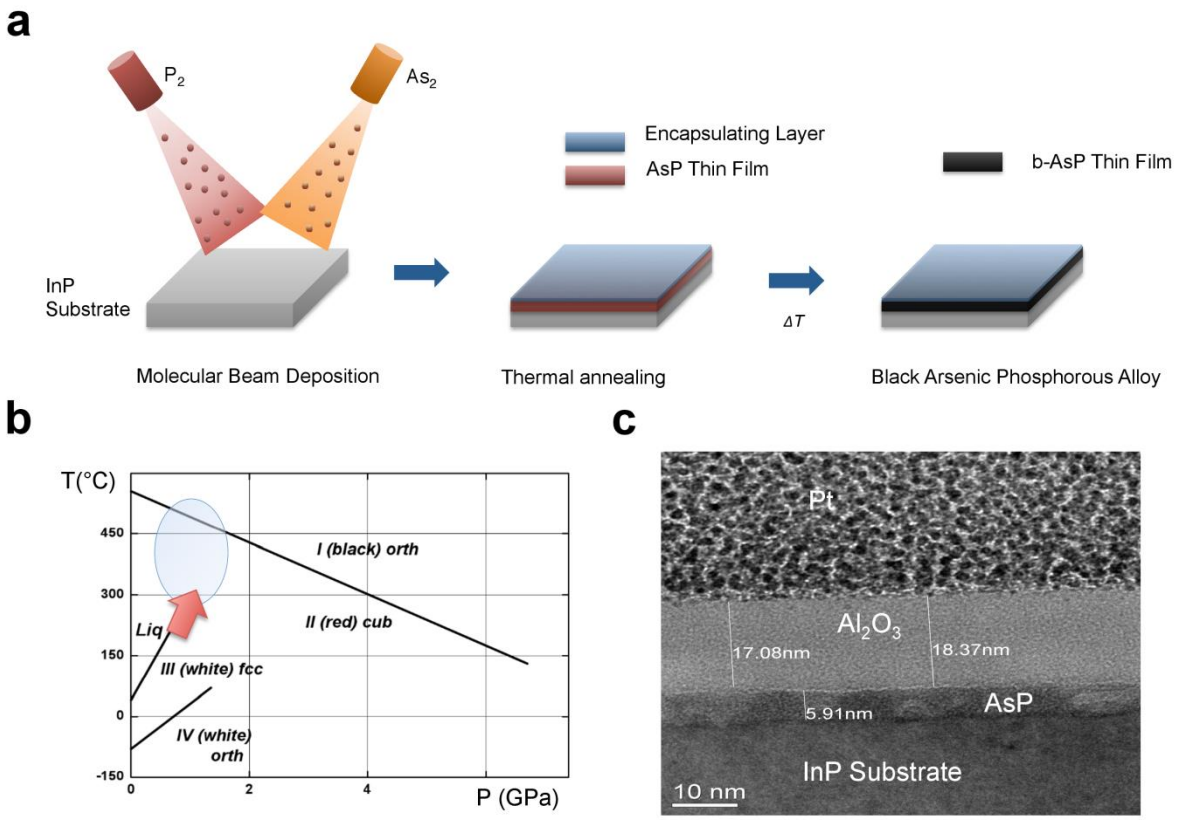

Figure 4.1: (Color online) Synthetic route and characterization of b-AsP Alloys. (a) Schematic illustration of the molecular beam deposition of AsP on-wafer. Following deposition, films are subjected to Al_2O_3 passivation and subsequently annealed. (b) Phase diagram of black phosphorus with r-P to b-P phase-change region of interest circled. (c) Low resolution TEM image of cross-section of film stack.

4.3.2 Characterization of b-AsP Thin Films

X-ray photoelectron spectroscopy (XPS) measurements were performed to characterize the composition of our b-AsP films. An inert gas Ar ion mill was used to sputter off the Al_2O_3 passivation coating and expose our growth layer. Figure 4.2 shows XPS results of core-shell

signatures of As, P, In, and O. Oxygen 1*s* scans showed negligible signal, indicating that the passivation method prevented film oxidation. Of significance, low In content was detected, validating a conformal b-P film above the InP substrate. Carbon signatures were detected and were attributed to adventitious carbon on the film surface. To obtain the stoichiometry of the AsP films, the normalized peak areas for As and P were compared. Both the As 3*d* and the 2*p* core-shell orbitals were selected for analysis and compared to the phosphorus 2*s* and 2*p* peaks. These photoelectrons were chosen because they are well known to possess the highest photoelectron intensity for elements As and P. Calculated compositions at several different points on the wafer were consistent, with alloy composition $As_{0.78}P_{0.22}$. Little compositional variation across an entire 3" wafer as validated by our XPS experiments thus confirms conformal, large-area growth.

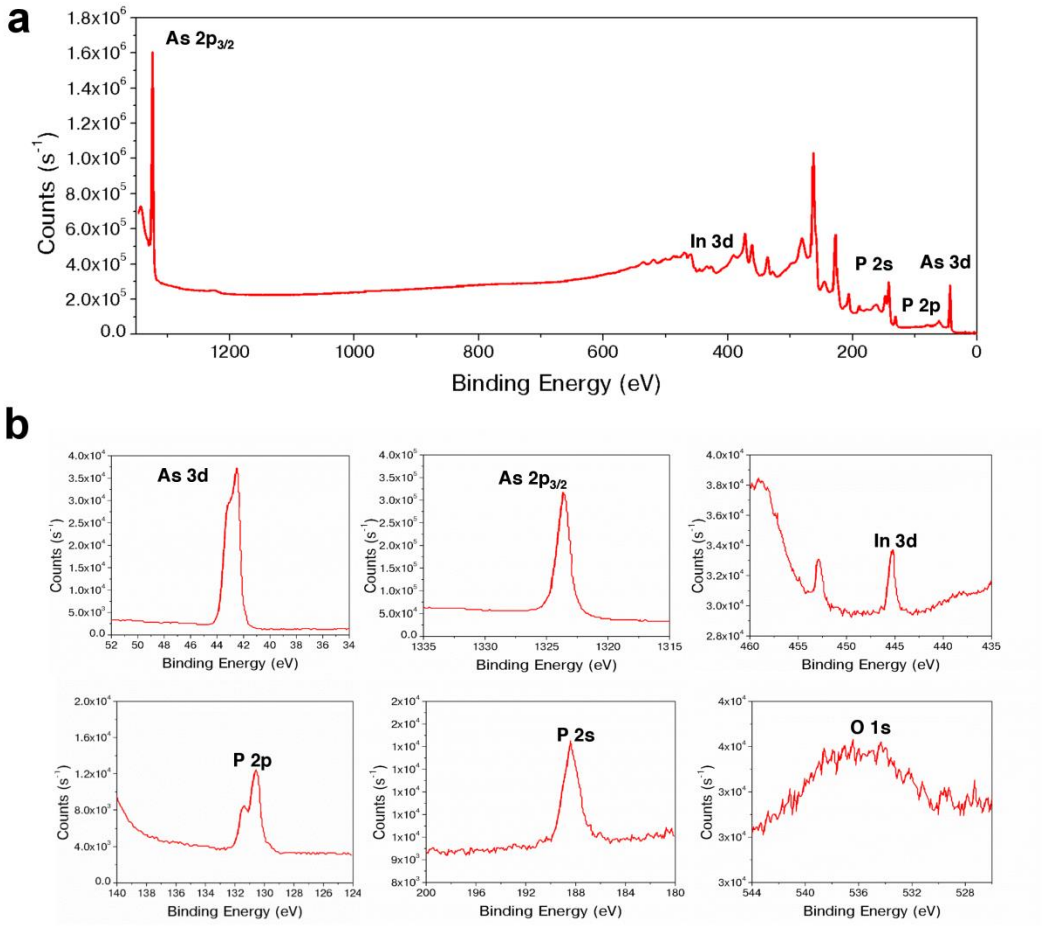

Figure 4.2: (Color online) XPS data for b-AsP thin films. Film stacks were subject to an inert gas mill to remove Al_2O_3 passivation layer. (a) Survey scan for thin films showing relevant As, P and In photoelectron peaks. (b) Individual photoelectron scans for As, In, P and O. Data was consistent across entire 3" wafer with calculated stoichiometry of $As_{0.78}P_{0.22}$. Negligible O 1*s* signal confirms low oxidation levels within the film.

To further probe the structural and chemical properties, we exposed a cross-section of the film stack using focused ion-beam (FIB) milling. Additional details of the FIB process can be found in the supplementary information (S5). The cross-section of was imaged using a JEOL 1400

TEM shown in Figure 3c. The result was consistent with x-ray reflectivity (XRR) thickness results of a ~17 nm oxide passivation layer and ~6 nm AsP film. To further validate XPS compositional data, electron dispersive spectroscopy (EDS) line scans were acquired in the transmission electron microscopy (TEM) chamber as shown in Figure 4.3a. Due to the spatial resolution limitations of the EDS, chemical signatures from the Pt scaffold, InP substrate and the Al_2O_3 passivation layer were all detected. Significantly, interfaces within the stack can be seen to be rough, which is attributed to activated diffusion of various elements during the annealing process [34]. The optimization of MBD on other wafers in order to limit diffusing species will be the focus of future work.

Structural characterization of the b-AsP thin-films was performed by utilizing high resolution TEM imaging. Atomic resolution was obtained using a 300 kV accelerating voltage FEI Titan microscope. A largely amorphous network is observed for both the film and the passivation layer. However, small crystalline regimes can be visualized in the Al_2O_3 layer which is expected as Al_2O_3 thin films grown by ALD can crystallize under proper annealing conditions [35]. Notably, nanocrystalline grains on the order of 5 nm can be seen along the substrate-film interface. To identify the structure of the observed grains as those of b-AsP, we performed *d*-spacing analysis shown in Figure 3c. b-P and b-AsP both have an orthorhombic crystal structure defined by three unequal axial lengths *a*, *b*, *c* all at right angles $\alpha=\beta=\gamma=90^\circ$. A sample crystal structure of the orthorhombic b-AsP alloy is illustrated in S6. Orthorhombic planar *d*-spacing for planes (*hkl*) are calculated by the equation below:

$$\frac{1}{d^2}=\frac{h^2}{a^2}+\frac{k^2}{b^2}+\frac{l^2}{c^2} \qquad (1)$$

Two planar *d*-spacings were measured using Image J software from the TEM images obtained of the nano-crystalline grains and compared to data available from the International Center for Diffraction Data (ICDD) database. Because there is limited crystallinity data on the b-AsP alloys, readily available b-P data was used for comparison. The slanted neon line is orthogonal to the (131) family of planes and is parallel to the direction of the *d*-spacing vector with *d*-spacing measured to be ~1.9 Å. The nearly vertical neon line is perpendicular to the (002) family of planes and the d-spacing is measured to be ~2.16 Å. These values are close to the (131) and (002) b-P values from the ICDD database which are 2.07 Å and 2.13 Å respectively . The angle between the two neon lines is then the interplanar angle between the (131) and (002) planes for the material. For an orthorhombic crystal, the interplanar angle φ is given by:

$$cos\varphi = \frac{\frac{h_1 h_2}{a^2} + \frac{k_1 k_2}{b^2} + \frac{l_1 l_2}{c^2}}{\sqrt{\left(\frac{h_1^2}{a^2} + \frac{k_1^2}{b^2} + \frac{l_1^2}{c^2}\right) + \left(\frac{h_2^2}{a^2} + \frac{k_2^2}{b^2} + \frac{l_2^2}{c^2}\right)}} \qquad (2)$$

The calculated angle from the TEM image analysis is 60.8° while the (002) and (131) interplanar angle calculated from ICDD data is 65°. This discrepancy is attributed to the small difference in lattice parameters for b-AsP alloys and pure b-P. Several small nm-sized grains are observed along the cross-section. By optimizing annealing process, larger grain domains and better crystallinity can be obtained.

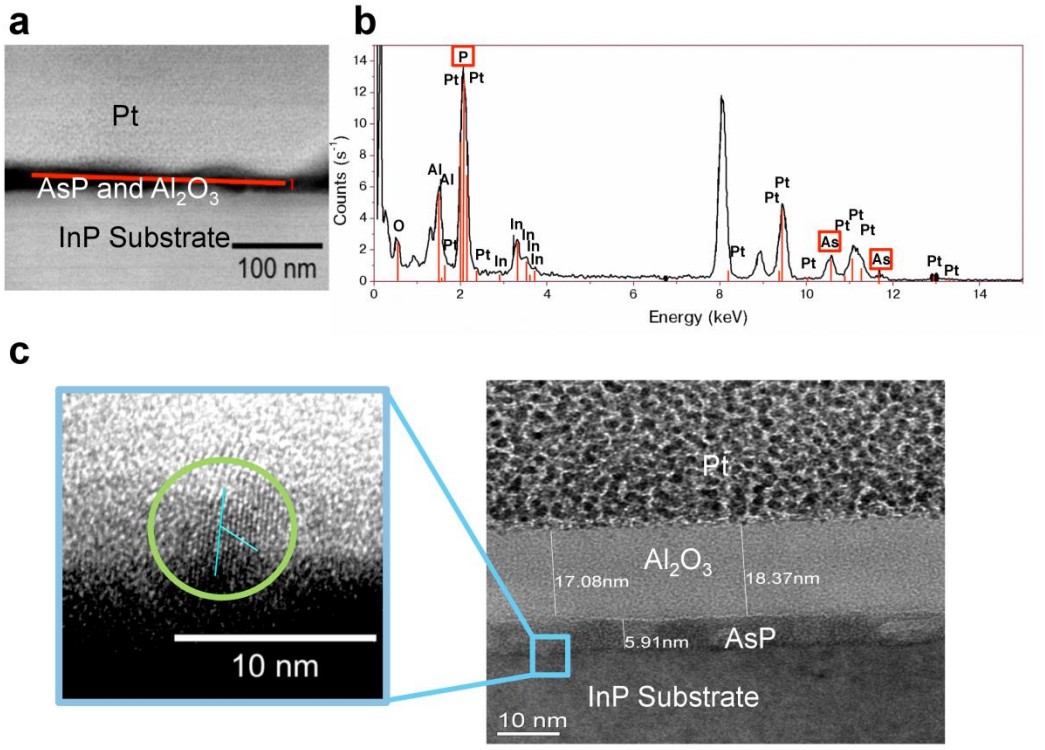

Figure 4.3: (Color online) Chemical and structural characterization of b-AsP thin films. (a) Low resolution TEM image of cross-section with EDS line-scan domain defined in red. Contrast between Al_2O_3 passivation and AsP thin film is not seen in this image. (b) EDS line-scan results showing presence of As, and P. Due to resolution limitations, substrate, passivation layer, and also Pt mold peaks are detected as well. (c) High-resolution TEM image of nanocrystalline grain observed along film-substrate interface. Neon lines represent directions normal to planes (131) and (002).

Structural properties of the b-AsP thin film alloys were further probed via Raman spectroscopy, which is a particularly powerful non-destructive technique for 2D materials that exhibit thickness-dependent Raman active phonon modes [36,37]. Additionally, for b-P and b-AsP, in-plane anisotropy results in polarization-dependent Raman modes [38,39]. As a result, Raman spectra can be used as a fingerprint to determine both the crystal orientation and the layer

thickness of b-AsP. Our thin films were subject to a 532 nm visible excitation source with laser power < 1 mW and spot size on the order of 10 μm. Figure 4.4b details the observed Raman spectra of our thin films as a function of annealing temperature compared with that of a bulk crystal synthesized through vapor transport growth of composition $As_{0.52}P_{0.48}$. These spectra exhibit excellent substantiation with both previous literature reports and data obtained from bulk crystal. Annealing has a clear effect on the evolution of the Raman spectra, as three sharp peaks are resolved from the indistinguishable 200-300 cm^{-1} broad signal seen in the as-deposited film. Peak broadening and reduced intensity are observed for amorphous materials while sharper and more intense peaks are indicative of a crystalline phase as exemplified in the well-studied Si system. We assign the heavier As-As vibrational modes to reside within the 200-300 cm^{-1} wavenumber regime. In our thin films, we identify three As-As solid modes: A_g^1 at 204 cm^{-1}, B_g^2 at 232 cm^{-1} and A_g^2 at 249 cm^{-1}. In contrast, the P-P modes are blue-shifted, and exhibit peaks within the 400-500 cm^{-1} regime and the A_g^1 mode is seen at 342 cm^{-1}. A mixed, broad As-P mode is identified at 302 cm^{-1}. Raman peaks from our thin films show excellent agreement with our bulk $As_{0.5}P_{0.5}$ sample with all peaks matching within ±10 cm^{-1}. Additionally, our data is consistent with previous reports of bulk, freestanding b-AsP Raman data. We attribute the small discrepancy in our thin-film versus bulk single crystal measurements to differences in thickness, variation in alloy stoichiometry, the on-wafer nature of our films, and presence of foreign chemicals such as the passivation layer. With varying temperature, little variation in Raman spectrum is observed, suggesting that the transformation process is kinetically controlled as compared to thermodynamically limited. We confirm conformal growth

across large areas by performing Raman mapping measurements on half of a 3” wafer seen in Figure 4b. Raman spectra are consistent across the entire wafer thus validating the success of our approach.

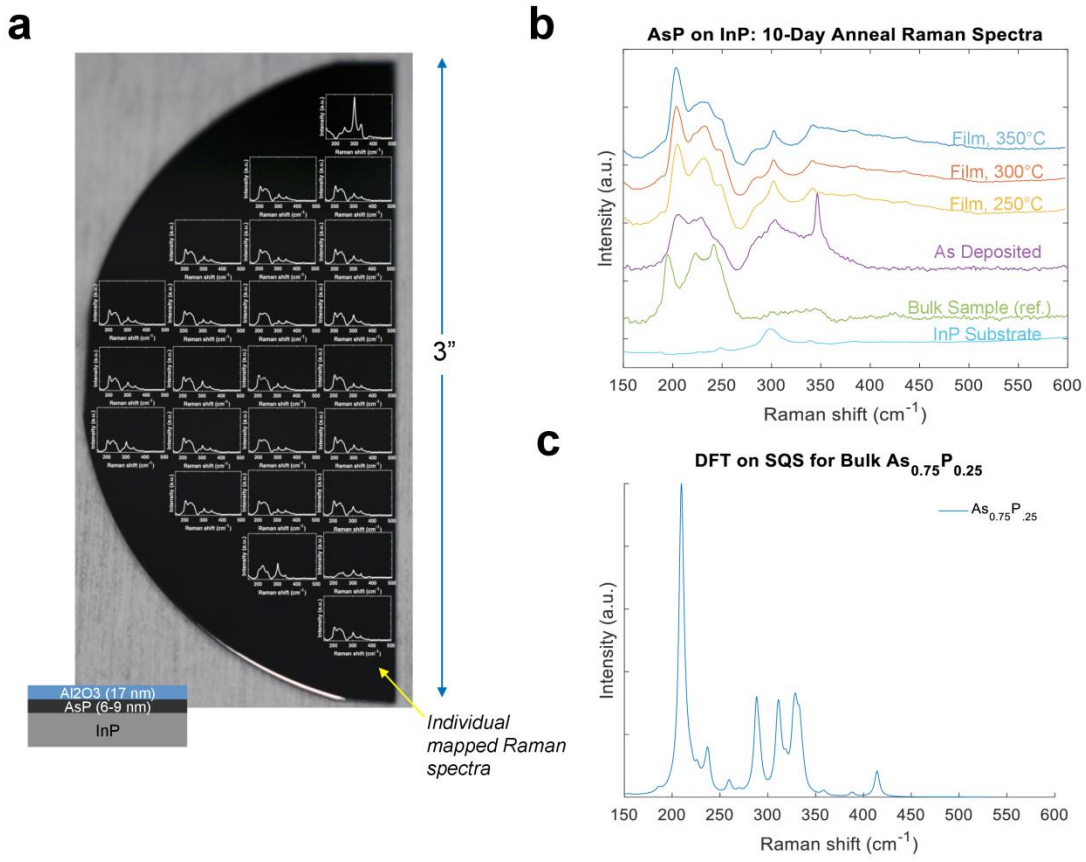

Figure 4.4: (Color online) Raman spectroscopy of on-wafer AsP. (a) Half-wafer Raman map with individualized Raman spectra. Inset is a cartoon of as-seen film stack. (b) Raman scattering spectroscopy results for thin films annealed for 10 days at different temperatures. Substrate spectra as well as bulk crystal spectra are plotted in light blue and green, respectively. (c) First principles Raman spectra for simulated bulk $As_{0.75}P_{0.25}$ crystal.

4.3.3 First-principles Raman spectra and Electronic Structure

Because of the rich structural information afforded by Raman spectroscopy, we validated our results using first-principles calculations based on density functional theory (DFT) [40]. For simulating alloys, we used special quasirandom structures (SQS) [41]. SQS has been a benchmark simulations method, and has had a successful history of characterizing a wide range of random alloys. We used density functional perturbation theory (DFPT) [42,43] to calculate phonons of these alloys en route to calculating mode Raman intensities. Intensities were adjusted to account for the laser wavelength used and were subsequently normalized. Calculations were performed for bulk crystals and vacuum-suspended monolayer, bilayer, and trilayer systems. Exemplary spectra of bulk $As_{0.75}P_{0.25}$ and suspended trilayer $As_{0.5}P_{0.5}$ SQS cells are shown in Figure 4a and 4b. Predicted locations of some of the most pronounced peaks align very well with the frequencies at which our $As_{0.78}P_{0.22}$ samples return high intensities. In addition, our prediction matches excellently with previous experimental and computational Raman data. These indicate quality phonon calculations and, again, successful b-AsP thin film synthesis. The most intense Raman activity overall is exhibited by the A_g^1 peaks around 210 cm^{-1} for bulk and trilayer alike. Direction-decomposed intensities reveal that these activities arise largely from out-of-plane vibrations of As-As bonds. Figure 5c depicts one such vibrational mode, whose out-of-plane component clearly dominates whose in-plane components.

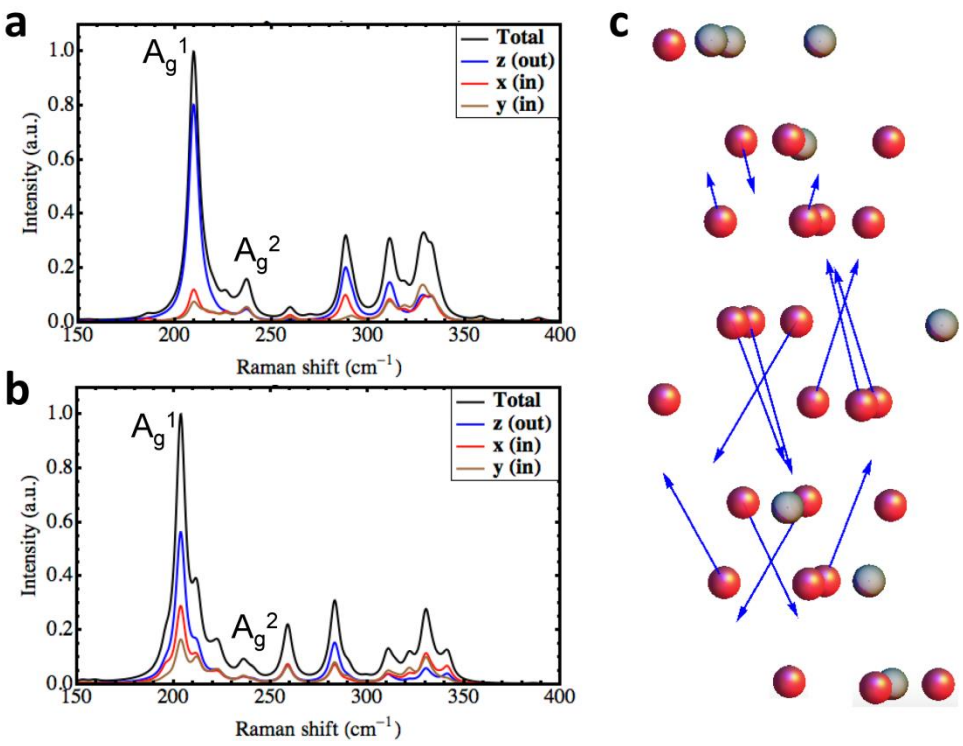

Figure 4.5: (Color online) Raman spectra calculated from first-principles. (a) Total and direction-decomposed Raman spectra of bulk $As_{0.75}P_{0.25}$. (b) Total and direction-decomposed Raman spectra of trilayer $As_{0.5}P_{0.5}$. (c) Schematic of an As-As A_g^1 vibrational mode at 208 cm^{-1} of bulk $As_{0.75}P_{0.25}$. As atoms are in red and P atoms are in gray.

Unlike peak locations, overall distribution of peak intensities somewhat differ from experiment to calculation. Intensities of our experimental peaks systematically appear much less prominent than those of the predicted peaks, as expected for a number of reasons. Experimental intensities are sensitive to exact beam polarizations and sample processing. Encapsulation of thin alloy samples from top and their fixation by the substrate on the bottom suppresses Raman signals. Moreover, our sample is partially amorphous and polycrystalline, which introduces a lot of background noise. On the computational side, perfectly parallel beam polarization is assumed.

Also, limited number of atoms in an SQS allows only so many Raman-active modes. An SQS of 32 atoms accommodates 96 vibrational modes, which may not capture all types of vibrations that would exist in real alloys. An average of Raman spectra from more SQS's of larger cell sizes may better reflect Raman activities of real alloys, though at the expense of computational load. Finally, computed values of Raman tensors partially depend on the magnitude of finite phonon displacements used to approximate the change in the dielectric tensor due to phonons.

Calculation and analyses of the behavior of the electronic structures and band gaps were also performed. We employed the HSE06 hybrid functional [44,45] to make reasonable estimations of the band gaps. Plain Perdew-Becke-Ernzerhof (PBE) exchange-correlation potential [46] coupled with the Grimme VDW correction [47] incorrectly predicts bulk black P to be semi-metallic. With HSE06 and the VDW correction, the direct gap at the Y-point is correctly reproduced as Figure 6a shows. For monolayer pure black P, the direct band gap forms at the Γ-point. As N_{layer} increases, the valence band maximum shifts away from the Γ-point towards the Y-point at the bulk-limit. For N_{layer}=1,2,3 structures, the valence bands are flat along Γ-Z, or perpendicular to layer-planes, reflecting the 2D nature.

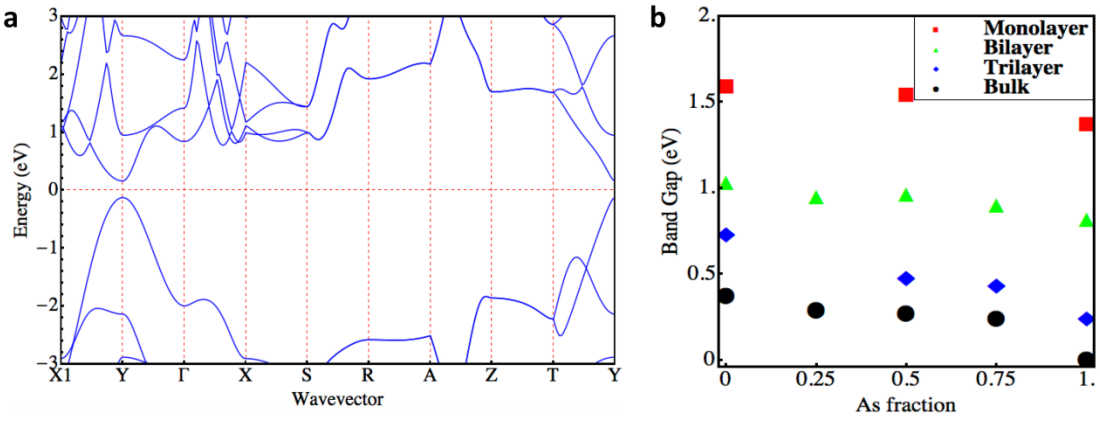

Figure 4.6: (Color online) (a) HSE06 band structure of bulk pure black P. (b) HSE06 band gaps of black As_xP_{1-x} alloys by As content and number of layers.

The trends of HSE06 band gaps are summarized in Figure 6b. Our values for pure black P are are 1.59 eV, 1.03 eV, 0.72 eV and 0.28 eV for monolayer, bilayer, trilayer and bulk. These agree well with previous results obtained from HSE06 with Grimme's correction: 1.53 eV, 1.01 eV, 0.73 eV and 0.27 eV. The gap decreases with N_{layer}, quickly approaching that of the bulk with more than three layers. It also decreases with As content *x*, as expected, though the rate of change is not necessarily linear with respect to *x*. Though the overall trends are reasonably predicted, the exact alloy gap values must be taken with caution since they are sensitive to the precise atomic configuration of SQS.

4.3.4 Conclusion

We developed a novel two-step route to synthesizing nanocrystalline b-AsP on wafer via molecular beam deposition and subsequent post-growth hermetic annealing. Chemical compositional characterization via XPS and in-situ TEM EDS confirms successful deposition of b-AsP with composition $As_{0.78}P_{0.22}$. Cross-section TEM images reveals a nanocrystalline film morphology with orthorhombic b-AsP grains on the order of ~5 nm. Raman scattering results demonstrate improved film quality as a result of thermal annealing, and acquired spectra are in good agreement with spectra acquired from bulk single crystal b-AsP. Raman mapping across half of a 3" wafer validates uniform, wafer-scale growth. Using first principle methods, we simulated the expected Raman spectra for our alloy in varying composition and layer thickness modalities. Good agreement between experimental and theoretical data is seen. To the best of our

knowledge, our results are the first successful demonstration of b-AsP on-wafer. With further optimization, our controllable and highly scalable growth technique enables the development of next-generation black AsP devices for optoelectronic, digital and RF applications.

4.3.5 Methods

We performed DFT calculations using the Vienna *Ab initio* Simulations Package (VASP) [48-51]. We used the projector-augmented wave pseudopotentials [52] with the PBE exchange-correlation functional. The plane-wave cutoff was consistently 600 eV. For all structures other than monolayers, the Grimme VDW correction was applied. In order to correctly predict the band gap and the semiconducting nature of black P, we used the HSE06 hybrid exchange correction. For simulating alloys, we used special quasirandom structures (SQS) consisting of up to 32 atoms.

Density functional perturbation theory provides static dielectric tensors (ε), harmonic phonon frequencies (ω_λ), and eigenvectors ($\mathbf{u}_{\lambda,a}$), for mode λ and atom *a*. With the phonon information, we created 2×3*N* configurations in each of which atoms were displaced in either the plus or the minus direction of Γ-point eigenvectors of 3*N* phonon modes, setting up for a 1st order finite-displacement approximation of the dielectric tensor. By performing a DFPT calculation on each frozen-phonon configuration for the dielectric tensors, we may write

$$\frac{\partial \varepsilon}{\partial \mathbf{u}_{\lambda,a}(\Gamma)} \sim \frac{\varepsilon_+ - \varepsilon_-}{\mathbf{u}_{\lambda,a}(\Gamma)}. \qquad (3)$$

The corresponding 3×3 Raman tensor elements are

$$\alpha_{\lambda,ij} = \frac{\sqrt{\Omega}}{4\pi} \sum_{\lambda,a} \frac{1}{\sqrt{M_a}} \frac{\partial \varepsilon_{ij}}{\partial \mathbf{u}_{\lambda,a}(\Gamma)} \mathbf{u}_{\lambda,a}(\Gamma) \qquad (4)$$

where Ω is the primitive cell volume and M_a is the mass of atom a. For the final calculation of Raman scattering intensity, we took into consideration that the As_xP_{1-x} films deposited in this work are amorphous-polycrystalline. The crystalline directions relative to the polarization direction of incident laser beam is for all intents and purposes random, and warrants space averaging. Thus, we calculated Raman scattering intensity according to the formulation by Porezag and Pederson [53] then applied appropriate Lorentzian broadening.

4.4 References

(1) Li, L.; Yu, Y.; Ye, G. J.; Ge, Q.; Ou, X.; Wu, H.; Feng, D.; Chen, X. H.; Zhang, Y. Black phosphorus field-effect transistors. Nat. Nanotechnol. 2014, 9, 372–377.

(2) Xia, F.; Wang, H.; Jia, Y. Rediscovering black phosphorus as an anisotropic layered material for optoelectronics and electronics. Nat. Commun. 2014, 9, 372–377.

(3) Liu, H.; Neal, A. T.; Zhu, Z.; Luo, Z.; Xu, X.; Tomànek, D.; Ye., P. D. Rediscovering black phosphorus as an anisotropic layered material for optoelectronics and electronics. ACS Nano. 2014, 8, 4033–4041.

(4) Ling, X.; Huang, H. W. S.; Xia, F.; Dresselhaus, M. S. The renaissance of black phosphorus. Proceedings of the National Academy of Sciences 2015, 112, 4523–4530.

(5) Churchill, H. O. H.; Jarillo-Herrero, P. Two-dimensional crystals: Phosphorus joins the family. Nat. Nanotechnol. 2014, 9, 330–331.

(6) Smith, B.; Vermeersch, B.; Carrete, J.; Ou, E.; Kim, J.; Mingo, N.; Akinwande, D.; Shi, L. Temperature and Thickness Dependences of the Anisotropic In-Plane Thermal Conductivity of Black Phosphorus. Adv. Mater. 2017, 29.

(7) Koenig, S. P.; Doganov, R. A.; Schmidt, H.; Neto, A. H. C.; Özyilmaz, B. Two- dimensional crystals: Phosphorus joins the family. App. Phys. Lett. 2014, 104, 330–331.

(8) Liu, H.; Du, Y.; Deng, Y.; Ye, P. D. Semiconducting black phosphorus: Synthesis, transport properties and electronic applications. Chem. Soc. Rev. 2015, 44, 2732–2743.

(9) Kim, J.; Baik, S.; Ryu, S.; Sohn, Y.; Park, S.; Park, B. G.; Delinger, J.; Yi, Y.; Choi, H.; Kim, K. S. Observation of tunable bandgap and anisotropic Dirac semimetal state in black phosphorus. Science. 2015, 349, 723–726.

(10) Das, S.; Zhang, W.; Demarteau, M.; Hoffmann, A.; Dubey, M.; Roelofs, A. Tunable Transport Gap in Phosphorene. Nano Lett. 2014, 14, 5733–5739.

(11) Rodin, A. S.; Carvalho, A.; Neto, A. H. C. Strain-induced gap modification in black phosphorus. Phys. Rev. Lett. 2014, 112, 176801.

(12) Deng, B.; Tran, V.; Xie, Y.; Jiang, H.; Li, C.; Guo, Q.; Wang, X.; Tian, H.; Koester, S. J.; Wang, H.; Cha, J. J.; Xia, Q.; Yang, L.; Xia, F. Efficient electrical control of thin-film black phosphorus bandgap. Nat. Commun. 2017, 8.

(13) Yang, Z.; Hao, J.; Yuan, S.; Lin, S.; Yau, H. M.; Dai, J.; Lau, S. P. Field-Effect Transistors Based on Amorphous Black Phosphorous Ultrathin Films by Pulsed Laser Deposition. Adv. Mater. 2015, 27, 3748–3754.

(14) Qiao, J.; Kong, X.; Hu, Z. X.; Yang, F.; Ji, W. High-mobility transport anisotropy and linear dichroism in few-layer black phosphorus. Nat. Commun. 2014, 5.

(15) Abbas, A. N.; Liu, B.; Chen, L.; Ma, Y.; Cong, S.; Aroonyadet, N.; Ko, M. Black phosphorus gas sensors. ACS Nano 2015, 9.

(16) Guo, Q.; Pospischil, A.; Bhuiyan, M.; Jiang, H.; Tian, H.; Farmer, D.; Deng, B.; Li, C.; Han, S. J.; Wang, H.; Xia, Q.; Ma, T. P.; Mueller, T.; Xia, F. Black Phosphorus Mid-Infrared Photodetectors with High Gain. Nano Lett. 2016, 16, 4648–4655.

(17) Wang, H.; Wang, X.; Xia, F.; Wang, L.; Jiang, H.; Xia, Q.; Chin, M. L.; Dubey, M.; Han, S. J. Black Phosphorus Radio-Frequency Transistors. Nano Lett. 2014, 14, 6424– 6429.

(18) Buscema, M.; Groenendijk, D. J.; Steele, G. A.; van der Zant, H. S.; Castellanos- Gomez, A. Photovoltaic effect in few-layer black phosphorus PN junctions defined by local electrostatic gating. Nat. Commun. 2014, 5.

(19) Mak, K. F.; Lee, C.; Hone, J.; Shan, J.; Heinz, T. F. Atomically thin MoS_2: a new direct-gap semiconductor. Phys. Rev. Lett. 2010, 105, 136805.

(20) Eda, G.; Yamaguchi, H.; Voiry, D.; Fujita, T.; Chen, M.; Chhowalla, M. Photoluminescence from Chemically Exfoliated MoS_2. Nano. Lett. 2011, 14, 5111–5116.

(21) Osters, O.; Nilges, T.; Bachhuber, F.; Pielnhofer, F.; Weihrich, R.; Schöneich, M.; Schmidt, P. Synthesis and Identification of Metastable Compounds: Black Arsenic - Science or Fiction? Angew. Chem. Int. Ed. 2012, 51, 2994–2997.

(22) Liu, B. et al. Black ArsenicÐPhosphorus: Layered Anisotropic Infrared Semiconductors

with Highly Tunable Compositions and Properties. Adv. Mater. 2015, 27, 4423–4429.

(23) Long, M.; Gao, A.; Wang, P.; Xia, H.; Ott, C.; Pan, C.; Fu, Y.; Liu, E.; Chen, X.; Lu, W.; Nilges, T.; Xu, J.; Wang, X.; Hu, W.; Miao, F. Room temperature high- detectivity mid-infrared photodetectors based on black arsenic phosphorus. Science Advances 2017, 3, 1–7.

(24) Zhang, J. L.; Zhao, S.; Han, C.; Wang, Z.; Zhong, S.; Sun, S.; Guo, R.; Zhou, X.; Gu, C. D.; Yuan, K. D.; Li, Z.; Chen, W. Epitaxial Growth of Single Layer Blue Phosphorus: A New Phase of Two-Dimensional Phosphorus. Nano Lett. 2016, 16, 4903–4908.

(25) Nilges, T.; Kersting, M.; Pfeifer, T. A fast low-pressure transport route to large black phosphorus single crystals. J. Solid State Chem. 2008, 181, 1707–1711.

(26) Lange, S.; Schmidt, P.; Nilges, T. Au_3SnP_7@black phosphorus: an easy access to black phosphorus. Inorg. Chem. 2007, 46, 4028–4035.

(27) Li, X.; Deng, B.; Wang, X.; Chen, S.; Vaisman, M.; Karato, S.; Pan, G.; Lee, M. L.; Cha, J.; Wang, H.; Xia, F. Synthesis of thin-film black phosphorus on a flexible sub- strate. 2D Materials 2015, 2, 031002.

(28) Li, C. et al. Synthesis of Crystalline Black Phosphorus Thin Film on Sapphire. Adv. Mater. 2018, 30, 1703748.

(29) Hu, G. et al. Black phosphorus ink formulation for inkjet printing of optoelectronics and photonics. Nat. Commun. 2017, 8.

(30) Minemawari, H.; Yamada, T.; Matsui, H.; Tsutsumi, J.; Haas, S.; Chiba, R.; Kumai, R.; Hasegawa, T. Inkjet printing of single-crystal films. Nature 2011, 475, 364–367.

(31) Holmes, D. M.; Belk, J. G.; Sudijono, J. L.; Neave, J. H.; Jones, T. S.; Joyce, B. A. Differences between As_2 and As_4 in the homoepitaxial growth of GaAs(110) by molecular beam epitaxy. App. Phys. Lett. 1995, 67, 2848–2850.

(32) Zhao, M.; Qian, H. L.; Niu, X. Y.; Wang, W.; Guan, L.; Sha, J.; Wang, Y. W. Growth mechanism and enhanced yield of black phosphorus microribbons. Cryst. Growth Des. 2016, 16.

(33) Wood, J. D.; Wells, S. A.; Jariwala, D.; Chen, K. S.; Cho, E.; Sangwan, V. K.; Liu, X.; Lauhon, L. J.; Marks, T. J.; Hersam, M. C. Effective Passivation of Exfoliated Black Phosphorus Transistors against Ambient Degradation. Nano Lett. 2014, 14, 6964–6970.

(34) Dong, H.; Cabrera, W.; Galatage, R. V.; Santosh, K. C.; Brennan, B.; Qin, X.; McDonnell, S.; Zhernokletov, D.; Hinkle, C. L.; Cho, K.; Chabal, Y. J.; Wallace, R. M. Indium diffusion through high-k dielectrics in high-k/InP stacks. Appl. Phys. Lett. 2013, 103, 061601.

(35) Jakschik, S.; Schroeder, U.; Hect, T.; Gutsche, M.; Seidl, H.; Bartha, J. W. Crystal- lization behavior of thin ALD-Al_2O_3 films. Thin Solid Films. 2003, 425, 216–220.

(36) Li, H.; Zhang, Q.; Yap, C. C. R.; Tay, B. K.; Edwin, T. H. T.; Oliver, A.; Baillargeat, D. From Bulk to Monolayer MoS_2: Evolution of Raman Scattering. Adv. Funct. Mater. 2012, 22, 1385–1390.

(37) Yamamoto, M.; Wang, S. T.; Ni, M.; Lin, Y. F.; Li, S. L.; Aikawa, S.; Jian, W. B.; Ueno, K.; Wakabayashi, K.; Tsukagoshi, K. Strong Enhancement of Raman Scattering from a Bulk-Inactive Vibrational Mode in Few-Layer $MoTe_2$. ACS Nano 2014, 8, 3895– 3903.

(38) Ribeiro, H. B.; Pimenta, M. A.; de Matos, C. J. S.; Moreira, R. L.; Rodin, A. S.; Zapata, J.

D.; de Souza, E. A. T.; Neto, A. H. C. Unusual Angular Dependence of the Raman Response in Black Phosphorus. ACS Nano 2015, 9, 4270–4276.

(39) Wu, J.; Mao, N.; Xie, L.; Xu, H.; Zhang, J. Identifying the Crystalline Orientation of Black Phosphorus Using Angle-Resolved Polarized Raman Spectroscopy. Angew. Chem 2015, 54, 2396–2399.

(40) Kohn, W.; Sham, L. J. Self-consistent equations including exchange and correlation effects. Phys. Rev. 1965, 140, A1133–A1138.

(41) Zunger, A.; Wei, S. H.; Ferreira, L. G.; Bernard, J. E. Special qausirandom structures. Phys. Rev. Lett. 1990, 65, 353–356.

(42) Baroni, S.; de Gironcoli, S.; Corso, A. D. Phonons and related crystal properties from density-functional perturbation theory. Rev. Mod. Phys. 2001, 73, 515–562.

(43) Gonze, X.; Lee, C. Dynamical matrices, Born effective charges, dielectric permittivity tensors, and interatomic force constants from density-functional perturbation theory. Phys. Rev. B. 1997, 55, 10355–10368.

(44) Heyd, J.; Scuseria, G. E.; Ernzerhof, M. Hybrid functionals based on a screened Coulomb potential. J. Chem. Phys. 2003, 118, 8207–8215.

(45) Heyd, J.; Scuseria, G. E.; Ernzerhof, M. Efficient hybrid density functional calcula- tions in solids: Assessment of the HeydÐScuseriaÐErnzerhof screened Coulomb hybrid functional. J. Chem. Phys. 2004, 121, 1187–1192.

(46) Perdew, J. P.; Burke, K.; Ernzerhof, M. Generalized gradient approximation made simple.

Phys. Rev. Lett. 1996, 77, 3865–3868.

(47) Grimme, S. Semiempirical GGA-type density functional constructed with a long-range dispersion correction. J. Comp. Chem. 2006, 27, 1787Ð1799.

(48) Kresse, G.; Hafner, J. Ab initio molecular dynamics for liquid metals. Phys. Rev. B. 1993, 47, 558–561.

(49) Kresse, G.; Hafner, J. Ab initio molecular-dynamics simulation of the liquid- metal–amorphous-semiconductor transition in germanium. Phys. Rev. B. 1994, 49, 14251–14269.

(50) Kresse, G.; Furthmüller, J. Efficiency of ab-initio total energy calculations for metals and semiconductors using a plane-wave basis set. Comp. Mat. Sci. 1996, 6, 15–50.

(51) Kresse, G.; Furthmüller, J. Efficient iterative schemes for ab initio total-energy calculations using a plane-wave basis set. Phys. Rev. B. 1996, 54, 11169–11186.

(52) Blöchl, P. E. Projector augmented-wave method. Phys. Rev. B. 1994, 50, 17953–17979.

(53) Porezag, D.; Pederson, M. R. Infrared intensities and Raman-scattering activities within density-functional theory. Phys. Rev. B. 1996, 54, 7830–7836.

Chapter 5: Summary

In this thesis, the wafer-scale synthesis of thin-film b-AsP is demonstrated. The method that was developed involves the molecular beam deposition of AsP followed by subsequent hermetic annealing for recrystallization. Grown thin films were characterized by a variety of structural and compositional techniques in order to validate successful growth. Additionally, we employed theoretical models and calculations to both guide our deposition rationale, as well as verify our experimental results. Some major achievements of this thesis work are listed below:

(1) We employed MBE to deposit thin films (6-9 nm) of AsP. These films were passivated with Al_2O_3 via ALD and subsequently annealed at 250-350°C for 10 days in order to promote recrystallization into the crystalline black phase.

(2) A simple, 1-D heat transfer model was developed to determine an approximate substrate temperature profile during MBE growth. The model was implemented in order to guide our experiments. Results were reasonably accurate, with a substrate heating rate of approximately 2.27°/min.

(3) MBE growth rate was optimized by implementing an iterative growth method. Growth rates were doubled from 0.75 Å/min to 1.54 Å/min. The novel method also allowed for the deposition of thicker films of 34.3 nm as compared to 6-9 nm.

(4) XPS depth-profile measurements were conducted on our films. Results indicate a stoichiometry of b-$As_{0.78}P_{0.22}$ and were consistent across the entire wafer. XPS also revealed that ALD encapsulation was successful in preventing oxidation.

(5) Raman scattering spectroscopy was performed in order to characterize our films. Results further corroborate the successful deposition of b-AsP as the spectra taken

from our films matches extremely well with previous reports in the literature. Raman mapping was also utilized to demonstrate uniform growth across the entire wafer.

(6) The composition of the films was further verified via electron microscopy techniques. We used cross-section EDS line scans to verify the presence of As and P along the film.

(7) HRTEM images were taken and depicted a nanocrystalline morphology within the film and encapsulation region. Grains were analyzed via d-spacing analysis. The presence of orthorhombic b-AsP grains were confirmed with grain sizes on the order of 5 nm.

(8) Density functional theory was employed to predict both the electronic structure and the Raman spectra for our material. Theoretical results match reasonably well with our experimental results, further confirming successful b-AsP deposition via our method.

Appendix A: MATLAB Code for MBE Heating

```
%Define Constants
rho=4.81E3; %density of InP [kg/m3]
v=pi*(0.0381).^2*(6E-4); %volume of substrate [m3]
cp=0.31*1E3; %heat capacity [J/(kg*K)]
r1=0.0254; %radius of sources [m]
r2=0.0381; %radius of substrate [m]
sigma=5 .67E-8; %Stefan-Boltzmann Constant [W*m*K-4]
T1=950+273; %Temperature of Cell [K];
T3=T1; %Temperature of Cell [K];
Tsurr = 70; %[K]

%Areas
A1=pi*(r1).^2;
A3=pi*(r1).^2;
A2=pi*(r2).^2;

%Conduction
Acond=0.00961;
ksteel=16.3; %W*m-1*K-1
L=0.0762; %[m] equivalent to 6 inches



%View Factor
%F12
F13=0.0044;
```

```
F12=F13;

F1surr=1;


%time step

dt=.1;




%Isothermal Heating

Tcondiso=-34+273;


%Polynomial Heating

n=15000;

  t=[0:dt:(n)*dt];


Tcond=0.0574.*(t./60).^2+0.6065.*(t./60)+(254.52); %Seconds


%Piecewise

add=304.*ones(1,57000);

Tcond=[Tcond,add];


%Reset time

n=15000;

t=[0:dt:(n)*dt];


%Build Temperature Array

T=[239];

Tmax =[239];
```

```
Tcool =[239];
Tiso =[239];

%Total Model Loop
for n=[1:15000]
    Th= ((A1*F12*sigma*(T1.^4-T(n).^4))+(A3*F13*sigma*(T3.^4-T(n).^4))-
(A2*F1surr*sigma*(T(n).^4-Tsurr.^4))-(((ksteel.*Acond)./L).*(T(n)-
Tcond(n))))*(dt/(rho*v*cp))+T(n);
    T=[T, Th];
end

%Max Heating

for n=[1:15000]
    Th=
(A1*F12*sigma*(T1.^4)+(A3*F13*sigma*(T3.^4)))*(dt/(rho*v*cp))+Tmax(n);
    Tmax=[Tmax, Th];
end

%Max Cooling

for n=[1:15000]
   Th= (-(A2*F1surr*sigma*(Tcool(n).^4-Tsurr.^4))-
(((ksteel.*Acond)./L).*(Tcool(n)-Tcondiso)))*(dt/(rho*v*cp))+Tcool(n);
   Tcool=[Tcool, Th];
end
```

```
%Isothermal Sink Cooling
for n=[1:15000]
    Th= (A1*F12*sigma*(T1.^4)+A3*F13*sigma*(T3.^4)-
(A2*F1surr*sigma*(Tiso(n).^4-Tsurr.^4))-(((ksteel.*Acond)./L).*(Tiso(n)-
Tcondiso)))*(dt/(rho*v*cp))+Tiso(n);
    Tiso=[Tiso, Th];
end



T;
plot(t,T,t,Tcool,t,Tmax)
%plot(t,T)
xlabel('Time (s)');
ylabel('Temperature (K)');
legend('Model','Max Cooling','Max Heating');
legend 'boxoff';
title('Temperature Profile for Model Versus Upper and Lower Bound
Conditions')
```